Design and Applications of Cold-Cathode X-ray Imaging Systems

by

Avilash Cramer

Submitted to the Harvard-MIT Program in Health Sciences and Technology
in partial fulfillment of the requirements for the degree of

Doctor of Philosophy

at the

MASSACHUSETTS INSTITUTE OF TECHNOLOGY

February 2021

Author .....
Harvard-MIT Program in Health Sciences and Technology
Oct 30, 2020

Certified by .....
Rajiv Gupta, MD/PhD
Associate Professor, Harvard Medical School
Thesis Supervisor

Accepted by .....
Emery N. Brown, MD/PhD
Director, Harvard-MIT Program in Health Sciences and Technology/Professor of Computational Neuroscience and Health Sciences and Technology

Design and Applications of Cold-Cathode X-ray Imaging Systems

by

Avilash Cramer

Submitted to the Harvard-MIT Program in Health Sciences and Technology
on Oct 30, 2020, in partial fulfillment of the
requirements for the degree of
Doctor of Philosophy

Abstract

X-ray computed tomography (CT) and planar x-ray imaging are mainstays of modern clinical care. The electron generation mechanism in standard x-ray tubes - specifically, a thermionic cathode - is reliable and capable of high current. However, thermionic cathodes are bulky, and cannot be pulsed quickly. Non-thermionic ('cold-cathode') electron generation can be exploited to make a smaller and rapidly pulsable x-ray source. Such an x-ray source could improve not just the portability of x-ray devices, but would allow for a CT system to operate by pulsing a distributed ring of x-ray sources instead of rotating a single large x-ray source.

Furthermore, cold-cathode x-ray sources could allow for new signal acquisition and processing paradigms in the x-ray domain. This includes time-based image acquisition techniques, such as elastography and photon-counting measurements.

In this dissertation, I discuss (1) the development of two novel types of cold-cathode x-ray sources: an ultraviolet photocathode-based source, and a silicon field emission chip; (2) novel methods for planar x-ray image acquisition, including a demonstration of dynamic x-ray elastography using a pulsed photocathode x-ray source; and (3) applications of modern signal processing techniques to the tomographic image reconstruction problem.

In an epilogue, I discuss our research on N95 respirator sterilization and re-use for crisis situations.

Thesis Supervisor: Rajiv Gupta, MD/PhD
Title: Associate Professor, Harvard Medical School

Funding Acknowledgements

I was supported by the National Institute of Biomedical Imaging and Bioengineering (NIBIB), of the National Institutes of Health under award number 5T32EB1680; by the US Army Medical Research Contract Acquisition Activity under award number W81XWH-15-C-0052; by the Eran Broshy Fellowship in Medical Engineering & Science; and by the Hugh Hampton Young Fellowship of MIT.

Acknowledgments

I want to give specific credit to the people below who helped me through the research process over the last five years:

- *Gupta lab members and alumni:* Wolfgang Krull, Tim Moulton, Dr. Xiaochun Lai, Tim Boers, Dr. Dufan Wu, Dr. Kai Yang, Alankar Kowtal, Jaime Caines, Gerard Snaauw, Jake Hecla

- *NASA's Goddard Space Flight Center:* Steve Kenyon, Dr. Zaven Arzoumanian, Dr. Keith Gendreau

- *Raskar lab members and alumni:* Dr. Achuta Kadambi and Tomohiro Maeda

- *MIT Nuclear Science and Engineering:* Dr. Leigh Ann Kesler, Pete Stahl, Dr. Cody Dennett, Steven Jeapal, Dr. Michael Short, Enze Tian, Dr. Ju Li

- *MIT EECS:* Dr. Winston Chern, Dr. Girish Rughoobur

- *A.A. Martinos Center for Biomedical Imaging:* Dr. Bruce Rosen, Dr. Bo Zhu, Dr. Neha Koonjoo, Dr. Abbas Yasseen, and Dr. Ken Chang.

- *PanFab:* Deb Plana, Helen Yang, Dr. Nicole LeBeouf, Akshay Kothakonda, Dr. Michael Sinha, Dr. Sherry Yu, Dr. Peter Sorger.

I owe also a great deal to my thesis supervisors,

- *Dr. Rajiv Gupta*, at Harvard Medical School, for his guidance and leadership in the last few years, and his encyclopedic knowledge of the history, systems, and practice of radiology.

- my committee, *Drs. Mathew Rosen, Richard Lanza, and Ben Vakoc*, for their support and guidance.

And finally, I would not be here without all the friends and family who kept me sane:

- *family:* My parents, Alan Cramer and Jayashree Kalpathy-Cramer; my grandparents, Ananathy and Krishna Kalpathy, and Marcia Cramer; my girlfriend, Steph; and all of the Cramer family cousins, aunts, and uncles.

- *members of the HST student community:* Rob Hinshaw, Marc-Joseph Antonini,

Manuel Morales, Dr. Jesse Kirkpatrick, John Samuelsson, Dr. Shriya Srinivasan, Aditi Gupta, Sri Gowtham Thakku, Vamsi Mangena, Aditi Gupta, Ellen DeGennaro

- *the ski buddies:* Jimmy, Magua, Nico, Lulu, Colin, Neil, Ben Eck, Laura, Parrish, Dylan, Colie; and in memory of Ben Kessel.

- *the climbing buddies:* Hannah Varner, Liane, Asha, Chris, Nathaniel, Danielle, Max, Hannah Lippe, Evan, Alex, Eric Kirchner, Kesley Wittels, Erik Knall, David Chang, David Cain, David Migl, Mason, Cole, and many, many more.

Dedicated to my parents

Avilash Cramer

October 20, 2020

Contents

List of Figures

List of Tables

Chapter 1

Introduction

Imaging modalities such as radiography, computed tomography (CT), ultrasound, positron emission tomography (PET) and magnetic resonance imaging (MRI) are an essential component of medical practice. Planar X-ray radiography is required for diagnosing many diseases such as tuberculosis, pneumonia, pneumothorax, and fractures. As a rapid and volumetric imaging technique, CT is an invaluable part of emergency medicine and inpatient care. CT is also essential in planning radiation therapy treatments. MRI, another volumetric imaging technique has better soft tissue contrast than CT. However, it can take substantially more time for acquisition, is even more expensive and harder to maintain.

The performance of these medical image acquisition devices has steadily improved in recent decades in nearly all measurable parameters such as resolution, scan time, number of clinical applications, ease of use, and patient safety. Unfortunately, a majority of world's population still has no access to radiology systems of any kind, let alone advanced imaging such as MRI or CT. While the reasons for these disparities are multifaceted, one factor that cannot be dismissed, is the cost and complexity of radiology tools. While cell phones, internet, computers, audio and video devices, and many other sophisticated consumer electronics have seen constant decrease in the price/performance ratio, no such trend is perceptible in medical imaging.

Even though X-ray technology is over 120 years old, planar radiography is only available to roughly 1/3 of the world's population. Many underserved areas - urban

and rural - lack this basic diagnostic tool because of its cost, maintenance, power, and personnel requirements. Furthermore, plain film radiography has largely been replaced by digital radiography in high-income nations where it has become the de facto standard for X-ray imaging. Digital radiography offers a number of advantages compared to film-based X-ray imaging, which include lower lifetime costs, ease of image processing and archiving, and the potential for teleradiology. Despite these advantaged, the adoption of digital X-ray imaging has been much slower because of the high initial cost of digital x-ray detectors, which is typically on the order of USD $10,000.

CT is used to diagnose many emergent medical conditions, including stroke and traumatic brain injuries [43, 100]. Recently, CT system provided an essential method of diagnosing COVID-19, especially in the early stages of the pandemic when PCR based test kits were not widely available.[CITE AJR], and are still used extensively for this purpose in China and Europe.

Unfortunately, the size, weight, and expense of CT systems – which involve a roughly 2 ton spinning gantry [62, 132] - make them largely inaccessible for patients outside of major hospitals centers.

From a global perspective, there is only approximately 1 CT scanner per million people (pmp) in Colombia as compared to over 64 per million in Australia, and 44 pmp in the US. Across all OECD nations, there is an average of 15.6 pmp compared to an average of 0.29 per million in low-income nations. Common prices for CT scanners are between USD $500,000 and $2 million [95].

Similarly, the United States has 36.7 MR scanners pmp, while Colombia has 0.2 pmp. Amongst the Sub-Saharan African nations there are collectively 0.04 MR scanners pmp - roughly 1/1000th the rate of the US. MRI scanners typically cost on order of US $2 million. For many conditions such as brain tumors, acute stroke, and many other conditions that require good soft tissue contrast, an MRI scanner is indispensable. It also does not expose a patient to ionizing radiation. However, it is dependent on acheiving a 0.2 - 3 Tesla magnetic field, with many research scanners going as high as 7T (and higher for some animal magnets). In most modern high-

filed MR scanners, high strength magnetic field is achieved by a liquid helium-cooled superconducting magnet. Maintaining a superconducting magnet at 4 Kelvin is an expensive and resource-intense task requiring continuous power, frequent refilling of liquid nitrogen, and occasional refilling of liquid helium. An unexpected rise in the core temperature — whether by electrical or mechanical failure, or human error — can cause the superconducting magnet to quench. Such an event can easily destroy the MR scanner and result in harm to patients and personnel [37].

In addition to the national disparities between LMICs and HICs, these imaging resources are unevenly distributed in most countries because a host of factors such as income or population distribution, geography, government regulations. Even within the US, many communities lack access to basic healthcare facilities including the medical imaging support required by them. In addition to cost and complexity of the devices themselves, infrastructure issues such as the lack of adequate roads, inconsistent or nonexistent power grids, water supplies, and Internet access, limited numbers of trained radiologists and technicians add to the difficulties of using advanced imaging technology.

Many teams around the world are researching low-cost imaging solutions to address the access and availability issues plaguing advanced imaging modalities.

In this thesis, I present a body of research centered on improving the accessibility of CT scanners. Specifically, our approach is based on the development and use of new types of x-ray tubes: ones that use a non-thermionic "cold-cathode" electron generation mechanism. These sources are significantly smaller and lighter than conventional x-ray tubes, and can be pulsed quickly.

1.1 Volumetric Imaging Techniques

1.1.1 Conventional CT

Computed tomography (CT), also known as computed axial tomography (CAT), is a versatile 3D x-ray imaging modality. It is the diagnostic standard for the management

of stroke, traumatic brain injury, and many other emergent conditions. More broadly, multi-angle tomosynthesis - passing an x-ray beam through a sample and measuring its intensity at a multitude of angles around a common axis - is used in a variety of medical and industrial applications. Tomosynthesis produces a data set consisting of a large number of projections through the same cross-section at different angles. 'Tomography' is generally used to refer to volumetric imaging from a full ring of acquisition angles, while 'tomosynthesis' generally refers to a volumetric imaging from an arc ('limited angle') of acquisition angles. Computational algorithms such as the inverse Radon transform are then used to create an attenuation image of the cross-section from the series of projection images [62].

Conventional CT systems use a large thermionic source mounted opposite a detector on a helical gantry. Images are acquired from hundreds of angles as the gantry spins at up to 300 rpm. As such, the spinning gantry is a substantial mechanical and electrical engineering challenge.

The design and construction of clinical CT has undergone several changes over the years. First generation CT system used a pencil beam x-ray source, and a single detector that rotated opposite the source. The detector and source would move both linearly and radially to get a full image, an acquisition scheme known as 'translate-rotate'. The slice thickness (z-axis resolution) was determined by collimator settings on x-ray tube. First generation CT scanners had a 25-30 minute scan time.

Second generation CT replaced the pencil beam with a fan beam x-ray source. An asymmetrical spot size (created by angling the anode target relative to the electron beam) is used to reduce dose outside the detector field of view (FOV) for each acquisition. As in first-gen CT, second gen used a 'translate-rotate' acquisition scheme, but with multiple detectors in an array opposite the source rather than a single detector. Having a larger fan beam and multiple detectors reduced the scan time to around 90 seconds.

In third generation CT, a large fan beam x-ray source is used, with large detector array that moves opposite the source. The x-ray irradiation area is large enough that no translation required, as the fan entirely encompasses the patient. 3rd generation

CT scanners also saw the introduction of a helical slip ring, a mechanical gantry system where x-ray sources trace a single helical path around the patient, allowing for very fast scan times (on the order of 30 seconds for a whole body scan). 3rd generation CT is widely adopted as the standard in modern hospitals.

Fourth generation CT is very similar to 3rd generation CT, with the key difference that the detector array comprises a full 360 degrees, meaning that no detector motion is required [62, 132].

Recently, dual energy CT have been introduced in hospitals as well. In dual energy CT, a single area is imaged with x-rays at two different energies. The difference between the two resultant images can provide additional contrast. Dual energy CT imaging is accomplished using two sources at different voltages and angles, or else a single source that is quickly switching between two voltages [58].

While a large number of variations exist on the general principle, nearly all use a moving gantry holding a thermionic x-ray source. Some non-rotating CT concepts have been realized using electron accelerators and a magnetically steered beam aimed at a large ring anode surrounding the target object, although they have not yet been widely adopted, for technical and economic reasons.

CT can be combined with an intravenous contrast agent, such as iodine, in a technique known as CT angiography (CTA). CTA is a quick and robust method of visualizing blood vessels.

It is worth comparing and contrasting CT to three other volumetric imaging modalities: ultrasound, magnetic resonance imaging (MRI), and positron emission tomography (PET). While MRI and ultrasound deliver no ionizing radiation, the typical dose[1] delivered to the patient for a head CT is 2-4 milliSieverts (mSv), and for an abdomen CT is 10-20 mSv. For PET, the typical dose is on the order of 7 mSv. The average American receives a yearly radiation dose of 6.2 mSv, roughly half of which comes from medical procedures.

If the linear-no-threshold (LNT) model of cancer risk is to be believed, it is possible that up to 2 percent of all cancers in the US are caused from radiation delivered by

[1]Effective dose

CT alone [15]. However, that figure is debated [140, 130], and assumes a whole-body, uniform dose from computed tomography; the LNT model of cancer risk is itself widely disputed. While this debate is unlikely to be resolved as a controlled trial of human radiations would be unethical and impractical, but the minimum yearly dose clearly linked to an increase in cancer risk is 100 mSv.

In any case, CT also has many advantages over MRI. CT is a much quicker procedure than MRI. Additionally, MRI is contraindicated for patients with embedded shrapnel, cardiac pacemakers, or other ferrous metal implants, as they are a significant burn and trauma risk in the presence of powerful magnetic fields. MRI, PET, and CT are unavailable for bariatric patients who cannot fit in the bore of the respective imaging system (typically on the order of 80 cm). Many CT and MRI protocols use a contrast agent, which also presents the risk of an adverse reaction in the patient.

1.1.2 PET

Another volumetric medical imaging technique is positron emission tomography (PET). In PET imaging, a solution containing a molecule (commonly a sugar, such as raclopride) tagged with an unstable radioactive isotope is injected into the patient. As the isotope decays, it releases a positron (an electron anti-particle), which annihilates an electron and release two 511 keV gamma rays in opposite directions. A ring of of high-speed gamma ray detectors surrounds the patient. By recording simultaneous detections, it is possible to form a 3D intensity map of the tagged molecule. PET is a powerful tool in that it can provide physicians and scientists with biochemical activity information within the body. However, since images are a stochastic map of the location of tagged molecules, the poor anatomical from PET images is quite poor [96, 88].Because of that, PET is often combined with another imaging modality, such as CT.

1.1.3 Ultrasound

Ultrasound is a medical imaging modality that uses the reflection of high frequency (1-18 MHz, depending on the application) sound waves to image soft tissue. Ultrasound has essentially no medical risk (such as from ionizing radiation or contrast agents), and is highly portable- as such, it is often the preferred imaging tool in low-resource environments. However, ultrasound is limited in its ability to penetrate deep into tissue or bone [80, 79]. Ultrasound imaging is commonly used in the US in conjunction with x-ray mammography, and for obstetric imaging. Portable ultrasound has a variety of uses, including for imaging vasculature.

1.1.4 MRI

In MRI, a large magnetic field (typically 3 Tesla) is used to align a small fraction of odd-numbered nuclei within the patient. A radio frequency (RF) pulse at the Larmor frequency of the protons in the magnetic field is used to flip a fraction of the aligned nuclei to a higher-energy state. As the particles 'relax' to the lower energy state, they emit an RF pulse at the same frequency. The delay before this second pulse is emitted is known as the relaxation time, and is dependent on the interaction of individual protons with charged particles in their vicinity. Different tissue types have different proton densities and thus different relaxation times. This diversity in relaxation times provides the contrast in MRI images.

The primary advantage of MRI is its ability to provide good soft tissue contrast. MRI has been a mainstay of both neuroscience research and neurology care for decades, as well as the assessment of joints, spinal injuries, and many others.

Simultaneous PET/CT, PET/MRI and MRI/CT system have all seen use in recent years [118, 83, 94]. PET provides activity data, but poor resolution and anatomic data. CT provides anatomical information, and in conjunction with an intravenous contrast agent (CT angiography), can provide an excellent visualization of bone and blood vessels. MRI provides exceedingly high resolution anatomical data as well as soft tissue contrast.

However, the engineering challenge of having multiple modalities image the same subject without interfering with each other is non-trivial, and additional imaging procedures can have risks of their own, especially if they involve ionizing radiation. The use of PET/CT for oncological management in young people, in particular, has been critiqued [54]. Regardless, a smaller form-factor CT system could be more easily combined with other imaging systems.

1.2 Clinical Motivation

1.2.1 Disparities in Access

Worldwide, some three-quarters of the global population has no access to medical radiography of any kind, let alone computed tomography. This relative paucity of radiography equipment extends not just to advanced systems like MRI and CT, but also to simple projection x-ray imaging, leading to a widespread inability to diagnose virulent and debilitating conditions such as tuberculosis [129]. The disparities in access for volumetric imaging are even more acute. In OECD[2] countries [95], there is an average on 1 CT scanner per 65,000 people. In low-income countries[3], there is one CT scanner per 3,500,000 people.

1.2.2 Stroke Management

Even in high-income nations, CT systems are generally only available in major trauma center hospitals, and need to be supplied with continuous, 3-phase power. This lack of portability contributes the particular challenges of healthcare delivery in rural communities, but affects pre-hospital care in essentially every demographic community.

CT is used to diagnose a wide variety of illness and injuries: traumatic brain injuries, pulmonary embolisms, even appendicitis[4]. One especially common pathology

[2]Organization for Economic Co-operation and Development, a collection of 35 mostly high-income nations

[3]Defined as having a per capital Gross National Income of less than $1005 (2016 dollars)

[4]As the author can attest from a June 2017 incident

where CT helps guide critical medical decision making is stroke. Stroke - hypoperfusion of brain tissue - is the second leading cause of death worldwide and the leading cause of disability in the US. Stroke symptoms include one-side paralysis, slurring, vertigo, and many others. Even when survived, strokes often result in permanent brain damage. Timely interventions are crucial to stroke management [119].

Strokes come in two broad flavors: hemorrhagic (bleeding) and ischemic. Ischemic strokes can be further subdivided[5] into two subcategories: thrombotic (caused by a clot), and embolic (caused by a embolus, a catch-all term for a variety of blockages). In ischemic strokes, timely treatment by thrombolytic drugs (such as recombinant tissue plasminogen activators) can be critical step to saving lives and brain tissue. However, in a hemorrhagic stroke, one of the blood vessels inside the skull is bleeding, filling a portion of the cranial cavity with blood. In the case of a hemorrhagic stroke, delivering thromobolytic drugs would be a devastating and possibly fatal mistake. Distinguishing between ischemic and hemorrhagic strokes is accomplished through neuroimaging.

As per the MGH stroke management guidelines [43], patients with symptoms indicative of a stroke first receive a non-contrast CT to determine if the stroke is hemorrhagic or ischemic, and to rule out a non-stroke pathology (termed a 'mimic')[6]. In the case that the stroke is ischemic, patients receive an intravenous contrast injection, and CT angiography scan. This is done to visualize the occlusion, and the extent of the occluded area. Finally, a diffusion weighted MR image (DWI) is performed to determine the extent of tissue death, and subsequently whether a given patient is a candidate for more invasive, mechanical removal of a thrombus/embolus. Variations of this protocol are used in hospitals around the world [131, 57, 14, 121, 78].

Given the importance of CT in stroke management, and the widespread prevalence of strokes, one of the most convincing applications for a mobile CT scanner is the prompt diagnosis of stroke. A CT scanner that could fit in an ambulance could possibly allow paramedics to distinguish between hemorrhagic and ischemic strokes,

[5]Technically, systemic hypoperfusion (low-blood pressure) can also cause ischemia in brain tissue.

[6]Hypo/hyperglycemia, epilepsy, multiple sclerosis, and intracranial tumors are common stroke mimics

and in the latter case, deliver thrombolytic drugs in the field.

A few mobile head CT systems have been pioneered in recent years, but they are not without their drawbacks. Neurologica has introduced the 1592 kg BodyTom, and the 438 kg CereTom as mobile systems for body and neuroimaging, respectively; Toshiba markets a mobile CT system that requires a dedicated multi-axle trailer.

Mobile stroke units (basically, a CT scanner in a tractor-trailer) have been implemented by pre-hospital care providers, and provided positive patient outcomes in a few communities in Germany and in the US [29, 146]. The benefits of pre-hospital Computed Tomography Angiography (CTA), in particular, have been reported on in the last few months [57]. However, mobile stroke units (MSUs) have an annual operating cost of approximately 1 million USD (for 12 hours of use a day), and in some areas treat as few as 1.5 patients per week [14].

Because of their costs and marginal gains in health outcomes, the reception of mobile stroke units by the EMS community has been lukewarm. A searing 2017 review of the technology in the *Journal of Emergency Medical Services* notes that "[mobile stroke units] are expensive and financially non-sustainable. Without widespread deployment, they stand to benefit few, if any, patients. The money spent on these devices would be better spent on improving the current EMS system including paramedic education, the availability of stroke centers, and on the early recognition of ELVO [emergent large vessel occlusion] strokes" [11].

An editorial in *Emergency Physicians Monthly* was even harsher, claiming that "Mobile CT stroke programs seem pretty nutty" [16].

A computed tomography system that does not have any moving parts, could be significantly cheaper, lighter, and more portable than current mobile stroke units. This could address many critiques of the current MSU systems.

1.2.3 Traumatic Brain Injuries

Stroke is not the only pathology for which CT is a preferred imaging system. Although imaging guidelines in head injuries is still an area of active debate and research, CT currently (and for the foreseeable future) plays a large role in clinical management of

traumatic brain injury (TBI).

In the first 24 hours following a head injury - and if imaging is indicated - CT is the preferred neuroimaging technique. CT is best imaging tool for detecting skull fractures, acute subarachnoid, and parenchymal hemorrhages, the latter two of which are deadly and rapidly emergent conditions that can require immediate intervention [152, 100]. MRI is occasionally in recommended TBI management 48-72 hours after injury if there is a suspicion of certain of late-changing conditions (subtle lesions), or in the detection of subacute and chronic conditions. PET and ultrasound not likely to be useful in acute head injury management, as the former offers too poor anatomic resolution and the latter is unable to penetrate the skull [9].

In both stroke and TBI management, CT has a vital role in early stages of care. For these conditions and many others, CT is powerful and versatile tool in emergency medical care, and especially in the critical first hours of treatment. In emergency settings, CT has the addition advantage of a quick scan time, making it easier for patients who are intubated, agitated, or who have limbs in splints or traction. CT also usually has a larger bore than MRI, which can be an advantage for certain bariatric patients.

1.2.4 Tomosynthesis applications

Beyond CT, limited angle tomography has a number of clinical and proposed uses. Digital Breast Tomosynthesis (DBT) is a technique that has been pioneered in recent years in which x-ray images are acquired as the source moves in an arc across the breast [107]. A 3D image of the breast is then reconstructed. It is currently unknown whether DBT provides significantly better outcomes than conventional 2D mammography. A large, randomized trial (TMIST) began in 2017 and will conclude in 2020 to assess the efficacy of DBT as breast cancer screening technique over conventional 2D mammography [55].

It is worth noting that the false positive rate of conventional x-ray mammography is frustratingly high: within the US along, there are millions of false positives every

year, leading to unnecessary biopsies (and other procedures). Often, cancerous tissue can have similar radiolucency to healthy tissue, even if the mechanical properties are quite different. As such, a variety both static and dynamic elastography methods have been proposed for ultrasound, MRI, and x-ray imaging of the breast. Dynamic X-ray elastography has not yet been translated to clinical practice, but if possible, could be a valuable tool in the early detection of breast cancers - especially in conjunction with tomosynthentic imaging apparatus.

Another possible application for portable volumetric imaging is in the design of custom prosthetics. Modern 3D printers allow for highly customized prosthetic components. However, the global burden of amputations falls most heavily in areas that lack access to volumetric medical imaging. A portable system for extremity tomosynthesis could find use in the design of custom prosthetics.

Tomosynthesis of the knee and hands has also been proposed [84, 50] as a mechanism to study the progression of arthritis and osteoporosis.

1.3 Technical Background

In this section I discuss the physical processes by which medical x-ray images are acquired, and how x-ray production is achieved, and relevant advances in ultraviolet photocathode technologies.

1.3.1 X-ray images

X-ray is a common term of energetic electromagnetic waves with a wavelength of 10^{-11} to 10^{-8} meters, or equivalently, photons in the 100 to 100,000 electron-Volt energy range.

X-ray tubes have been in use since the late 1800s for a variety of applications. Though the size and exact function of x-ray tubes vary greatly, they all share two basic components: an electron source, and a target held at a high potential positive with respect to the electron source [139]. The potential difference between the anode and the cathode draws electrons from the electron source and accelerates them towards a

metal anode target, such as tungsten or molybdenum. The electron beam's interaction with the target metal generates x-rays. Both transmission-type and reflection-type geometries are used, the latter to create an anisotropic source at an angle to the electron beam axis. Physically, the emission of x-rays is caused by the rapid deceleration of electrons that impact the target, a process known as Bremmstrahlung radiation, and by the ejection of electrons from the k- or l-shells of the target metal. Many implementations of x-ray tubes include a method for managing the heat buildup in the target, by liquid-cooling or rotating the target.

Conventionally, the electron source in medical x-ray tubes is a type of thermionic source, in which a filament (often tungsten) is heated, ejecting electrons from its surface. This occurs once the electrons have enough thermal energy to overcome the work function of the metal. For tungsten, this occurs at temperatures above 2200 degrees C [132].

In medical x-ray tubes, a molybdenum cup is commonly used to focus the ejected electrons onto the target anode. This focusing enables a small spot size.

X-ray imaging has a wide variety of uses in medicine. In this thesis, I focus on three applications in particular: radiography, mammography, and computed tomography (CT). X-ray radiography is used to diagnose orthopedic injuries, tuberculosis, and many emergent conditions.

Mammography is an x-ray screening technique for breast cancer [105], the second leading cause of death for women in the US. CT has a wide variety of uses, mostly notably in stroke and TBI management. Application of CT were covered in detail in the preceding sub-section.

X-ray imaging follows Beer's law,

$$I = I_0 e^{-\mu l} \tag{1.1}$$

where I is the irradiance on an image sensor, I_0 is the irradiance on the attenuating object, μ is the linear attenuation coefficient of the object, and l is the propagation distance through the object. The attenuation of a given tissue type is dependent on

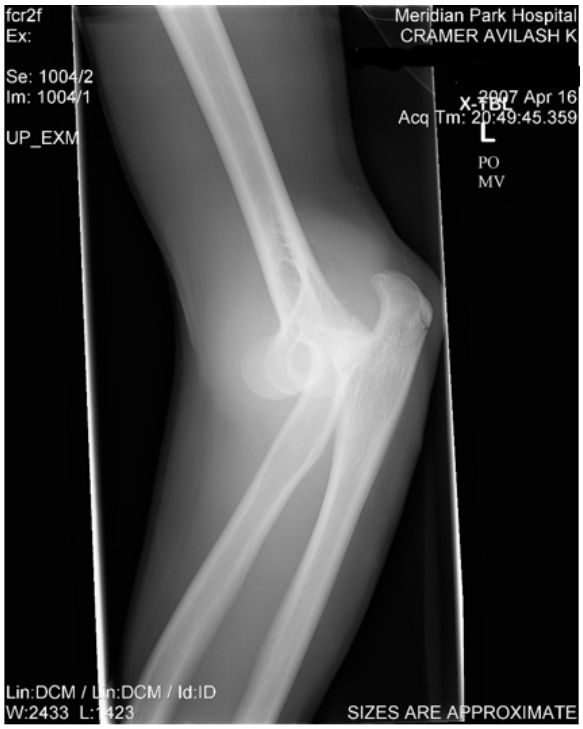

Figure 1-1: X-ray radiograph of the author's arm following a regrettable rock climbing incident.

its density and effective atomic number [132]. When the x-ray path contains multiple materials, Beer's law can be expressed as

$$I = I_0 e^{\sum_i \mu_i l_i} \tag{1.2}$$

Different x-ray attenuation by different tissue types provides contrast in x-ray imaging.

In digital x-ray imaging, a detector element collects charge generated by photons. Recording x-ray photons is a non-trivial affair. For both digital and film radiography, there is a need to down convert from high energy x-ray photons to optical photons in order to generate an image. High energy photons have a low probability of interacting with a thin sheet of film, and can damage the charge collecting pixel detectors (which,

in any case, do not work well at x-ray energies). A separate material is needed- one that can both stop the x-ray photons and produce optical photons, which are easily imaged with either film or a digital detector.

Stopping x-rays and producing visible light is accomplished using a crystal known as a scintillator (also referred to as a phosphor). Scintillators for a given x-ray application are chosen such that even a thin sheet will have a high stopping power for x-rays at the energy used. Generally, scintillators used for medical imaging emit around 500 nm $\pm$ 100 nm. Some common scintillator choices include Cesium Iodide, CsI, and Gadolinium oxysulfate, Gd_2O_2S (GOS). GOS in particular is frequently doped to alter its absorption and emission profiles; terbium and praseodymium are common dopant choices for radiography and computed tomography, respectively. A table of the properties of scintillators commonly used in medical imaging is below, adapted from [28].

Table 1.1: Common scintillators in medical imaging

Name	Formula	Application	Speed (s)	Emission Peak (nm)
Gadolinium Oxysulfide (Terbium)	Gd_2O_2S:Tb	Radiology	$3 * 10^{-3}$	540
Barium Fluorobromide	BaFbr:Eu	Radiology	$8 * 10^{-7}$	390
Cesium Iodide	CsI	Radiology	$9.8 * 10^{-7}$	550
Cadmium Tungstate	$CdWO_4$	CT	$1.4 * 10^{-5}$	480
Yttrium-Gadolinium Oxysulfide	$(Y_3Gd)_2O_2$:Eu	CT	$1 * 10^{-3}$	611
Gadolinium Oxysulfide (Praseodymium)	Gd_2O_2S:Pr	CT	$3 * 10^{-6}$	513
Sodium Iodide	NaI:Tl	Nuclear Cameras	$2.3 * 10^{-4}$	415
Bismuth Germanate	$Bi_4Ge_3O_12$	PET	$3 * 10^{-7}$	480
Gadolinium Orthosilicate	Gd_2SiO_3:Ce	PET	$4 * 10^{-8}$	430

Scintillator speed is another important factor to consider. Imaging techniques that rely on photon-counting principles, such as Positron Emission Tomography (PET), are reliant on a detector with good temporal resolution. The speed listed above refers to rise time- scintillators can have a slow turn-off time, even though they may respond

quickly to an initial photon.

We used a cesium iodide-based imaging system in our experiments, due to its speed and the fact that it is a very common choice for radiography and fluoroscopic imaging.

1.3.2 X-ray production

Bremsstrahlung X-ray production can be broken down into two stages: electron production, and electron acceleration and braking. I will discuss the acceleration and braking stage first; electron production is discussed in 1.3.3.

Emitted electrons are accelerated towards a metal target through a high voltage. Common target materials for medical imaging include tungsten, molybdenum, and rhodium. Accelerated electrons striking a metal target will emit a spectrum of x-rays across a spectrum of energies. This spectrum is known as the Bremsstrahlung spectrum, and is dependent on the energy of the incident electrons, as well as the target material. The variation in emitted x-ray energy is due several factors. A representation of the Bremsstrahlung interaction is shown in equation 1.3.

$$A + e^- -> A + e^- + \hbar\omega \tag{1.3}$$

where A is the metal atom, e^- the incident electron, and ω the frequency of the emitted x-ray. Electrons expend their kinetic energy over the course of several interactions at varying distances from the nuclei of the target metal. Accordingly, the x-ray photons are produced at varying depths from the target metal nuclei.A complete quantum electrodynamics model of Bremsstrahlung radiation has been described by [10], [69], and others.

For medical applications, the energy spectrum of emitted electrons from an x-ray source is of critical importance [132]. The maximum wavelength of emitted Bremsstrahlung radiation from an x-ray tube is given by the Duane-Hunt limit,

$$\lambda_{max} = \frac{hc}{eV} \tag{1.4}$$

where h is Planck's constant, c the speed of light, e the charge of an electron, and V the tube voltage [106]. The emitted Bremsstrahlung spectrum is given by Kramer's rule

$$I(\lambda)d\lambda = \frac{KiZ}{\lambda^2}(\frac{\lambda}{\lambda_{max}} - 1) \tag{1.5}$$

where $I(\lambda)$ is the x-ray intensity at a wavelength (λ), K is a constant, i the tube current, Z the atomic number of the target, and λ_{max} given by 1.4. This can be rewritten somewhat more intuitively in terms of photon energy E:

$$I_E = KZ(E_M - E) \tag{1.6}$$

where I_E is the intensity of photons at an energy E, K a constant, E_M the energy of a photon with wavelength λ_{max} [65]. However, for medical imaging, low energy x-photons are filtered out by a window such as Be, Al, or Mo, depending on the application. This dramatically alters the spectral profile at lower energies.

As the Duane-Hunt limit states, for an x-ray source, the tube voltage (reported as kVp, or 'peak voltage') sets the maximum x-ray energy, not the average energy of emitted x-rays. A good rule of thumb is that the average x-ray energy (in electrons-Volts) from Bremsstrahlung sources is about one third of the peak voltage [65].

In addition to the Bremsstrahlung spectrum, a second type of x-ray emission is produced when the incident electrons ionize the target material, often by displacing an electron in the k- or l- shell of the target metal. This process produces narrow, high-intensity peaks of x-ray radiation at discrete points along the energy spectrum. This k- or l-line emission is primary source of radiation for certain applications such as mammography. This is accomplished by using a filter (usually a thin sheet of metal) to remove much of the Bremsstrahlung radiation [132].

Common target/filter combinations for mammography include molybdenum/ molybdenum, molybdenum/ rhodium, and rhodium/ rhodium. While Mo/Mo has been reported to have the highest contrast-to-dose ratio in mammography, a system using rhodium (Z = 42) filters or anodes has a spectrum that has more energetic photons

Table 1.2: K-line of common anode element choices for x-ray imaging

Atomic Number	Element	Ka1 (keV)	Ka2 (keV)	Kb1 (keV)
42	Molybdenum	17.47	17.37	19.63
45	Rhodium	20.21	20.07	22.72
74	Tungsten	59.32	57.98	67.24
75	Rhenium	61.14	59.72	69.31

than a molybdenum filtered tube, so it may be more appropriate for a dense or large breast [40].

In radiography and CT, x-ray photons usually need to penetrate the bone and tissue that comprise the head, chest, and/or abdomen. Since this requires a more energetic photon spectrum than mammography, molybdenum is not a useful choice of target. Common targets for radiography and CT include tungsten (Z = 74) and a 10%/90% rhenium (Z = 75) tungsten alloy. For thermal management reasons, a common anode design has a rhenium/tungsten surface on top of a molybdenum or graphite core. Aluminum (Z = 13) is a common filter choice for radiography and CT applications. Bremsstrahlung radiation (as opposed to characteristic ionization radiation) is the significant contributor to the x-ray spectrum in radiology and CT [132].

The width of the electron beam, and the angle between the electron beam and the anode target determines the focal spot size, which determines the maximum resolution of the resultant image. For radiography and computed tomography, a small spot size is less important due to blurring from scattering within the body; however, for mammography, which hinges on the accurate discrimination of tiny features, a small spot size is critical [89].

Table 1.3: Tube voltages and spot sizes for different medical x-ray applications

Application	Spot Size (mm)	Tube Voltage (kV)
Mammography	$>$0.1	$\sim$17
Radiography	1-10	30-120
CT	1-10	150

1.3.3 Electron generation techniques

The other stage of x-ray generation is the production of electrons that are then accelerated towards the anode. In conventional x-ray tubes, electron generation is accomplished by running current through a thin tungsten filament. The current density J in a thermionic filament follows the expression

$$J = (1 - r_{av}) A_0 T^2 e^{\frac{-\phi}{kT}} \tag{1.7}$$

Where T is the temperature of the filament, r_{av} the reflection rate of electrons at its surface, ϕ the work function of the filament material, k the Boltzmann constant, and A_0 a constant.

While thermionic electron sources can reliably produce a large electron flux (up to 1 amp per square centimeter), they are themselves large and have substantial power requirements, and cannot be pulsed quickly. A number of alternative x-ray generation arrangements have been proposed for use in non-rotating CT, and are in various stages of development.

Field emission is an alternative to a thermionic filament or a photocathode (see section 1.3.4). In field emission, a large electric field (rather than temperature) is used to overcome the work function of a material, thereby ejecting electrons. The current density in field emission source is described by the Fowler-Nordheim equation:

$$J = a \frac{F^2}{\phi} e^{-\frac{b\phi^{\frac{3}{2}}}{F}} \tag{1.8}$$

where a and b are constants and F the applied electric field. Unlike thermionic sources, field emission sources can be very small (nanoscale), can have a rise time as low as 50 microseconds [101], and can run at low temperatures. A large body of research centered around carbon nanotube (CNT) field-emission sources.

CNT x-ray sources have been demonstrated in various incarnations since the 90s [136]. CNT x-ray sources typically implement a triode-like gating system, where the cathode is molybdenum substrate with the CNTs deposited on top, and the gate a metallic (often tungsten) mesh. Controlling the potential of the mesh controls the

electron generation.

CNT sources can have exceedingly small spot sizes, allowing for very high resolution x-ray imaging However, building a CNT source that is reliable, rapidly pusable, and has a small form factor continues to be a significant engineering challenge. Few, if any, miniaturized, pulseable carbon nanotube based field emission sources have been brought to market [101].

Non-rotating tomosynthesis systems based off of arrays of gated CNT sources have been demonstrated for several different applications. In particular, CNT sources have seen success in micro CT imaging of mice [76] and teeth [109], and breast tomosynthesis [110].

A 2014 feasibility study [125] determined that CNT sources could be used for non-rotating CT, and a subsequent 2015 PhD thesis [124] demonstrated chest tomosynthesis using a CNT array. A review published this month notes that "Conceived less than 20 years ago, CNT-enabled X-ray sources are now being manufactured on a commercial scale and are powering both research tools and experimental human imaging devices" [109]. It seems quite likely that, at least in the near term, CNT field emission sources will continue to lead the way in non-rotating x-ray tomosynthesis.

Nonetheless, CNT sources do have a number of challenges, including source stability [148], reliability [12, 115], and most significantly, an involved manufacturing process. For these reasons, we opted to explore photocathode based x-ray sources.

1.3.4 Ultraviolet Photocathodes

Much work has been done on photocathode design in the 112 years following Einstein's description [30] of the photoelectric effect. An excellent review of photocathode types is provided by [77], who subdivides photocathodes into two broad categories: metallic cathodes, and semi-conductor cathodes.

In photocathode emission, an incoming UV photon promotes an electron from the valence band on the photoemissive substance into the conduction band. If the electron has enough energy to overcome the work function ψ of the metal, it can be ejected as a free electron. In metals, the valence band overlaps the conduction

band, so there will be a considerable number of electrons in the conduction band. Scattering within the conduction band creates a short escape depth, so that electrons from more than a few nm below the surface of the magnesium do not contribute to the photoemission process. By contrast, semiconductors have a significant band gap, so the conduction band is sparsely populated. Because of this, the electrons from deep within the semiconductor material can contribute to photoemission.

The number of photo-electrons a material ejects for a given illumination is known as the quantum efficiency (QE), typically define in this context as

$$QE = \frac{\#e_{emitted}{}^{-}}{\#\gamma_{incident}} \tag{1.9}$$

Where $\#e_{emitted}{}^{-}$ is the number emitted of photoelectons and $\#\gamma_{incident}$ is the number of incident photons. Many semiconductor cathode materials can provide a much higher QE than metallic cathodes at ∼250 nm. Cesium telluride (Cs_2Te), in particular, is of note as a very high QE cathode material [108, 85]. Unfortunately, it has a shorter lifetime than the metallic cathodes, has a complicated and expensive production process, and has severe handling constraints. Exposure to vacuum pressures as high as 10^{-7} Torr - which is still lower than many turbopumps can achieve - would be enough to ruin the cathode. Metallic cathode materials with a relatively high QE at ∼250 nm include samarium, barium, and yttrium [77, 85]. However, they all have special handling concerns. Barium in particular is especially reactive, and behaves poorly in the presences of electromagnetic fields.

We opted to use magnesium as our cathode material in this project. Magnesium has a relatively high QE at wavelengths of ∼250 nm [99, 77, 85], is very abundant, and has relatively few special handling concerns[7]. A magnesium photocathode will slowly absorb oxygen, and oxidize into MgO [153, 134], but the process is fortunately self-limiting [93]. This gives magnesium cathodes a long lifetime, and allows them to be exposed to atmosphere for short periods of time without catastrophe. Laser cleaning of magnesium [99, 104, 133] has been reported to greatly improve (by a

[7]There are still a few hazards: vaporized magnesium is a respiratory irritant, and powered magnesium can oxidize rapidly in water.

factor of up to 10x) the QE of magnesium photocathodes, although this improvement of efficiency would be ruined by any exposure to all but the tightest of vacuums.

The efficiency of a metal photocathode is dependent on the thickness of the metal layer, but only for very thin films. For layers greater than 100 angstroms in thickness, the QE of the cathode is generally thickness-independent [6, 103].

A rapidly pulseable, photocathode based x-ray source in the 1-10 keV range was developed at the Goddard Space Center to test and calibrate the Neutron star Interior Composition Explorer (NICER), a payload recently installed on the International Space Station [38, 44]. NICER is an astrophysics sensing package designed for the study of pulsars, which emit radiation in the soft x-ray range. This calibration source was a starting point for the work developed in the course of this thesis.

While the most popularized and mature field emission x-ray sources are based on carbon nanotubes, other field emission architectures include zinc oxide and silicon chips have been around for decades as electron sources in various applications.

Chapter 2

Cold-cathode X-ray source design

2.1 Stationary Computed Tomography for Space and other Resource-constrained Environments

In this section I discuss the development of a small, pulseable, metallic cold-cathode x-ray source, and its use in a prototype tomosynthesis module. This source was important not just as a demonstration of metallic cathodes as the electron generation mechanism for an x-ray source, but also because it provided a test bed for much of the rest of the work done in this thesis.

Adapted from **Stationary Computed Tomography for Space and other Resource-constrained Environments**, Cramer et al, Scientific Reports (2018).

Abstract

Computed tomography (CT) is used to diagnose many emergent medical conditions, including stroke and traumatic brain injuries. Unfortunately, the size, weight, and expense of CT systems make them largely inaccessible for patients outside of major hospitals. We have designed a module containing multiple miniature x-ray sources that could allow for CT systems to be significantly lighter, smaller, and cheaper, and to operate without any moving parts. We have developed a novel photocathode-based x-ray source, created by depositing a thin film of magnesium on an electron multiplier. When illuminated by a UV LED, this photocathode emits a beam of electrons,

with a beam current of up to 1 mA. The produced electrons are accelerated through a high voltage to a tungsten target. These sources are individually addressable and can be pulsed rapidly, through electronic control of the LEDs. Seven of these sources are housed together in a 17.5 degree arc within a custom vacuum manifold. A full ring of these modules could be used for CT imaging. By pulsing the sources in series, we are able to demonstrate x-ray tomosynthesis without any moving parts. With a clinical flat-panel detector, we demonstrate 3D acquisition and reconstructions of a cadaver swine lung.

Introduction

Roentgen's discovery of "A new kind of ray" or x-ray ("for the sake of brevity") ushered a new field of medical imaging that is still continuing to advance at a rapid pace [116]. X-ray computed tomography (CT), is a volumetric imaging technique in which a tomographic image is reconstructed from hundreds of projection x-ray images taken at different angles around the subject. It is the first line imaging modality for diagnosing a wide variety of illnesses and injuries [43, 100, 36, 119]. Modern CT scanners employ one or two x-ray sources mounted on a rotating gantry. As the gantry revolves around the patient (at speeds up to 300 revolutions per minute), the system acquires x-ray projections from multiple angles that are processed to generate a volumetric image [62, 132]. The rotating gantry mechanism represents a considerable portion of the mass, size, and power requirements of a conventional CT scanner, hindering its application in resource-constrained environments; the rotating system's large net angular momentum further reduces its suitability for use on board a spacecraft [147, 49, 35]. We describe a non-rotating CT system composed of multiple photocathode-driven x-ray modules that can be assembled into a ring or other geometry for tomographic imaging.

CT is used in the management of many injuries and disease, such as aortic dissection, pericardial tamponade, cancers, and many others. Two classes of emergent conditions where are CT is particularly vital are strokes, and traumatic brain injuries (TBI).

As per the stroke management guidelines [43] at the Massachusetts General Hos-

pital, patients with symptoms indicative of a stroke first receive a non-contrast CT to determine if the stroke is haemorrhagic or ischemic, and to rule out a non-stroke pathology (a 'mimic', such as hypo/hyperglycemia, epilepsy, multiple sclerosis, and intracranial tumors). In the case that the stroke is ischemic, patients receive an intravenous contrast injection, and CT angiography is performed. This is done to visualize the occlusion in the artery, and the extent of the affected arterial territory. Such advanced imaging is performed to determine the extent of tissue death, and to determine whether a given patient is a candidate for more invasive, mechanical removal of a thrombus/embolus. Variations of this protocol are used in hospitals around the world [131, 57, 14, 121, 78]. Given the importance of CT in stroke management, and the widespread prevalence of strokes, a CT scanner that is portable and can be deployed in a variety of clinical setting is highly desirable. Such a scanner would allow doctors to distinguish between haemorrhagic and ischemic strokes, and in the latter case, deliver thrombolytic drugs in the field.

CT also plays a large role in clinical management of TBI. In the first 24 hours following a head injury - and if imaging is indicated - CT is the preferred neuroimaging technique. CT is best imaging tool for detecting skull fractures, various forms of intracranial hemorrhages, and other rapidly emergent conditions that may require immediate intervention [152, 100].

However, even in high-income nations, CT systems are generally only available in major trauma centers and hospitals, and need to be supplied with continuous, 3-phase power. This lack of portability not only makes advanced healthcare delivery in rural communities challenging, it affects pre-hospital care in essentially all demographics. Worldwide, some three-quarters of the global population has no access to medical radiography of any kind, let alone computed tomography. The disparities in access for volumetric imaging are even more acute: in OECD countries, there is an average on 1 CT scanner per 65,000 people, while in low-income countries (Defined as having a per capital Gross National Income of less than $1005), there is one CT scanner per 3,500,000 people [95].

In the military sector, aircraft carriers, mobile forward surgical teams, and forward

operating bases, generally operate without a volumetric medical imaging capability, despite performing surgeries that would routinely be accompanied by volumetric imaging in the civilian world [36, 71, 4] (during the Iraq war, one mobile forward surgical team in Mosul was occasionally equipped with a single CT system). A CT system that is light weight and modular - and can be broken down into man-portable components and assembled in the field - might be able to bring volumetric imaging closer to the battlefield.

Extended space missions represent another use case for a portable tomographic imagining system. A manned mission to Mars, for example, will take hundreds of days at the minimum [147], and having advanced radiographic imaging capabilities could be a substantial benefit for the crew members of such a mission. Currently, radiographic imaging on the International Space Station is limited to ultrasound [35]. Unfortunately, a conventional CT system is not an option, due to its weight, and the fact that a rotating gantry would impart an equal and opposite rotation upon the spacecraft. A light-weight, motion-free, modular tomographic imaging system could address these issues.

Results

We demonstrate an x-ray source module consisting of a set of seven x-ray elements that can be turned on or off rapidly, in a programmable fashion, for distributed generation of x-rays from multiple points in space without any mechanical motion. The x-ray elements in this source module are miniature x-ray sources that are triggered by ultraviolet light. The UV light shining on a photocathode generates a small number of electrons by photo-emission. As depicted in Fig. 1, the photo-electrons are amplified using a high-gain electron multiplier and accelerated through a high voltage to a tungsten target. In the following subsections, we describe each of these components of our distributed x-ray source that enables multi-source motion-free tomography. Salient features of this design, as illustrated by various characterization experiments that we have conducted, are then described. The results of tomographic image reconstruction are illustrated with cadaveric specimens. Finally, we discuss what it would take to scale our prototype scanner to full-body human scanning.

Electron Production

In conventional x-ray tubes, electrons are generated by heating a tungsten filament by running current through it. While thermionic electron sources can reliably produce a large electron flux (up to 1 ampere per square centimetre), they are large, have substantial power requirements, and cannot be pulsed on and off quickly due to their thermal inertia. A number of alternative x-ray generation arrangements have been proposed and are briefly described below in order to motivate the design choices made in our prototype.

Field emission is one alternative to thermionic electron generation. In particular carbon nanotube (CNT) field emission x-ray sources have been demonstrated since the 90s [136]. Non-rotating CT systems using carbon nanotube field emission sources have been proposed [125, 124].

CNT sources can have exceedingly small spot sizes, allowing for very high resolution x-ray imaging. However, CNT sources do have a number of challenges, including source stability [148], reliability [12, 115], and most significantly, a complex manufacturing process. CNT sources are destroyed by even a brief exposure to pressures above a high vacuum. Because of these difficulties, few, if any, miniaturized, pulseable CNT-based field emission sources have been brought to market [101].

Another alternative technique of electron generation is to use a photocathode. In photocathode emission, an incoming UV photon promotes an electron from the valence band on the photoemissive material into the conduction band. If the electron has enough energy to overcome the work function ψ of the photoemissive material, it can be ejected as a free electron.

In the proposed design, we use a metallic photocathodes as it has several advantages for our particular application. While semiconductor and bi-alkalide photocathodes offer a better quantum efficiency (QE) in the UV range than metallic photocathodes, they are generally difficult to produce, are intolerant of pressures greater than 10^{-9} Torr, and are degraded by exposure to air [85, 99]. By contrast, metallic photocathodes are robust, easy to deposit, have a long lifetime, can survive being briefly brought up to atmospheric pressure, are intrinsically radiation hard, and

feature a sub-picosecond response time for fast pulsing.

We used magnesium as our photocathode material illuminated by an LED emitting ∼255 nm UV light. Magnesium has a relatively high quantum efficiency (QE) at the chosen UV wavelength, is very abundant, and has relatively few special handling concerns [99, 77, 85]. A magnesium photocathode will slowly absorb oxygen, and oxidize into MgO. This process can occur even in low vacuum. Although in special circumstances this oxidation can actually increase the quantum efficiency of a magnesium photocathode, in general, it will reduce it. However, the oxidation process is fortunately self-limiting and occurs over a course of years even at atmospheric pressure, and much more slowly in vacuum [153, 134, 92].

Unlike CNT-based sources, the proposed distributed X-ray source does not require ultra-high vacuum. For example, we have operated it at 10^{-6} to 10^{-7} torr for over one year without any cathode failure. Our cathode can even survive exposure to full atmospheric pressure for short durations, allowing for easy repair and replacement within the housing. By contrast, a CNT source would be irreparably damaged if it were exposed to even low (10^{-7} torr) vacuum. For our source, a turbopump is sufficient to maintain vacuum; a diffusion pump or an ion pump, which are more complex and less portable, are not required.

Electron Amplification

Metallic photocathodes produce too weak a photocurrent to be directly used for human-scale CT. Human imaging typically requires hundreds of milliamperes of x-ray tube current while a photocathode can generally produce only a fraction of microampere. To amplify the photocurrent, we used a Channeltron^{TM} electron multiplier (Magnum 5900) with an adjustable bias voltage of 2500 to 4000V. Originally developed for mass spectrometry, a Channeltron consists of a set of tightly wound spiral capillaries made of glass. The capillaries are coated with an emissive layer and supplied with a bias voltage that propels the injected electrons forward. The electrons produced by photoemission are injected into the input end of these capillaries. They bounce repeatedly from the walls of the Channeltron, with each interaction producing more electrons, before they exit from the output end. We constructed a photocathode

by depositing a thin layer of magnesium on the input window of the Channeltron using a thermal evaporator (Denton Vacuum systems, 505-A). The deposition process, described in greater detail in the Methods section, is simple, inexpensive and takes less than one hour.

The Channeltron amplifies the current produced by the photocathode on its input surface by a factor of up to 10^8. As a result, the individual source elements can produce up to 1 mA of tube current. This tube current can be modulated by changing the bias voltage or input illumination of the Channeltron. Since the Channeltron is inside the vacuum manifold, programmable UV light stimulus to the photocathode at the input window of the Channeltron is provided by a 255 nm UV LED (Thorlabs Ball Lens LED250J) through a quartz window.

X-ray production

In conventional x-ray tubes, and in the distributed x-ray source proposed here, electrons are accelerated as they fall down the voltage gradient between the cathode and the anode. Typical accelerations voltages vary from few thousand to millions of volts, depending on the application and the desired x-ray energies. Medical x-ray tomography typically uses tube voltages between 17 kVp (for digital breast tomosynthesis) and 140 kVp (such as in pelvic CT). Common target materials for medical imaging include tungsten, molybdenum, and rhodium. Accelerated electrons striking a metal target will emit x-rays over a range of energies dependent on the energy of the incident electrons and the energy levels of various electron shells of the target material. In general, this spectrum consists of a Bremsstrahlung background with superimposed emission line spectra of the anode material.

In the proposed design, an adjustable high positive voltage, up to 35-40 kVp is applied to an anode target made of tungsten. The electrostatic field created by the positively charged anode accelerates the electrons from the output of each Channeltron, which is grounded. X-rays are generated as the high-energy electrons strike the anode. Because the heat is deposited at multiple anode targets, there is no need to physically rotate the individual targets for cooling.

Source Module and Vacuum Manifold

We constructed a module consisting of an arc of seven of these photocathode-based x-ray elements inside of a vacuum manifold (Fig. 2 and 3). The module spans 24 degrees of an arc, with the inner circle measuring 227.5 mm in radius. The seven x-ray elements span the middle 17.5 degrees of this arc. A full ring of these modules would have 15 modules, an outer diameter of 57.0 cm and inner diameter of 38.8 cm. Such a source ring is coupled with an adjacent concentric ring of detector arcs or flat-panel detectors. The x-ray sources are digitally controlled by the UV LED illumination using a microcontroller mounted on top of the x-ray source module.

The generated x-rays exit the vacuum housing though a beryllium window, directly adjacent to the anode. Beryllium was chosen for its low atomic number (z = 4), and relative stability in atmosphere. A vacuum flange on the rear of the module allows for the housing to be connected to a turbopump.

A vacuum flange on the rear of the module allows for the housing to be connected to a turbopump, which maintains a vacuum of 10^{-7} Torr. A valve allows the vacuum to be maintained even when separated from the turbopump. The vacuum manifold also has a getter for maintaining vacuum allowing it to be sealed off permanently once the desired vacuum is reached.

X-ray source characteristics

The focal spot size measured for the above described source was measured to be approximately 1 mm x 4.5 mm. As mentioned before, each source is capable of approximately 1mA of tube current. Source stability, another important requirement for tomographic imaging, was also measured and can be described in terms of: (1) stability of the photon flux in the X-ray beam, and (2) stability of the beam spectrum.

Our experiments reveal that the X-ray flux, which is proportional to the tube current, is stable over the duty cycle for which sources is intended to be used. In our experience, the beam current can be assumed to be the same from pulse to pulse when the x-ray tube is used for up to several minutes. Over longer periods of operation, with our source, as with most X-ray sources, the X-ray flux does change, primarily because of tube heating. To account for this effect, all CT systems (including ours) have an "air calibration" step where the un-attenuated X-ray beam is first measured

and then used for normalizing each projection.

A second part of x-ray flux stability involves source to source variation in our multi-source setup. While there is a variability of up to a few hundred microamps in the beam current produced by each of the 7 sources for a given bias voltage and input illumination, this variation can be compensated for by adjusting the illumination and/or duty cycle of each source. Our custom-built controller board allows us to control the frequency, duty cycle, and luminance of the pulsed UV LED illumination of each x-ray element in order to achieve a uniform x-ray output from each source.

In order to assess the spectral stability, we measured the spectrum using an Amptek Cd-Te X-ray spectrometer (X123, Amptek Inc., Boston, MA). We found the beam spectrum, which is reflective of the tube voltage and atomic composition of the anode, to be stable throughout imaging. Since the atomic composition of the anode does not change, the beam spectrum is primarily a function of the stability of the power supply used for controlling the anode voltage. Extremely low ripple power supplies are available, and this parameter for our source is no different from any other X-ray source.

Reliability

The proposed distributed source is highly reliable because of the life-time of the metallic photocathodes, the reliability of the electron amplifiers, the large thermal mass of the anode and the fact that it is stationary. The magnesium photocathode will continue to work as long as it is not exposed to air for long durations. The Channeltrons used in our design are rated to work for 10,000 hours in spectroscopy applications, although we have noticed some degradation in Channeltron efficiency across the time-course of a few years. Finally, if the source was sealed, as opposed to being actively pumped, one may have to re-establish the vacuum if it were to decline over time.

Tomographic Imaging

Using a clinical flat-panel detector, we acquired fluoroscopic projection images of a catheter being inserted into the bronchioles of a pig lung (Fig 4A). In order to acquire tomographic images, we simulated a full 360-degree ring of x-ray sources

using a rotation stage for the specimen. For each position of the rotation stage, seven images, one from each x-ray element, were acquired at a tube voltage of 35 kVp. We implemented a Filtered Back Projection (FBP) reconstruction algorithm to create a 3D volumetric images from a series of projection images (Fig 4B and 4C).

The projection images were acquired using a Varian flat panel detector in 2x2 binning mode, for an effective pixel size of 278 microns. The voxel size of the reconstructed pig lung images was 0.45 mm, isotropic. The minimum resolvable feature size in the reported images was 0.6 millimetres. These parameters are quite competitive with the state-of-art CT scanners currently in use. We have imaged cadaveric hand, wrist, knee, bovine lung specimens and qualitative comparison by a radiologist (R.G.) found the imaging to be of comparable image quality.

Scaling up for Full-Body Tomography

The current prototype operates at 40kVp. However, this is only a limitation of the current prototype and can be overcome by increasing the tube voltage to 120 kVp or higher, a number that is more typical of human scanning. Such a scale-up will increase the size of our source. However, as detailed below, a 3-fold increase in tube voltage does not severely impact the size, weight and portability of our design.

Fig. 5 shows a schematic diagram of the system gantry with the key distances marked. Increasing the tube voltage to 120 kVp will necessitate proportionate increase in the distance of the anode (the high voltage component) from the cathode and the housing, specifically the X-ray window. We are currently replacing the HV connection with a candlestick type connector and re-designing the vacuum manifold such that the critical distance between the key components is suitable for high voltage operation. The separation between the anode and the x-ray window and between the anode and rear wall (the critical dimensions) are each about 15 % of the total front-to-back length of the module. To support 120 kV operation, these distances would have to be tripled, increasing the total length by a factor of 1.3. As calculated in our CAD designs, this would increase the weight by approximately 40%, to 1.5 kg per module. Therefore, re-designing our distributed source for voltages traditionally used for medical imaging does not detract from its scalability, portability, and the other

advantages mentioned above.

For comparison, a conventional CT system can weigh over 2000 kilograms, without the patient bed, and occupy a volume of 228 (h) x 188 (w) x 156 (d) cm to provide a bore size of 70 to 80 cm. Even specially designed "portable" neuroimaging CT scanners are nearly 500 kilograms and 153 (h) x 134 (w) x 72 (d) cm for a bore size of 32 cm [21, 22].

For any CT scanner designed for human imaging, the size of the bore is fixed by the anatomy (i.e., head-only, full-body, or extremity-only scanner) and cannot be decreased. Also, the requirements on the patient table are unchanged by the scanner design, as are the requirements on reconstruction computer and power supply. The static CT presented here, however, does decrease the overall weight and size of the scanner because of the following factors: (1) it simplifies the system gantry; (2) it removes the motor and the gear system for rotating thousands of kilograms of mass; (3) it eliminates the high-bandwidth slip ring required for transferring the projection data from the rotating components to the static computer; (4) being motion-free, it simplifies the high-voltage distribution on the gantry; and finally, (5) it eliminates the rotating anode and the elaborate cooling system that is mandated by the high wattage — up to 100 kW or more for a general-purpose, high-end scanner — being dumped at a single millimetre sized focal spot on the anode.

The size and weight implications of these changes are significant. As shown in Fig. 5, the dimension of the overall gantry with the current 7-element modules. — a ring that is suitable for a head-only CT scanner — can be thought of as a donut with a 38.8 cm bore, 57.0 cm outer diameter, 6.9 cm depth, and an estimated weight of 22.5 kg. These specifications are considerably more attractive than the current state-of-art 3rd generation scanners.

While difficult to estimate and compare the cost implications of the above-mentioned simplifications, we expect the static CT system to be cheaper because of it does not need a slip ring, a rotating gantry, and a tube cooling system.

The overall shielding requirements for the proposed system are no different from those of a conventional CT system. However, given the static nature of our design,

the points in space where the radiation is being generated, and the volume that will be irradiated, are fixed in space and time. As a result, one can design a more tailored shielding scheme that is built into the distributed ring of sources. Such internal shielding, which can be quite close to the points of x-ray generation, can be designed to minimize size and weight, a task that we have currently not undertaken.

In regard to scalability and portability, it should be mentioned that scaled-down versions of the traditional rotating CT scanners are available for portable deployment [21]. These scanners typically reduce the bore size of the gantry to a head-only scanner. By virtue of the inverse-square law, the x-ray source power increases as the square of the bore size. Therefore, reducing the bore-size by approximately a factor of 3 results in an order of magnitude decrease in the x-ray source power required for imaging, with concomitant reduction in weight and cooling requirements. The rotational mechanism, along with its power train and slip ring for data transfer, however, persists in these designs. As portability is accomplished by trading off bore size, these designs are not scalable: any increase in bore size, for example to accommodate the whole body, will bring us back to the original heavy, non-portable system. This is well illustrated by the portable full-body portable CT scanners currently available (e.g., the BodyTom^{TM} [22]). These so-called portable scanners, which weigh as much as any other conventional scanner, should be regarded as a traditional CT scanner with a motorized base for in-hospital transportation rather as a portable scanner for field deployment.

Discussion

Our prototype demonstrates several specific advantages that could enable CT imaging in austere environments. Timing of the UV LEDs, rather than current modulation, controls the x-ray flux. The system has no moving parts and each module weighs approximately 1 kilogram. Individual CT modules could be stored and transported in a compact storage box and then assembled in space or in the field for operation. When not in use, the CT system can be disassembled and stored away. Modules can be brought up to atmospheric pressure for repairs and replacement of individual sources.

In the current CT scanners, it is customary to modulate the tube current in response to the changing attenuation as the scanner rotates around a patient. With individually addressable sources that can be pulsed at different duty cycles, it is possible to further reduce radiation dose by selective illumination.

The compact, modular construction of our system would make it easier to combine it with positron emission tomography (PET) for simultaneous PET/CT imaging. Since our system dispenses with the slip-ring and all other moving parts in a CT gantry, tighter coupling between the CT and the PET stages of a hybrid PET/CT scanner would be feasible. Since a rotating gantry cannot be easily combined with the high magnetic field of a Magnetic Resonance scanner, our static CT system opens the door for a portable simultaneous MR/CT system which will have clear applications in trauma, stroke and cancer imaging.

There are several opportunities for improvement in future generations of our current prototype which currently has several limitations that include: the lack of electron beam focusing lens, the low beam current, and a voltage ceiling of 40 kVp. Of these limitations, only the beam current is inherent to the use of a photocathode for electron generation. We are working to redesign the Channeltrons so that they have a thinner profile and incorporate an Einzel lensing system consisting of a series of electrostatic lenses at the output of the Channeltron.

In conventional CT, the image quality is dependent on the integrated photon flux over one rotation. As the rotation time (seconds or s) decreases, the tube current (mA) has to proportionally increase in order to maintain the product mA x s, which provides a measure of the delivered dose. The fastest rotation one can achieve in conventional CT (and accordingly, the minimum scan time) is governed by mechanical considerations with the current state-of-the-art limited to about 5 rotations per second. Beyond this rotation speed, a gantry weighing thousands of kilograms generates insurmountable centripetal force on the x-ray tube, electronics, and other rotating components.

In switching from a mechanical rotation of a 3rd generation CT scanner to the digital control of the proposed stationary CT, we eliminate a fundamental barrier to

faster CT scans. However, even though the mechanical rotation is no longer involved, one still needs to accumulate the requisite photon flux to achieve a given image quality. Higher photon flux for each element in our distributed X-ray source can be achieved by 1) increasing the active surface area of the electron multipliers, 2) optimizing the photocathode deposition process, 3) increasing the multiplier bias voltage, and 4) replacing the 255 nm UV LEDs with a switched 180 nm UV lamp. In addition, even though each source in static CT is weak, there are many of them and they can be arbitrarily and simultaneously turned on or off to provide any coded pattern. The patterns that can be employed for scanning, and the algorithms that can be used to reconstruct tomographic images from these coded patterns, are a topic of ongoing research.

If sufficient flux is achieved, increasing the pulse rate could further reduce the scan times. Currently, the slowest component limiting the pulse rate of the x-ray sources is the set of optoisolators separating the 5V logic and 20V power lines on the LED control circuit (see Methods). These have a rise time of 6 microseconds. A faster pulse rate would allow for faster scan times in tomographic imaging. If the x-ray pulse rate were able to be reduced to the order of a nanoseconds (a capability well within the reach of a metallic photocathode, which has a sub-picosecond response time) time-domain x-ray imaging — with the potential for a dramatic reduction in delivered dose — is feasible [68]. Such time-domain imaging would also allow many recent advances from the LIDAR community to be applied to x-ray imaging.

Reducing the cost of the bill of materials would be an important step in bringing our prototype to the clinic, and would help ensure that it is available to the billions of patients around the world in middle- and low- income communities. One possibility in particular that holds promise is using cheaper LEDs with a broader spectrum and poorer heat management. A broad spectrum is of no particular concern to us, but heat sinking the LEDs and isolating them thermally from the electron amplifiers (which have a highly heat-dependent behavior) would become an important task.

In acquiring tomographic images with a series of miniaturized, photocathode-based sources, we have demonstrated a novel method of volumetric x-ray imaging,

and a fundamental re-imagining of x-ray tomography. We have also demonstrated the utility of a metallic photocathode as the electron generation method for x-ray imaging.

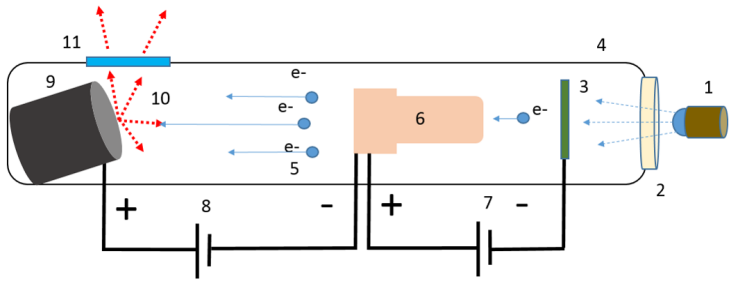

Figure 2-1: Schematic of the miniature x-ray source. A pulsable UV LED (1) emits UV photons which pass through a quartz window (2) into the vacuum manifold (4) and interact with a photoemissive magnesium film (3). This interaction produces electrons which are amplified by a Channeltron device (6), which is supplied with a 3kV bias voltage (7). The amplified electrons are accelerated through a large electric field provided by an external high voltage source (8), and impact on an angled tungsten target (9). This interaction (10) produces x-ray photons which leave the vacuum manifold through a beryllium window (11).

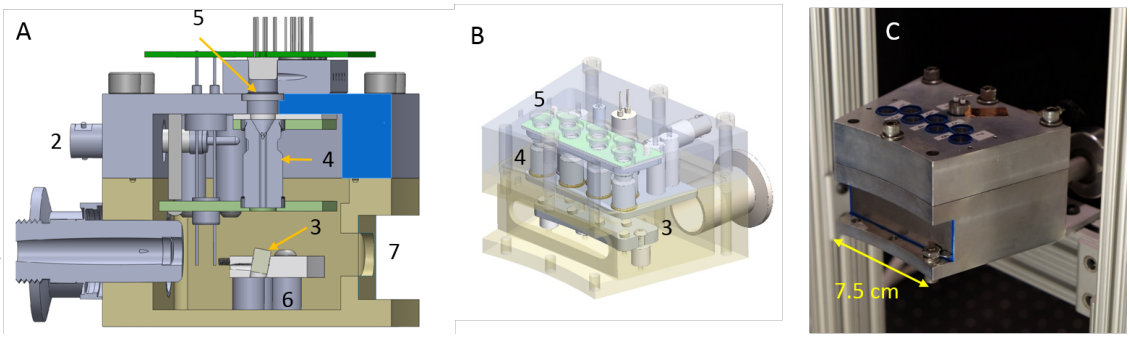

Figure 2-2: A: Cut-through CAD model of the module B: Isometric view with a transparent outer housing C: Completed x-ray module with a beryllium sheet covering the x-ray window.(1) Vacuum connector (2) 3kV bias line (3) tungsten targets (4) Channeltron electron amplifiers (5) quartz windows (6) High-voltage anode plate (7) x-ray window

Methods

Magnesium Deposition

The magnesium deposition was carried out using a thermal evaporator (Denton Vacuum systems, 505-A). Fifty mg pellets of magnesium were placed in a tungsten

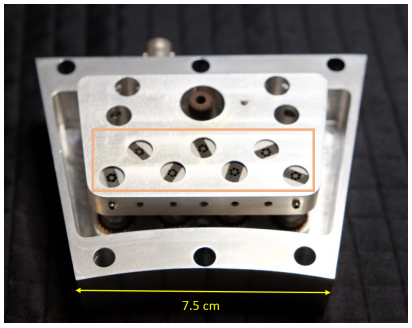

Figure 2-3: Internal view of the module, with the exit ports of the Channeltrons highlighted.

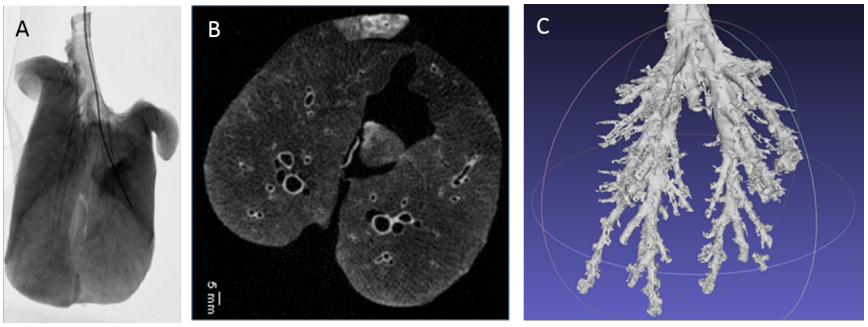

Figure 2-4: A: X-ray projection image of pig lung with an inserted catheter. B: axial slice from pig lung reconstruction. C: segmented bronchial tree from pig lung.

wire basket. The magnesium was vaporized by running 25 amps of current through the tungsten wire for 2 minutes, under vacuum ($< 10^{-5}$ Torr). Foreline pressure on the diffusion pump was maintained with a mechanical roughing pump. Deposition occurred inside of a Pyrex bell jar pumped down to vacuum using a liquid nitrogen-cooled diffusion pump. Individual Channeltrons were wrapped in aluminum foil and held to a rotating stage underneath the tungsten basket with carbon tape. Alongside the Channeltron, a glass microscope slide was placed on the rotation stage to confirm successful deposition.

The chamber (commonly used for gold and carbon coating) was first extensively cleaned to remove the possibility of any contamination with other materials. No other metals (besides magnesium) were used in the chamber after the cleaning process. Cleaning was accomplished in a 3 step process- the chamber was disassembled, and each component scoured with acetone and 800 grit sandpaper. The process was repeated a second time with isopropyl alcohol (IPA) instead of acetone. Finally, each

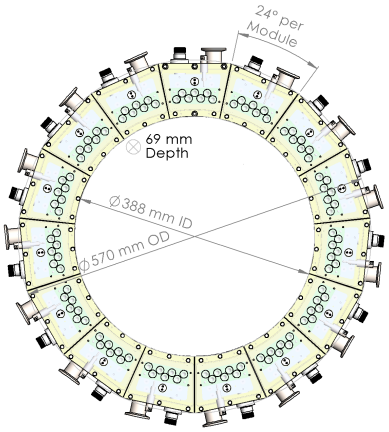

Figure 2-5: CAD diagram of full ring of modules, with dimensions

component in the chamber was scrubbed using IPA and Kimwipes.

A bias voltage of between 3000 and 4000 volts is applied across the Channeltron. An adjustable high voltage between 10 and 40kV is applied from the exit of the Channeltron to the tungsten anode target. The weak electron beam produced by illuminating the magnesium-coated input of the Channeltron with UV light is multiplied up to 10^8 times by the Channeltron. The 10-40kV potential difference between the Channelton output window and the anode accelerates the electrons from the Channeltron and imparts upon them the energy which is partially converted into

x-ray photons at the anode by the Bremsstrahlung process.

UV LED control

We designed a printed circuit board (PCB) to control the 7 UV LEDs. The PCB has two separate circuits: a 20 V power line and a 5 V logic line. The circuit uses a board-mounted Arduino Micro to control the pulses of the UV LEDs, through a bi-polar junction transistor (BJT). The 5V logic lines are kept on a protected ground and separated from the 20 V power lines by optoisolators. A constant current is provided to the LEDs by two constant current diodes (CCRs) in parallel. These units limit the current to a maximum of 100 mA to protect the expensive LEDs, which are limited to 100mA. However, the current provided by the CCRs can be adjusted by a potentiometer in series with one of the CCRs. A visible indicator LED is also in parallel with each UV LED. A high-side current sense chip (LT1787) provides feedback from each LED circuit to the Arduino, and allow us to monitor in real time the response times and current draw of the UV LED. 4-pin phoenix connectors on the top of the board enable transmission and reception of timing signals from the flat-panel detector and a Thorlabs PRM1Z8 rotation stage. The PCB layout was designed using DipTrace, an E-CAD software. The PCB itself was manufactured by Imagineering. Inc.

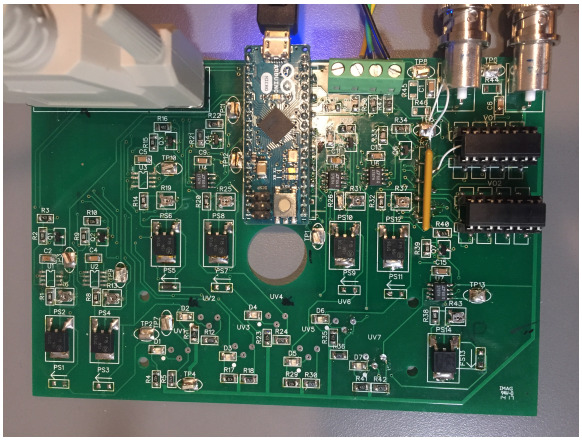

Figure 2-6: Populated LED control PCB

High Voltage Control

The x-ray source is powered and monitored by an integrated, custom built high

voltage system, and controlled by a LabView script. In addition to setting and regulating the high voltage power flowing to the targets and the multipliers, the system has built-in HV fault handling and data logging capabilities. The high-voltage hardware in the unit is controlled via a LabJack UE9 digital/analog IO device. Separate high-voltage power supplies (HVPS) are used to maintain the 10 - 40 kV anode voltage (Matashusada XRT-505) and the 3kV bias on the electron amplifiers (EMCO F30). In addition to the HV power supplies, the high-voltage system contains three relay boards and three low-voltage power supplies (LVPS). One of the LVPS provides 24V to the anode HVPS, and another provides 12V to the amplifier HVPS. The final LVPS provides power for the relays. The relays are controlled through the output ports of the Labjack, a programmable 0-5V output. Two relays control the high-voltage outputs, and a third controls the interlock of the anode 25-50kV HVPS. This HVPS also requires a set-point input, which is provided by amplifying the 0-5V Labjack output to 0-10V. Current and voltage measurements are recorded using the analog input channels on the Labjack.

The LabView VI controlling the high voltage system is designed to be easy to use and to fail safe in the event of arcing. The user interface allows voltage control as well as individual control over the relays in the system. Further, it shows the power supply parameters(actual voltage and current) every 100ms and logs them. It includes features such as overvoltage shutdown, automatic safe-mode in case of interrupted communications, a 10s-watchdog timer and automated data logging. A 50 KΩ ballast resistor, immersed in mineral oil, was added to the output of the power supply to reduce a significant electrical arcing problem. With the ballast resistor, we are able to achieve continuous operation at up to 40kV. Higher voltages will require a significant redesign of the housing module increase the critical dimensions. The aluminum housing has a BNC connector for the multiplier bias, and a silicone connector/cable (MPF, Inc) for the 10-40 kV line.

Anode targets

The tungsten anode rods are held in place by set screws. For ease of machining, we used tungsten carbide rods that were slightly alloyed with cobalt and iron.The

tungsten rods are set at a 10 degree angle to the Channeltrons, and thus the electron beam. This reduces the spot size in one dimension, creating an ellipse.

Geometric Calibration

We are able to obtain the geometric information necessary for image reconstruction in a single acquisition using a custom designed cylindrical 3D-printed phantom. The phantom contains 14 ball bearings embedded in a thin cylinder of ABS plastic. To perform the calibration, images are acquired on the flat-panel detector as the phantom is rotated through different angles for each x-ray source. By tracking the position of the ball bearings as the phantom is rotated, the distances from each source to the detector plane and rotational axis can be determined.

Image Acquisition

Imaging acquisition was done using a Varex Imaging 2530DX flat panel detector, which has a 278 um^2 pixel size in 2x2 binning mode. The panel was synchronized with the control board. After the completion and installation of 7 miniature x-ray sources, we were able to acquire volumetric images of several biological samples. Images processing of the volumetric images was performed using 3D Slicer.

Safety and Handling Vaporized magnesium is a respiratory irritant, and powdered magnesium can oxidize rapidly in water. Diffusion pump oil (used the thermal evaporation system) is also a respiratory irritant, and the diffusion pump must be cryogen-cooled to prevent back-streaming of the pump oil.

2.2 A Digital Pulsed X-ray Source Based upon Si Field Emitter Arrays

The main drawback of the magnesium cathode described in the previous section is its low flux- limited to little over 1 milliamp. One possible solution to that limitation is described in this section: a miniaturized x-ray source based off a silicon field emitter.

Abstract

Despite decades of research and development in cold-cathode field emission de-

vices, modern commercial x-ray sources still mostly consist of thermionic electron emitters. Field emission-based x-ray sources have been demonstrated with high current densities, reasonable temporal resolution and small footprints, but reliability and lifetime concerns have prevented widespread adoption of cold-cathodes. Here, we demonstrate a novel x-ray source based upon silicon (Si) field emitter arrays (Si FEAs) that is small and simple to manufacture as it uses standard silicon foundries and processes. As compared to previously proposed cold cathodes, our Si FEAs offer improved reliability and lifetime. Si FEAs also demonstrate high instantaneous current density and temporal resolution allowing the x-ray source to be operated as a high-flux x-ray source that can be pulsed. Pulsed operation enables a distributed x-ray source with a stationary anode where the anode heat load is managed by turning different FEAs on/off to distribute the heat and allow for cooling. Our Si FEAs can operate even in relatively poor vacuum ($>10^{-7}$ Torr). We demonstrate a high-performance Si FEA based x-ray source which may be used for time-resolved x-ray imaging, or as a distributed source in a non-rotating tomographic imaging apparatus.

Introduction

Most x-ray sources consist of a cathode for electron generation, an electric field in a vacuum manifold for electron acceleration, and an anode for stopping the high velocity electron to generate x-rays via bremsstrahlung and line emission [116]. In such an x-ray generation scheme, the use of field emission cathodes (also known as cold cathodes), as an alternative to the commonly used thermionic cathodes, has been a subject of research for decades [24, 76, 124, 125].

Field-emission cathodes have many advantages over their thermionic counterpart. First, is possible to fabricate field-emission cathodes using low-cost semiconductor batch manufacturing technologies such as silicon wafer processing. They can achieve high absolute current densities of the order of several amperes per square centimeter (A/cm2). Because the emission of electrons is governed by application of an electric field, field-emission cathodes can be turned on or off with nanosecond precision. The rapidity with which they can be pulsed has the potential to increase the image acquisition speed. Their fast pulse rate could also be used for time-resolved imaging

in x-ray domain, or for stroboscopic methods such as dynamic x-ray elastography. Rapid pulsing may also be utilized for more effective beam current modulation with concomitant reduction in radiation dose to the patient.

Multiple field emission cathodes may be used in the same vacuum manifold, enabling spatially distributed generation of x-rays. A promising application of such distributed x-ray generation is in tomographic imaging, e.g., in modalities such as digital breast tomosynthesis [56] and computed tomography [125]. By virtue of distributed x-ray generation, one can eliminate mechanical motion of the gantry and rely upon electronic switching of different x-ray modules. Such simplification of the mechanical gantry has obvious implications on the portability, weight and cost of the overall system.

Many cold-cathode technologies have been demonstrated. These include silicon (Si), carbon nanotube (CNT), zinc oxide, and molybdenum Spindt-type field emitter arrays (FEAs). Unfortunately, despite these promising lab demonstrations, the deployment of cold-cathode x-ray sources has been hampered by their fragility, drift, need for ultra-high vacuum, and modest lifetime over which they function reliably. While much progress has been made, the performance of such systems – which remains inferior to thermionic cathodes for most x-ray applications – has not achieved the original promise of this technology in terms of pulsing frequency, current density, and x-ray focal spot size.

In this paper, we evaluate the performance of a newly designed field-emission cathode using Si fabrication technology. Our new Si field emitter arrays (Si FEAs) was designed to systematically address the root cause of performance lag in the previous field emission based x-ray sources. The key features of Si FEAs are summarized below:

- High emitter density (1 μm pitch) and small gate apertures (200-300 nm in diameter) as the electron source.

- High current densities high, by virtue of high emitter density (108 tips/cm^2), that enables one to use a small cathode footprint and remove any electron focusing optics.

- Small gate aperture for each field emitter tip that enable high current at sub-100 V gate voltage switching.

- High switching speed, which can be attained with conventional pulse generators, due to the low switching voltage required for turning the field emission ON or OFF.

Our x-ray source consists of 3 parts: (a) a vacuum manifold with electrical feedthroughs for the cathode, gate and anode, (b) a Si FEA cathode to generate electrons, and (c) a reflection-type anode. The Si FEA cathode is operated as a pulsed, digital (i.e., the cathode is either ON or OFF) electron source with a fixed duty cycle that mimics the cooling of a rotating anode in a standard x-ray tube. Due to its simplicity, the packaged x-ray source has a reduced form-factor. A 0.5 x 0.5 mm^2 electron source has a thermal spot size of 0.85 x 0.6 mm^2 on the anode (estimated based upon the 45 degree molybdenum anode), and a measured optical spot size of approximately 0.6 x 0.6 mm^2. Therefore, there is negligible spread in the electron beam due to space charge effects and focusing optics is unnecessary. We demonstrate x-ray imaging using this Si FEA based x-ray source and measure its performance characteristics.

Results

Imaging Setup

The imaging setup presented in this paper is a proof-of-concept x-ray source based upon Si FEAs and a reflection molybdenum anode, as illustrated in Figure 4. The setup consists of the x-ray source, imaging sample mounted on a rotating stage and the detector, Varex Paxscan 2530DX. The x-ray source consisted of only an electron source and the Mo anode cut with a 45° angle was positioned 1.5 cm above the source. Connection to the anode was made using a ceramic high-voltage (HV) feedthrough. No focusing optics was used and the structure was enclosed in an vacuum chamber with a base pressure of 10^{-8} Torr and operating pressure above 10^{-7} Torr. The increase in pressure during operating is likely caused by water desorption from the heating of the anode, which is unavoidable without additional equipment, such as a getter, to desorb water vapor from the anode. The three electron sources are Si field emitter arrays described above with a dimension of 0.5 x 0.5 mm^2 and two 1 x 1 mm^2 which can provide a maximum of 20 and 80 mA respectively due to the space charge

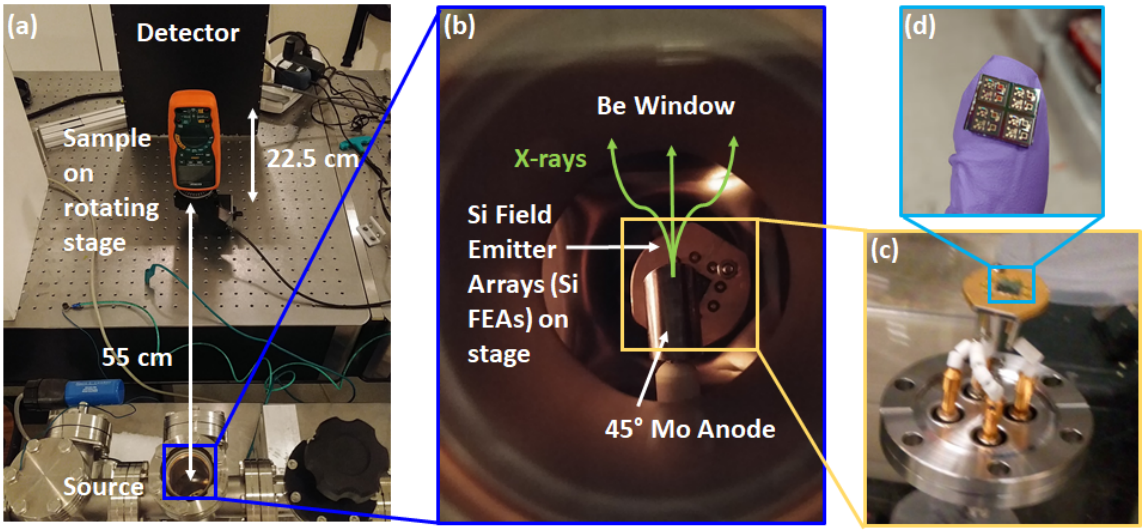

Figure 2-7: (a) Photograph of the x-ray test setup with a multimeter as the test sample which sits on a rotating stage. The source is approximately 55 and 77.5 cm from the sample and detector, respectively. The x-ray source (b) is a bremsstrahlung source housed in a small vacuum chamber with a small ion and turbo pump with a Si field emitter arrays (Si FEAs) as the electron source and a molybdenum anode biased at high voltage; the x-rays travel out towards the sample through a Be window. The base pressure of the system is roughly 10^{-8} Torr and operates at roughly 10^{-7} Torr when active. The (c) electron source is a (d) Si FEA chip containing (Die size: 7x7 mm^2) and three wire-bonded devices. The cathode or substrate of the Si FEA chip is mounted to feedthrough using silver paint and wire-bonds are used to connect the gates to individual feedthroughs

limitation of the chamber; this is the equivalent of 8 A/cm^2.

The electron sources are connected to the power supplies using a 2.75" Conflat miniature high voltage (MHV) vacuum feedthrough which can connect up to 3 sources simultaneously. The Si cathode is connected as a common, grounded substrate bonded using conductive Ag epoxy to a transistor-outline package (Model: TO-3 with 8 leads). Individual electron sources are controlled by their respective gates through a wirebond between the gate and the TO-3 package, and through metal stubs used to connect the lead to the MHV feedthrough. The electrical connections and pulse train for the x-ray setup is shown in Figure 2-7. The anode potential is provided by a DC high voltage power supply, Matsusada XRT-505, and the gate voltage pulsing is provided by an Agilent 8114A high power pulse generator. A small resistor of 50 Ω is connected to the emitter which provides insight into the gate delay of the device under observation

and the current flowing through the emitter. An oscilloscope readout, Figure 5, provides the time-response of the emitter terminal of the device. When the gate is first pulsed, a significant amount of current passes through the emitter. This current is the transient from charging the capacitor between the gate and emitter. Over time, this current decays, resulting in a constant current at the emitter which is equal to the anode current in the absence of gate leakage. This gives an idea of the response time of the device with all of the additional packaging and wire-bonding. Here, we measured the RC delay to be around 100 ns for a 500 x 500 μm^2 device, with a shorter delay expected for the larger 1000 x 1000 μm^2 device due to a reduced impact from parasitic capacitances external to the FEA. Based upon this, it is expected that the field emitter array will output the same amount of current that was previously measured through previous measurements. The device shows the expected current drive of approximately 16.5 mA, well within our device tolerances.

Imaging results

The resolution of the x-ray source was investigated to understand the impact of not having focusing optics. This was performed by putting standard 10 μm slit apertures in front of the x-ray source and measuring the size of the slits on the detector, Fig. 2-8. A 500 x 500 μm^2 array was used as a balance between obtaining a minimum spot size for these sources and getting enough dose through the 10 μm slit to accurately extract the focal spot size. Based upon the magnification (2x), apparent size of the slit and the size of the pixel (130 μm), it was determined that the effective spot size of the 500 x 500 μm^2 source is approximately 600 μm which suggests that while some spreading of the electron beam exists, this geometry is more than sufficient for x-ray imaging applications that do not require a microfocus spot.

Using this source, we could image objects that a standard x-ray source is able to image. Because there is no heat management (such as a rotating anode), and the devices are operating under relatively high pressures ($>10^{-7}$ Torr), pulsed techniques are necessary to improve the reliability of the devices. When the source is on, the anode is heated raising the overall pressure of the chamber due to sublimation of water from the anode. To transmit the maximum power through the source with minimum

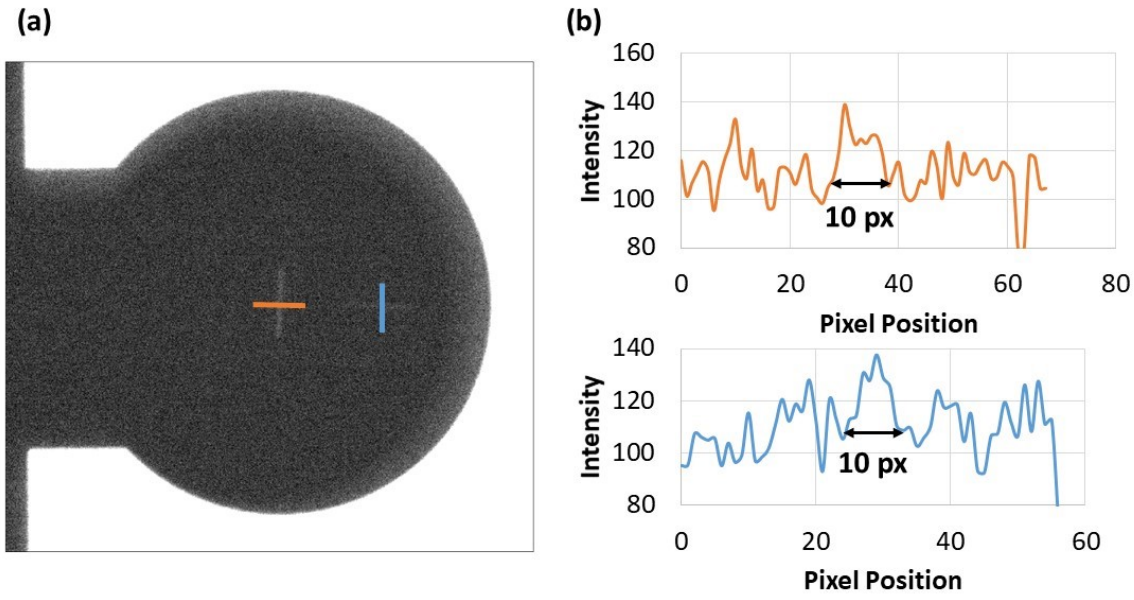

Figure 2-8: (a) X-ray image of two 10 μm slits used to measure the effective focal spot size of the source. The image was taken with a 2x magnification and the 500x500 μm^2 device to test the focal size limitations of the FEAs. (b) Line scans of the intensities were used to derive the focal spot size of the source based upon the number of pixels. It was observed that the worst-case number of pixels is approximately 10 pixels or roughly 600 μm, indicating minimal size increase in the focal spot size despite not having any focusing optics.

water desorption, the sources are operated for a short period of time, normally a few hundred nanoseconds, and are turned off for a few tens of microseconds to cool, much like the pulsed I-V presented above; the cooling effect is equivalent to a rotating anode operating at 50,000 rpm. While this is not optimal for power throughput, it is sufficient to image most objects. Examples of these images are shown for a multimeter showing a clear image with adequate resolution for inspection of the object, Fig. 2-9.

We also demonstrate that a single FEA x-ray source can be used to perform computed tomography by placing the sample on a rotating stage (similar to current commercial designs) and taking a few hundred images, an example of a slice produced from 3D reconstruction is provided in Fig. 2-10. The source is sufficiently reliable to take >300 images of the multimeter, although with poorer quality than the image in Fig. 2-9. While the source was able to image the multimeter, it was not able to maintain the image quality without feedback which was provided manually by

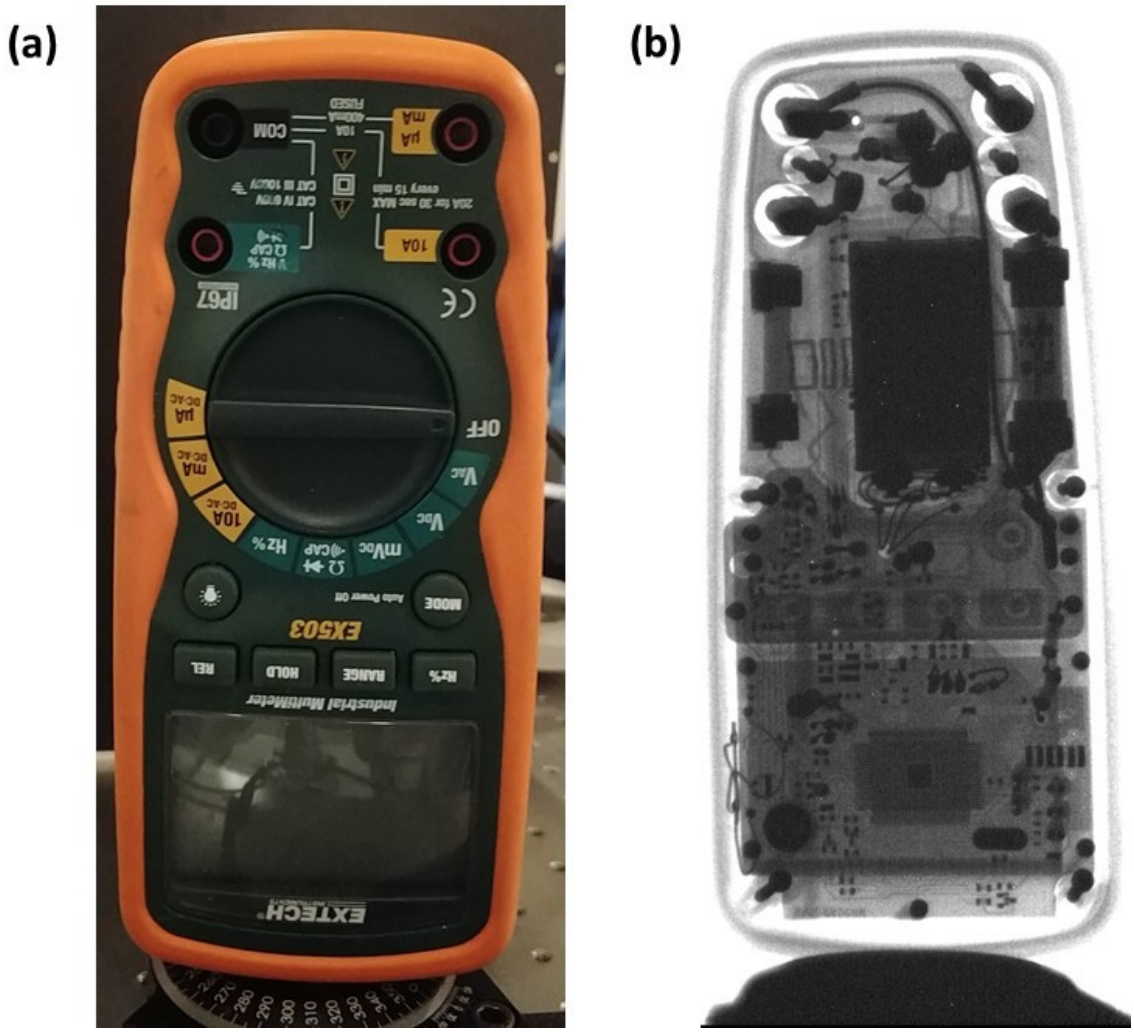

Figure 2-9: . (a) Optical and (b) 2D x-ray image of a multimeter taken using a 1000 x 1000 μm^2 source at 38 kVp with a pulse width of 200 ns, V_G = 57 V and a period of 20 μs. The total exposure time was 1s or 50000 pulses

adjusting the gate voltage, and pulse width due to the high power requirements and eventual degradation in poor vacuum conditions. While this is a testament to the source stability, the device would in principle never be operated at such a short wait time and between images in poor vacuum due to the distributed nature of the source.

Discussion

All of the above design considerations are obvious changes necessary for designing an optimized x-ray source and would improve the properties of the Si FEA based x-ray source beyond its current state. However, the main significance of these proof-of-concept experiments is the demonstration of an x-ray source that can enable dis-

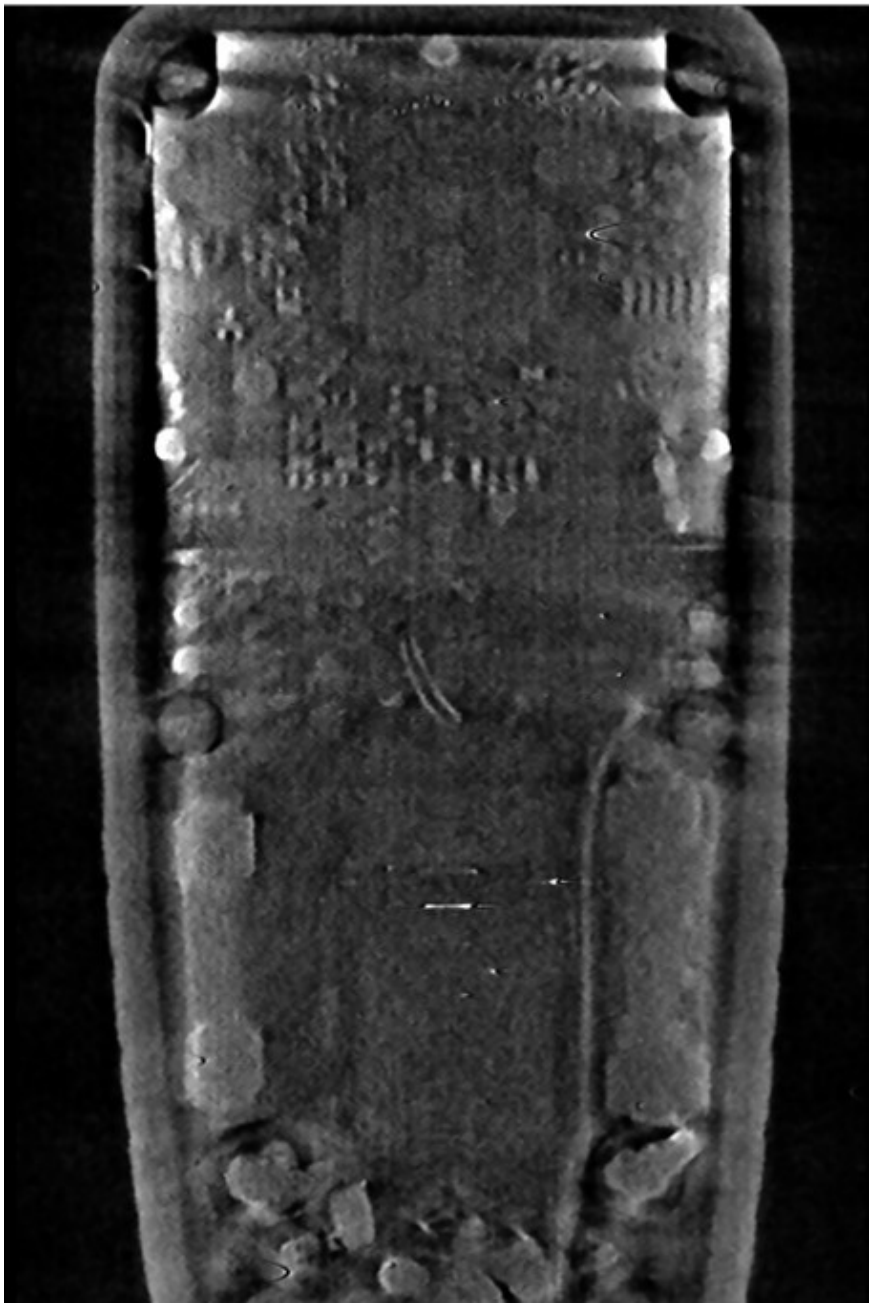

Figure 2-10: Slice of the multimeter from the 3D reconstruction at board level. Bright features indicate the presence of metal which has enhanced absorption relative to other materials in the multimeter

tributed x-ray source systems. Applications that require distributed x-ray sources are any 3D imaging application where the motion of a single source can be replaced by multiple static sources such as conventional CT. Using conventional CT as an example, the design of the system would be changed from a single x-ray source and

detector pair that is rotated to a completely static system with a ring composed of detectors and hundreds of individual x-ray sources.

A number of advantages for this design enable enhanced portability and reduced size, a potential to greatly reduce dose ($>$ 10x) and improve CT speed. The first of these advantages is realized by the removal of the gantry. This enables significant reduction in the weight of the overall system and removes the slip ring required to transmit the detector data at high bandwidth. This mechanical changes also removes the rotational inertia of the system enables the static system to be deployed anywhere such as an ambulance, airplane or on the international space station.

In a static system, all of the sources are individual and electrically controlled with no movement blur. Each source or exposure point can have optimal dose with an optimal filter, and new techniques can be developed to minimize dose or improve the collection speed. Sources with sufficient exposure would no longer need to be pulsed resulting in a more advanced tube current modulation and algorithms could be used to reduce the total number of sources required. It has been previously shown that only 1/10th of the images are required for an adequate CT reconstruction showing that a huge potential to reduce patient dose.

The reduction in dose results in the raw improvement in the imaging speed, but could also be a new feature for improved time-resolved CT imaging. In static CT, the current and the time that the source is on are both parameters. For a constant dose, the source can be on for a shorter period of time reducing the time proportionally the dose that is applied. This new trade-off enables faster CT scans and rotation times proportional to the actual dose required. This provides a new means to improving the rotation time for temporally resolved CT imaging which would be important for imaging key organs such as the heart or lungs, and enables new methods of temporally resolved imaging for breast imaging with speeds far beyond the temporal limit of current approaches. For example, if a current CT requires 1000 images with a fixed dose and rotation time of 250 ms. For an acceptable reconstruction of the 100 most important angles, a CT could be taken at a rate of 25 ms simply by reducing the number of angles taken. This feature provides a powerful new way of gathering

time-dependent data that would not otherwise be possible with conventional CT.

We have not yet exploited the potential of very short (ns) pulses that may be obtained from such as system. Such narrow pulses could be used to measure distances in an object to obtain 3-D transmission measurements without motion.

While there are many touted benefits to static CT, there still exists no methodology of implementing yet. A source with the right performance, reliability, cost and form-factor does not yet exist. This work is a first-step in this direction by demonstrating that a source with the right performance and reliability metrics can be practically attained using field emission. The source design in this work has the potential to solve the cost and manufacturing problems because it uses conventional Si manufacturing and only requires a cathode or the Si FEA chip, a vacuum package and an anode. What still needs to be solved is that the source needs to be fabricated with the correct form factor and specifications for an application. This source was demonstrated in an actively-pumped small vacuum chamber much like all other field emission sources, but this form factor is still much too large for use in a practical system. Future engineering efforts will be needed to make the source with a specific form-factor such as the roughly 3 sources per degree necessary for conventional CT and vacuum packaging will need to be optimized for these considerations.

Conclusions

We have developed a novel x-ray source with a unique, and simple architecture consisting of only a cold-cathode Si field emission electron source, a vacuum enclosure, and an anode. We demonstrate that the x-ray source is robust enough and fulfills the resolution requirements for the majority of standard x-ray imaging tasks such as 2D and tomographic imaging. The source in development will be used as a distributed x-ray source that will enable new architectures for static 3D x-ray imaging. The demonstration showed in this paper is a first step to the practical implementation of such a source with additional engineering needed to fabricate a source with the proper form-factor.

Chapter 3

X-ray image acquisition

3.1 Using Document Scanners to Make Digital X-ray Images

In this section I discuss a technique for using a conventional document scanner to make an ultra low-cost x-ray imager. Despite its low cost - $50 vs $10,000 for a conventional medical x-ray flat panel detector - the document scanner can outperform the conventional flat panel by some resolution metrics. However, this technique does have a very long image acquisition time.

Adapted from: **Using Document Scanners to Make Digital X-ray Images.** Kadambi, A*, Cramer, A*, Lanza, R, Raskar, R, and Gupta, R. OSA Computational Optical Sensing and Imaging, June 25, 2018. (* these authors contributed equally).

Introduction: Digital radiography has become the *de facto* standard for X-ray imaging in the developed world. Unfortunately, its advantages — which include ease of image acquisition, visualization, processing, archiving and potential for teleradiology — have not come to large parts of the developing world due to cost and complexity. The primary driver of cost and complexity in these systems is the digital X-ray detector. With that motivation, this paper takes the first steps to turn an ordinary document scanner into a digital X-ray detector.

Specifically, we use a Canon® LIDE 220 document scanner to make X-ray images of a cadaver hand and an X-ray resolution chart. The document scanner is ill-posed to handle low-photon regimes, as would occur when using a scintillation screen. Therefore, both structured and unstructured artifacts are observed in the captured images. These artifacts stem from sources including hardware noise, striped noise from the scanning process, dead pixels, and photon noise from the X-ray beam and scintillating screen. We model and mitigate noise using an approach inspired by variational methods [117, 42]. In doing so, our work represents a first attempt to study scanner-based X-ray imaging, which we believe offers two primary benefits:

- Frugal X-ray sensing: a document scanner is inexpensive.
- High-resolution imagery: document scanners have evolved to scan prints at 5 micron-resolution, or better.

Clarifying scope: This paper studies the potential of X-ray imaging via document scanners. This means that an off-the-shelf X-ray source must be used to test the feasibility of our detection scheme. Although much cheaper than the detector, X-ray sources and their innovation are outside the scope of this work. The use of a commercial source also limits the immediate, clinical viability of our current prototype. This is an engineering limitation. The X-ray source used to test feasibility is not optimized for the line-scan detector; it has a conic field-of-view which unnecessarily exposes anatomy outside the linescan sensing region. Pairing a low-cost linescan source with our X-ray detector will alleviate the dose issue and is likely to enable frugal, *in vivo* X-ray radiography.

Optical Configuration: This section describes the hardware modifications made to a Canon® LIDE 220 document scanner. A schematic of our imaging layout and a photograph of our prototype is shown in Figure 3-1. To enable sensitivity to X-ray radiation, a scintillation screen is placed in front of the scan head to convert X-rays to visible light. The specific scintillation screen we use is made of gadolinium oxysulfide ($Gd_2O_2S : Tb$, peak emission at 550 nm, peak excitation energy at 110 keV). To avoid optical cross-talk, the integrated scan lamp in the document scanner must be

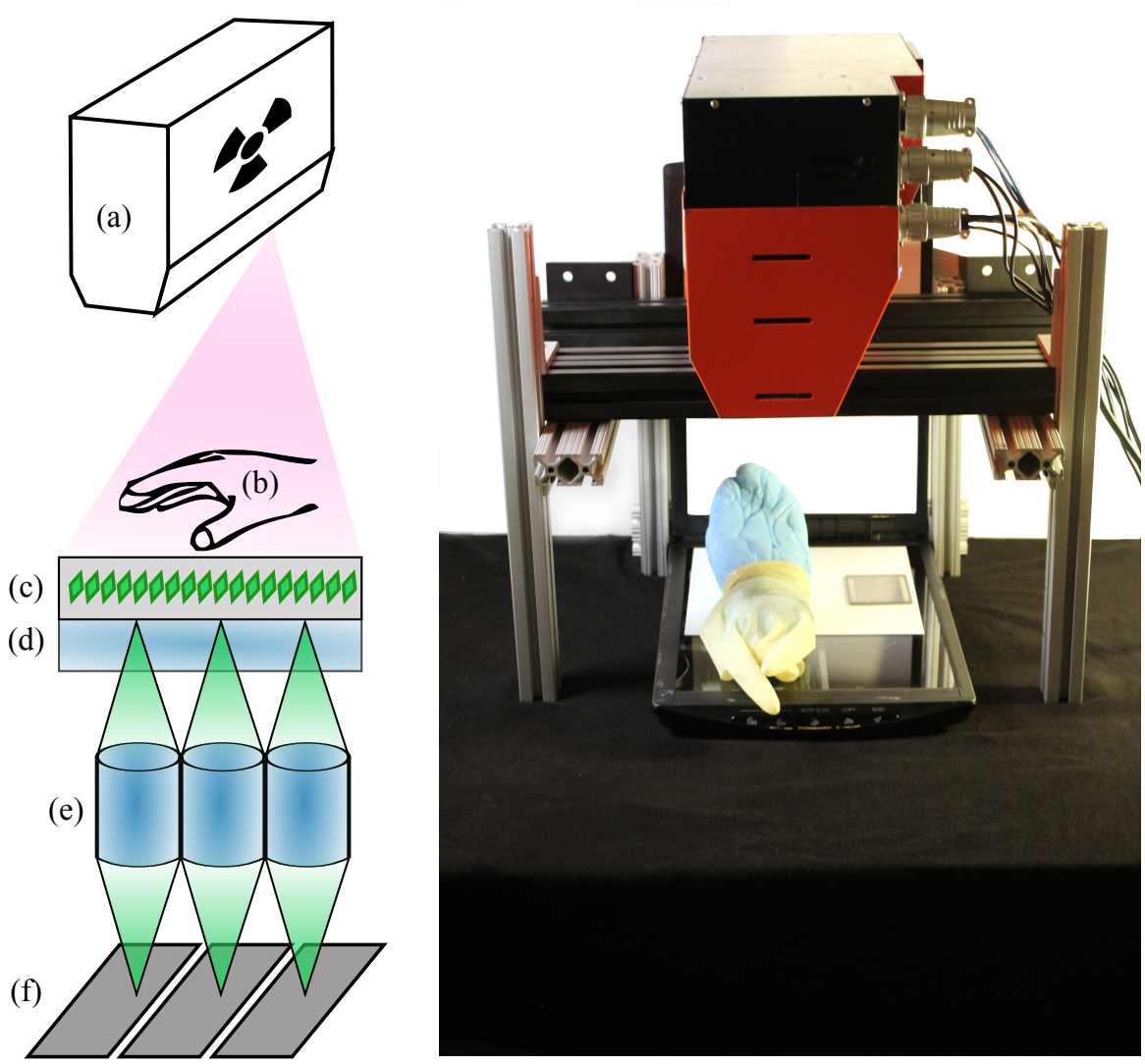

Figure 3-1: Using a document scanner as a digital X-ray detector. X-rays are emitted from the overhead-mounted source. The cadaver hand and a resolution chart lay on the scan bed. (a) X-ray cone beam; (b) object to be imaged; (c) scintillation screen emitting green light; (d) scanner glass (or optional lead-doped glass to block X-rays); (e) self-focusing gradient lens; (f) pixels on linescan sensor.

switched off during the exposure. We achieve programmable control of the scanner using Scanner Access Now Easy (SANE), an open-source Linux API. The object to be imaged is placed on the scintillator and irradiated with X-rays from a Hamamatsu X-ray source (model L9631).

Because the light emitted by the fluorescent screen in response to X-ray illumination is much dimmer than the light from the scan lamp of the scanner, it is necessary to either: (a) increase the exposure time; or (b) average multiple images. We write a Bash script to automate the scan process to acquire a set of batch images. We perform a naive average of these 100 images to obtain a single image, which we use as input to the post-capture denoising method described in the following section.

The complexity of X-ray detectors stems from the requirement for a large sensing area (e.g. 30cm x 40cm). Smaller CCD and CMOS sensors would lead to a significant loss in the field-of-view. It is interesting that a document scanner offers a large-format imaging surface that is as large as many clinically deployed X-ray detectors. Another benefit of using a scanner is the potential for high-resolution imaging. Over the past decade, the document scanner has evolved to the point where it is possible to scan photos and documents at 9600 dots-per-inch, which corresponds to a pixel pitch of about 2.5 microns. By contrast, clinical digital X-ray detectors such the Varian PaxScan 2530DX and Varian CB3040 have a pixel pitch between 100-200 microns. When scanning printed circuit boards or biological specimens with fine detail it might actually be preferable to use a document scanner. High-resolution is also desirable in many clinical applications such as mammography, where the pattern and morphology of microcalcifications is key in making accurate diagnosis.

In the context of frugal innovation, an oft-raised question is whether a digital camera could be used to take a picture of a scintillating screen. Unfortunately, the relatively small sensor size induces demagnification (e.g., a Canon® T3i DSLR has a sensor size of only 3 square centimeters). In scenarios where dose and resolution is not critical, hobbyists and researchers have proposed interesting approaches to capture X-ray images using camera sensors [51, 31].

Denoising Scheme: An output X-ray image from the scanner is shown in Figure 3-

2a. We first attempted to apply standard methods of denoising to eliminate the stripe pattern. In the radiology community, “air calibration" is a manual technique used to normalize each pixel in a line with the value of air. Unfortunately, this standard method did not work well for the heavily corrupted image from the document scanner. Therefore, we additionally incorporate more sophisticated techniques in a joint optimization. Our approach draws heavily from ideas used successfully in other research communities [117, 42, 13, 150, 154, 59, 2]. However, without a precedent for this hardware, we describe here an initial attempt to model and decouple X-ray linescan noise.

A document scanner comprises of a 1-D sensor of N pixels, which is moved to M positions. Let $\mathbf{y_m} \in \mathbb{R}^N$ denote the 1-D linescan from the m-th scan head position. The scanner concatenates multiple linescans together to transmit a 2-D image $\mathbf{Y} \in \mathbb{R}^{M \times N}$ to the computer, where $\mathbf{Y} = [\mathbf{y}_1, \ldots, \mathbf{y}_M]$. Since the scintillating screen emits dim light, the measurement $\mathbf{Y}$ results from either a long-exposure scan or an average of multiple scans. Let $\mathbf{X} \in \mathbb{R}^{M \times N}$ denote the ground truth image, which we aim to recover.

We assume an additive noise model, such that

$$\mathbf{Y} = \mathbf{X} + \mathbf{S} + \mathbf{G}, \tag{3.1}$$

where $\mathbf{S}$ is structured noise and $\mathbf{G}$ is zero-mean Gaussian noise. The structured noise primarily comprises of: (1) stripes due to the push-broom nature [45] of image acquisition and (3) dead lines.

We will be using the well-known metric of total-variation in our approach (first introduced by Rudin-Osher-Fatemi [117]). Let $\nabla_x \mathbf{S} \in \mathbb{R}^{M \times N}$ denote the horizontal discrete gradient. Then, the horizontal and vertical total variation of $\mathbf{S}$ is given by

$$\begin{aligned} \|\nabla_x \mathbf{S}\|_1 &= \sum_{m=1}^{M} \sum_{n=1}^{N-1} |S_{m,n} - S_{m,n+1}| \\ \|\nabla_y \mathbf{S}\|_1 &= \sum_{m=1}^{M-1} \sum_{n=1}^{N} |S_{m,n} - S_{m+1,n}|. \end{aligned} \tag{3.2}$$

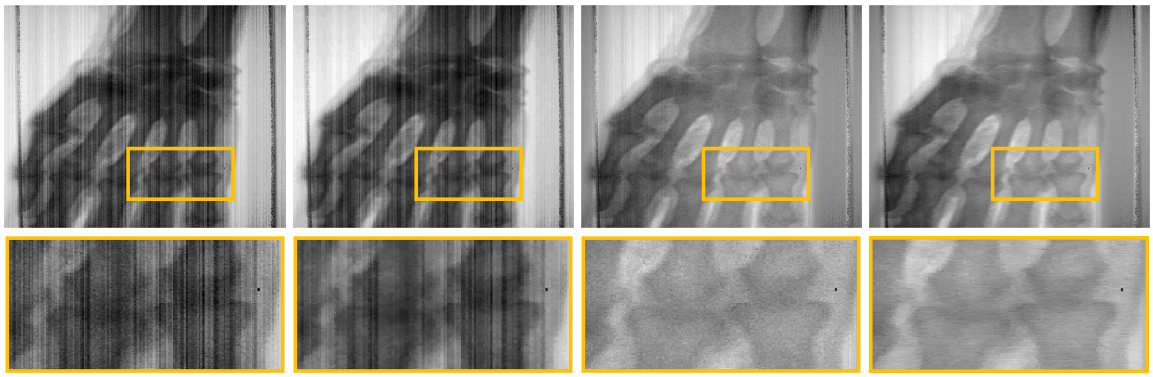

(a) Input: Data Avg from Scanner (b) Best TV denoising (c) Destriping Only (d) Joint Optimization [**Proposed**]

Figure 3-2: X-ray image of a cadaver hand using a Canon® LIDE 220 document scanner. (a) An averaged composite of 100 individual scans used as input to denoising methods (b-d). The proposed approach is (d). Inset image: proximal inter-phalangeal joint.

Since the stripes occur in the columns of the noisy measurement, it follows that

$$\|\nabla_x \mathbf{S}\|_1 \gg \|\nabla_y \mathbf{S}\|_1, \tag{3.3}$$

where $\|\cdot\|_1$ is the ℓ_1 norm. To account for unstructured noise (like photon noise from the X-ray beam) we will penalize the total-variation of $\mathbf{X}$. Taken together, a joint optimization is written as:

$$\underset{\mathbf{X},\mathbf{S}}{\operatorname{argmin}} \quad \mathcal{C}_{\mathbf{X},\mathbf{S}}(\mathbf{Y}) + \tau\|\nabla_y \mathbf{S}\|_1 + \lambda\|\nabla_x \mathbf{X}\|_1 + \lambda\|\nabla_y \mathbf{X}\|_1$$

where $\mathcal{C}_{\mathbf{X},\mathbf{S}}(\mathbf{Y}) = \|\mathbf{Y}-\mathbf{X}-\mathbf{S}\|_F^2$ denotes the convex functional for the fidelity term and $\|\cdot\|_F$ denotes the Frobenius norm. Despite the convexity of $\mathcal{C}_{\mathbf{X},\mathbf{S}}(\mathbf{Y})$, this objective function, unfortunately, does not admit closed-form differentiation due to the presence of regularizers. Therefore, the fidelity and regularization terms must be decoupled. The Split Bregman approach [42] is a fast numerical method suited for this task,

requiring that optimization program be rewritten as

$$\begin{aligned} \underset{\mathbf{X},\mathbf{S}}{\text{argmin}} \quad & \mathcal{C}_{\mathbf{X},\mathbf{S}}(\mathbf{Y}) + \tau\|\mathbf{A}\|_1 + \lambda\|\mathbf{B}\|_1 + \lambda\|\mathbf{C}\|_1 \\ \text{subject to} \quad & \mathbf{A} = \nabla_y \mathbf{S}, \\ & \mathbf{B} = \nabla_x \mathbf{X}, \\ & \mathbf{C} = \nabla_y \mathbf{X}, \end{aligned}$$

where the introduction of new variables $\mathbf{A}$, $\mathbf{B}$, and $\mathbf{C}$ serve to push the ℓ_1 terms for $\mathbf{S}$ and $\mathbf{X}$ into the constraints. Hereafter, we will focus our study on an unconstrained variant of the problem by writing the Lagrangian as:

$$\begin{aligned} &\underset{\mathbf{X},\mathbf{S},\mathbf{A},\mathbf{B},\mathbf{C}}{\text{argmin}}\ \mathcal{C}_{\mathbf{X},\mathbf{S}}(\mathbf{Y}) + \tau\|\mathbf{A}\|_1 + \lambda\|\mathbf{B}\|_1 + \lambda\|\mathbf{C}\|_1 \\ &+ \alpha\|\mathbf{A} - \nabla_y \mathbf{S}\|_F^2 + \beta\|\mathbf{B} - \nabla_x \mathbf{X}\|_F^2 + \beta\|\mathbf{C} - \nabla_y \mathbf{X}\|_F^2. \end{aligned}$$

A key to the Split Bregman method is to introduce so-called "Bregman variables" into the Lagrangian. Denote $\mathbf{A}'$, $\mathbf{B}'$, and $\mathbf{C}'$ as the Bregman variables, which are imputed into the optimization program as

$$\begin{aligned} &\underset{\mathbf{X},\mathbf{S},\mathbf{A},\mathbf{B},\mathbf{C}}{\text{argmin}}\ \mathcal{C}_{\mathbf{X},\mathbf{S}}(\mathbf{Y}) + \tau\|\mathbf{A}\|_1 + \lambda\|\mathbf{B}\|_1 + \lambda\|\mathbf{C}\|_1 \\ &+ \alpha\|\mathbf{A} - \nabla_y \mathbf{S} - \mathbf{A}'\|_F^2 + \beta\|\mathbf{B} - \nabla_x \mathbf{X} - \mathbf{B}'\|_F^2 \\ &+ \beta\|\mathbf{C} - \nabla_y \mathbf{X} - \mathbf{C}'\|_F^2. \end{aligned}$$

This optimization program is still not directly tractable. However, since the variables are decoupled, it is possible to subdivide the program into five smaller optimization programs that, individually, optimize one of the five decision variables. The subprob-

lems we consider are:

$$\begin{aligned}
\text{P1:} \quad & \underset{\mathbf{X}}{\operatorname{argmin}} \quad \mathcal{C}_{\mathbf{X},\mathbf{S}}(\mathbf{Y}) + \beta\|\mathbf{B} - \nabla_x\mathbf{X} - \mathbf{B}'\|_F^2 \\
& \qquad\qquad\qquad\qquad +\beta\|\mathbf{C} - \nabla_y\mathbf{X} - \mathbf{C}'\|_F^2 \\
\text{P2:} \quad & \underset{\mathbf{S}}{\operatorname{argmin}} \quad \mathcal{C}_{\mathbf{X},\mathbf{S}}(\mathbf{Y}) + \alpha\|\mathbf{A} - \nabla_y\mathbf{S} - \mathbf{A}'\|_F^2 \\
\text{P3:} \quad & \underset{\mathbf{A}}{\operatorname{argmin}} \quad \tau\|\mathbf{A}\|_1 + \alpha\|\mathbf{A} - \nabla_y\mathbf{S} - \mathbf{A}'\|_F^2 \\
\text{P4:} \quad & \underset{\mathbf{B}}{\operatorname{argmin}} \quad \lambda\|\mathbf{B}\|_1 + \beta\|\mathbf{B} - \nabla_x\mathbf{X} - \mathbf{B}'\|_F^2 \\
\text{P5:} \quad & \underset{\mathbf{C}}{\operatorname{argmin}} \quad \lambda\|\mathbf{C}\|_1 + \beta\|\mathbf{C} - \nabla_y\mathbf{X} - \mathbf{C}'\|_F^2
\end{aligned} \tag{3.4}$$

Although it may seem complicated to solve five optimization programs, each subproblem has a well-known solution. Problems P1 and P2 can be posed as a least-squares inversion, following the Kronecker product property described by the authors of [2]. We will use their solution in writing P1 as a matrix-vector equation:

$$\begin{aligned}
(\mathbf{I} + \beta[\nabla_x^T\nabla_x + \nabla_y^T\nabla_y])\mathbf{x} = (\mathbf{y} - \mathbf{s}) + \beta\nabla_x^T(\mathbf{b} - \mathbf{b}') \\
+ \beta\nabla_y^T(\mathbf{c} - \mathbf{c}'),
\end{aligned} \tag{3.5}$$

where $\mathbf{I}$ is the identity matrix and $\mathbf{x}$, $\mathbf{y}$, $\mathbf{s}$, $\mathbf{b}$, $\mathbf{b}'$, $\mathbf{c}$ and $\mathbf{c}'$ are vectors unrolled from matrices $\mathbf{X}, \mathbf{Y}, \mathbf{S}, \mathbf{B}, \mathbf{B}', \mathbf{C}$, and $\mathbf{C}'$, respectively. Turning now to P2, the solution is analogous, but simpler as the variation norm is only in one dimension, so that the linear system becomes

$$(\mathbf{I} + \alpha\nabla_y^T\nabla_y)\mathbf{x} = (\mathbf{y} - \mathbf{x}) + \alpha\nabla_x^T(\mathbf{a} - \mathbf{a}'), \tag{3.6}$$

where $\mathbf{a}$ and $\mathbf{a}'$ are unrolled from $\mathbf{A}$ and $\mathbf{A}'$. We refer the readers to [2] for the intermediate steps for Equations 3.5 and 3.6. P3, P4, and P5 have an extremely simple formulation, namely an ℓ_1 minimization with a Frobenius constraint. It is well-known that problems of these class can be solved via shrinkage operators. The

functional for shrinkage is

$$\mathcal{S}(\mathbf{P}, \nu) = \frac{\mathbf{P}}{|\mathbf{P}|} \max(|\mathbf{P}| - \nu), \tag{3.7}$$

for some matrix $\mathbf{P}$ and constant ν [42]. Finally, the Bregman variables, $\mathbf{A}'$, $\mathbf{B}'$, and $\mathbf{C}'$ need to be updated, which can be done with direct computation. Taken together, the update rules are

$$\begin{aligned}
\mathbf{A}_{k+1} &= \mathcal{S}(\nabla_y \mathbf{S}_k - \mathbf{A}'_k, \tau/\alpha) \\
\mathbf{B}_{k+1} &= \mathcal{S}(\nabla_x \mathbf{X}_k - \mathbf{B}'_k, \lambda/\beta) \\
\mathbf{C}_{k+1} &= \mathcal{S}(\nabla_y \mathbf{X}_k - \mathbf{C}'_k, \lambda/\beta) \\
\mathbf{X}_{k+1} &= \text{Least Squares Solution to Eq. 3.5} \\
\mathbf{S}_{k+1} &= \text{Least Squares Solution to Eq. 3.6} \\
\mathbf{A}'_{k+1} &= \mathbf{A}'_k + (-\mathbf{A}_{k+1} + \nabla_y \mathbf{S}_{k+1}) \\
\mathbf{B}'_{k+1} &= \mathbf{B}'_k + (-\mathbf{B}_{k+1} + \nabla_x \mathbf{X}_{k+1}) \\
\mathbf{C}'_{k+1} &= \mathbf{C}'_k + (-\mathbf{C}_{k+1} + \nabla_y \mathbf{X}_{k+1}),
\end{aligned} \tag{3.8}$$

where k denotes the iteration number from $1, \ldots, K$. The algorithm requires, as input, values for the regularization constants, τ, λ. Unknown variables are initialized to zero and the algorithm loops over the update rules until convergence. The final output is a denoised image, such that

$$\mathbf{X}_{\text{denoised}} = \mathbf{X}_{K+1}. \tag{3.9}$$

To our knowledge, we have proposed the first Split Bregman formulation that jointly enforces unidirectional total-variation on the noise matrix $\mathbf{S}$ while enforcing bidirectional total-variation on the image $\mathbf{X}$. Such a formulation turns out to be ideal for denoising X-ray scanned images. Our approach amalgamates ideas from prior, pioneering work: Rudin-Fatemi-Osher who formulate total-variation [117], Goldstein and Osher who proposed the Split Bregman method [42], Aggarwal and Majumdar [2]

who formulate an efficient method for hyperspectral denoising, and Bouali and Ladjal who first analyze unidirectional variation [13].

Results: A human cadaver hand was scanned using the modified Canon® LIDE 220, as per the optical description in Section **??**. 100 line scans were averaged to form the image in Figure 3-2a. Note the severe striped noise artifacts are unique to X-ray scanning. Subjective quality assessments for three denoising approaches are shown in Figures 3-2b-d. TV-denoising (implementation from [19]) is a common post-processing step in X-ray imaging, but is not designed for stripe artifacts. Implementing only the destriping method drastically improves the subjective image quality, but unstructured noise and a few speckle artifacts remain. The joint approach we propose mitigates mixed sources of noise artifacts and, by subjective assessment, seems well-matched to the X-ray linescan technique.

A resolution chart benchmark test was performed to compare the spatial resolvability of the modified Canon® LIDE 220 and a commercial-grade, flat panel detector from Varian Medical Instruments. Figure 3-3 plots the modulation transfer function of both systems. The MTF50 of both instruments is similar. While the commercial-grade detector performs well from 0.6 to 1.3 lp/mm, all contrast is lost at resolutions above 1.5 lp/mm. In comparison, the flatbed scanner performs slightly worse in the region from 0.6 to 1.3 lp/mm but retains 30 percent contrast out to 3.25 lp/mm, the highest-resolution feature on the test target. It is interesting that there is exists a regime where the scanner approach would prove advantageous with respect to accepted, commercial X-ray detectors.

This paper is a first attempt to experimentally demonstrate the potential of using consumer document scanners as a method to obtain X-ray images. Frugality aside, the potential for micron-resolution imaging could have broader implications in scanning detailed, *ex vivo* biomedical samples or for applications outside of medicine, such as material inspection. Further evaluations, on a larger dataset, are required to improve our understanding of the algorithm and the capture hardware.

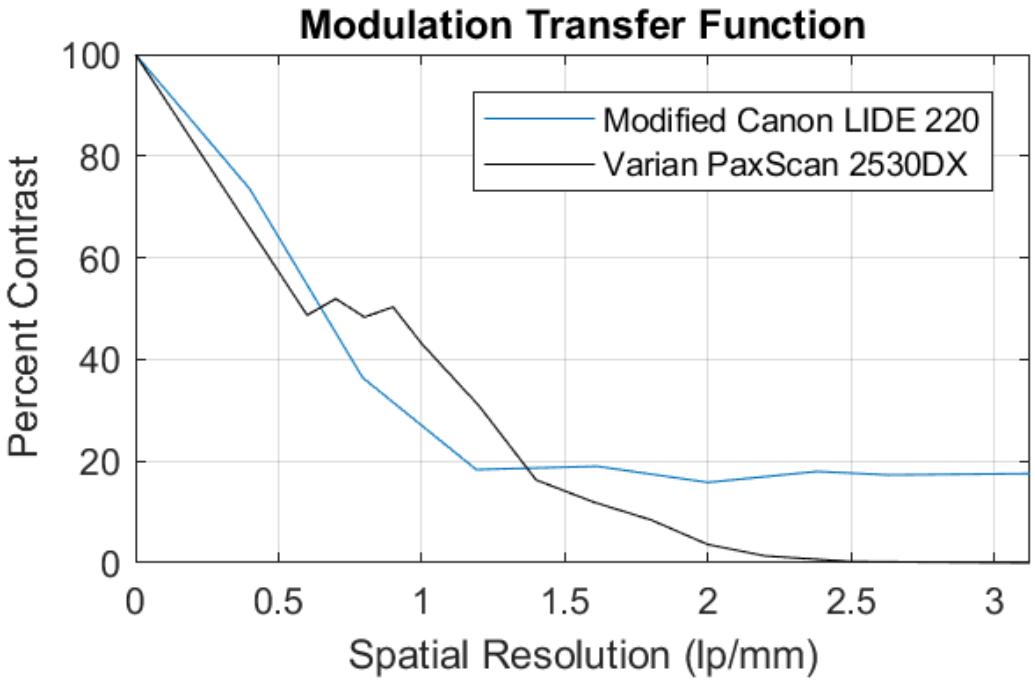

Figure 3-3: Modulation transfer functions for the modified X-ray scanner we constructed and a commercial flat panel X-ray detector.

3.2 Dynamic X-ray Elastography using a Pulsed Photocathode Source

In this section, I describe a technique for using a quickly pulsed x-ray source to extract both mechanical and radiolucency data from a vibrating sample. This method exploits the photocathode x-ray source described in the previous chapter, and could have relevance for many medical imaging techniques, but breast imaging in particular.

Adapted from: **Dynamic X-ray Elastography using a Pulsed Photocathode Source** Kamezawa C., Cramer A., Krull W., Yashiro W., Hyodo K., Gupta R [Submitted August 2020].

Introduction

Tissue elastography, a noninvasive imaging modality used to assess tissue stiffness, has been under development for the past three decades [98, 97, 72, 149, 90, 91]. Because cancerous lesions have different mechanical properties than adjacent healthy tissue, elastography aims to detect such lesions based on their stiffness. Even when

such lesions have similar x-ray attenuation to the surrounding tissue, and are therefore not apparent on conventional mammography, elastography may be able to detect them.

There are two main classes of elastography techniques: static, and dynamic. In static elastography, a fixed static pressure is applied to tissue under investigation and local strain from tissue deformation is mapped by imaging. This method can qualitatively evaluate the pattern of deformation and identify lesions [56, 138]. Static elastography, however, does not provide a quantitative map of tissue stiffness because it lacks a direct measure of the stress field within the tissue [142]. Dynamic elastography, the topic of this paper, uses shear wave propagation to map both stress and strain in the tissue in response to dynamic mechanical deformation, producing a quantitative elasticity map.

In dynamic elastography, shear waves are generated inside a sample by a superficially applied, time varying pressure. Such a pressure could be generated using air vibration, force impulse from acoustic radiation, or other methods that impart a shear wave which travels within the tissue. The time-varying stress and strain generated by this shear wave are continuously imaged. One generates a quantitative elasticity map by inferring the spatial and temporal variation in the tissue displacement from the velocity of the propagating shear wave from the observed image sequence. Depending on the sample of interest, a number of different medical imaging techniques may be employed to image the shear wave. Both magnetic resonance (MR) and ultrasound (US) elastography have rapidly expanded into clinical practice and have been used for liver and breast diseases, respectively [128, 63].

Despite higher spatial resolution and superior penetration depth of x-rays compared with other imaging modalities, relatively few studies have reported on dynamic x-ray elastography. In the past decade, static elastography using x-ray imaging has been reported by Hamilton et al, Kim et al, and Sutphin et al [66, 67, 1]. As mentioned before, these static techniques do not provide a quantitative elasticity map.

Dynamic x-ray elastography can provide a two-dimensional map of storage and loss moduli. This prior study used a continuous x-ray source that was divided into

individual pulses using an optical chopper wheel, an arrangement that was somewhat cumbersome to implement and difficult to accurately time. In this paper, we demonstrate the feasibility of dynamic x-ray elastography that obviates the need for a chopper wheel by synchronously pulsing the x-ray source.

Experimental Setup:

Figure 3-4 schematically illustrates the experimental setup for dynamic 2D x-ray elastography using a compact pulsed x-ray source. A photograph of the experimental setup is shown in Fig. 3-5. The pulsed x-ray source used in this research has been described previously [24]. The setup consists of an x-ray source, a gel phantom with a vibration stage, a detector for image acquisition, and a control unit. The continuously acquired 2D images of the phantom, under the influence of the vibration stage, are post-processed to compute the stiffness map. The individual components of our setup, and the processing steps for deriving the elasticity or stiffness maps, are described below.

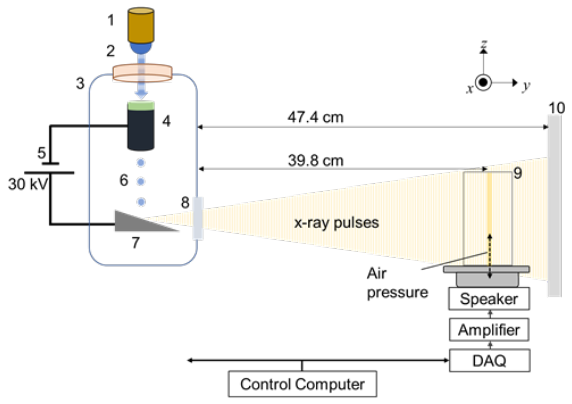

Figure 3-4: A pulsed 255nm UV LED (1) is used to illuminate a magnesium thin film through a quartz window (2). The thin film, shown in green color, is deposited on a glass electron multiplier (4). The photocathode and anode are both contained within a vacuum manifold (3) pumped down to 10-7 Torr by a turbo pump and sealed by a beryllium window (8). The output electrons of the photocathode (6) are accelerated through a high voltage supplied by (5) to a tungsten target anode (7), producing x-ray pulses through the Bremsstrahlung process. These pulses illuminate a phantom (9), depicted in detail in Fig 2. The phantom is vibrated pneumatically by a speaker synchronized with the UV LED. The images are acquired at different phases of the vibration by a flat-panel detector (10).

Pulsed X-ray Source:

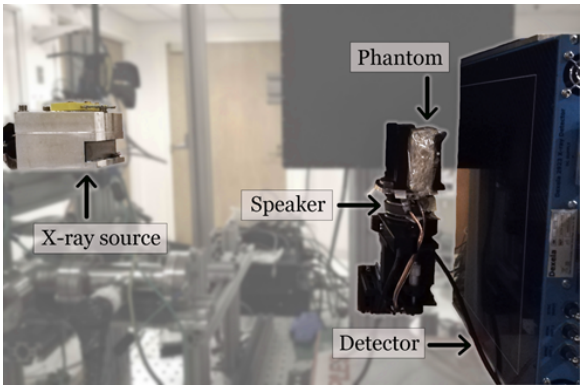

Figure 3-5: A photograph of the setup.

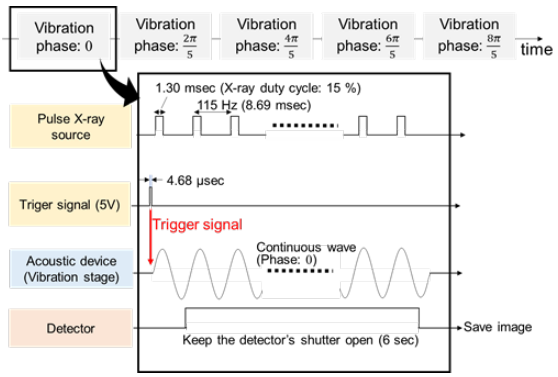

Figure 3-6: Image acquisition sequence for dynamic x-ray elastography using a pulsed x-ray source.

Our x-ray source, which is described in detail in Cramer et al [24] (see chapter 2.1), uses a pulsed ultraviolet (UV) LED emitting at 255 nm. The UV LED is placed outside the vacuum manifold of the x-ray source. The light from this LED strikes a photo-emissive magnesium film inside the vacuum manifold via a quartz window. A small number of photoelectrons generated in this matter are amplified by a Channeltron^{TM} (Photonis Inc., Sturbridge, MA) electron amplifier by a factor of up to 109. The output electron current from the Channeltron^{TM} is then accelerated through a high voltage to strike a tungsten target. The optical spot size of the resulting x-ray focal spot is 4.5 mm (horizontal) x 1 mm (vertical).

By adjusting the pulse duration, intensity and duty cycle of the UV LED, it is possible to control the x-ray pulses (and beam current) of the x-ray source. Seven such x-ray sources are housed in a single module and share a common vacuum manifold.

The overall 7-element source is designed to be small and lightweight (approximately 1 kilogram). The 7 sources span approximately 24 angular degrees.

In the current demonstration, we used a single x-ray source to generate a pulsed x-ray beam at 30 kVp and 20 μA tube current. The generated x-ray beam was incident upon a phantom mounted on a pneumatic vibration stage described below.

Gel Phantom and Shear Wave Generation:

We prepared Hitohada gel phantom (Fig. 3-7) from soft urethane resin doped with ZrO_2 particles. Our phantom had a 25 mm-diameter hard inclusion in the center. We used two types of raw materials of clear Hitohada gel to make the inclusion and the rest of the phantom: H05-100J (EXSEAL Co. Ltd.) was used for the hard inclusion; H00-100J (EXSEAL Co. Ltd.) was used for the surrounding matrix. These materials have a hardness of Asker-C 7 and Asker-C 0, respectively. The hard inclusion simulated a cancerous lesion with a different elasticity but similar radiolucency.

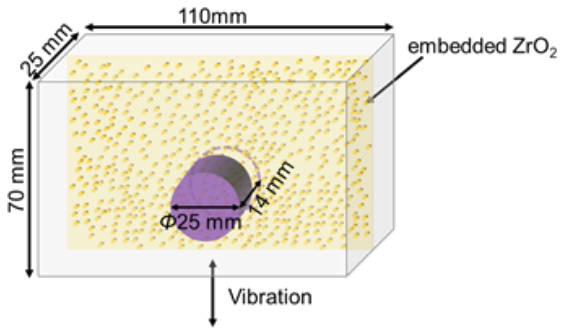

Figure 3-7: Hitohada gel embedded with ZrO_2 particles and a 25 mm diameter hard inclusion in the center.

We pneumatically vibrated the phantom using an 8 cm diameter Fostex M800 speaker with an added plastic cover with a 1 mm diameter hole. The sound from the speaker, which induced air pressure wave to vibrate the phantom, was generated by a sinusoidal signal from a data acquisition module or DAQ (National Instruments, USB-6002). The sinusoidal signal from DAQ was amplified using a power amplifier (Bose, Free Space IZA250-LZ) in order to drive the Fostex speaker. The speaker pneumatically vibrated the phantom in the z-direction at a frequency of 115 Hz in order to generate shear waves in the gel. With the speaker on, we acquired stro-

boscopic absorption images at each phase of the vibration to obtain a time-varying, two-dimensional view of the shear wave.

Synchronized Image acquisition:

The phantom was illuminated with pulsed x-rays synchronized to the DAQ and the speaker. X-ray images were acquired using a CMOS x-ray flat panel detector (Dexela 2923) that was located 47.4 cm from the x-ray source. The pixel size of the detector was 75 μm x 75 μm. The magnification of the phantom was 1.2 as shown in Fig. 3-5. Therefore, the effective pixel size at the isocenter of the phantom was 63 μm 63 μm. The duty cycle of the pulsed x-ray was 15%, with a pulse width of 1.3 msec as shown in Fig. 2. An x-ray projection image of the phantom was accumulated for 6 seconds, i.e., the electrical shutter of the detector was kept open for this duration. Therefore, the cumulative time for which the phantom was exposed by x-rays to obtain an x-ray projection image was 0.9 s. The sinusoidal signal from the DAQ was synchronized with x-ray pulses by a trigger from the pulsed x-ray start timing. We obtained x-ray projection images at five different phases of the air pressure vibration: 0, $\frac{2\pi}{5}$, $\frac{4\pi}{5}$, $\frac{6\pi}{5}$, and $\frac{8\pi}{5}$ (i.e., 0, 72, 144, 216, and 288 degrees, respectively) with respect to the vibration timing.

Image Processing and Elasticity Map Generation:

In order to obtain a two-dimensional elasticity map, we used a three-step process that is briefly summarized below [18]. First, we obtained the x-ray projection images at the 5 phases (0, $\frac{2\pi}{5}$, $\frac{4\pi}{5}$, $\frac{6\pi}{5}$, and $\frac{8\pi}{5}$) as shown in 3-6. The portion marked by the dotted circle is the hard inclusion embedded in the surrounding matrix.We then obtained displacement maps in the vertical direction (i.e., along the displacement vector of the shear wave) as shown in Fig. 3-8 (a-e) . We retrieved the displacement at each pixel in the maps by using a non-rigid registration algorithm — a non-parametric diffeomorphic image registration algorithm based on Thirion's demons algorithm [82] — implemented in MATLAB (Version 9.5.0, The MathWorks, Inc., Natick, MA, USA), and Butterworth bandpass filtering [21] for denoising. Our non-rigid registration algorithm, which non-linearly accounts for the local distortion field at each pixel, estimates a displacement field that aligns two images. In our case, the image

with 0 radian phase was used as the index image, and the distortion filed from it to the images with the phase timing of $\frac{2\pi}{5}$, $\frac{4\pi}{5}$, $\frac{6\pi}{5}$, and $\frac{8\pi}{5}$ were computed. We applied the fringe scanning method to this image set and mapped the displacement from the center of vibration amplitude for each pixel.

Finally, storage and loss modulus maps for the phantom were reconstructed on the basis of the incompressible algebraic inversion of the differential equation (AIDE) for an incompressible material ($\nabla \cdot u = 0$, where u is the displacement vector). In the AIDE, the complex shear modulus G is calculated from the wave equation in a stationary state (the Helmholtz equation) as follows:

$$G = -\rho\omega^2 \frac{U_i}{\nabla^2 U_i} \tag{3.10}$$

Here, ρ is density, ω is angular frequency of vibration, U_i is th discrete Fourier transform of u_i with respect to time, where u_i $(i = x, y, z)$ are components of $\mathbf{u}$. The complex shear modulus can be expressed by $G = G' + iG''$, where $G' \equiv Re(G')$ and $G'' \equiv Im(G)$ corresponding to the storage and loss moduli, respectively. As the Poisson's ratio of living tissue is between 0.490 and 0.499, we approximate both the phantom material and human tissue as incompressible. The volumetric mass density of Hitohada gel was determined to be 1.0 g/cm3. We excluded a small displacement area near the vibration stage. After that, we applied a median filter (25 pixels x 25 pixels) to the storage and loss modulus maps to make it smooth.

Results: Figure 3-8 (f) and (g) shows the maps of the storage and loss moduli obtained from Fig. 5 (a) through (e). As can be seen, the high storage modulus region corresponds to the region designed to simulate the cancerous lesion; this region has higher elasticity and is denoted by a dotted circle in Fig.5 (f). Therefore, out approach is able to distinguish the hard inclusion in a matrix. The storage moduli of the square regions in Fig.5 (f) denoted (f)-1 and (f)-2 were 12 ± 2.5 kPa and 3.4 ± 0.78 kPa, respectively. The loss moduli in the corresponding squares denoted by (g)-1 and (g)-2 in Fig.5 (g) were 4.4 ± 2.1 kPa and 2.8 ± 1.0 kPa, respectively.

We calculate of the contrast noise ratio (CNR) as follows:

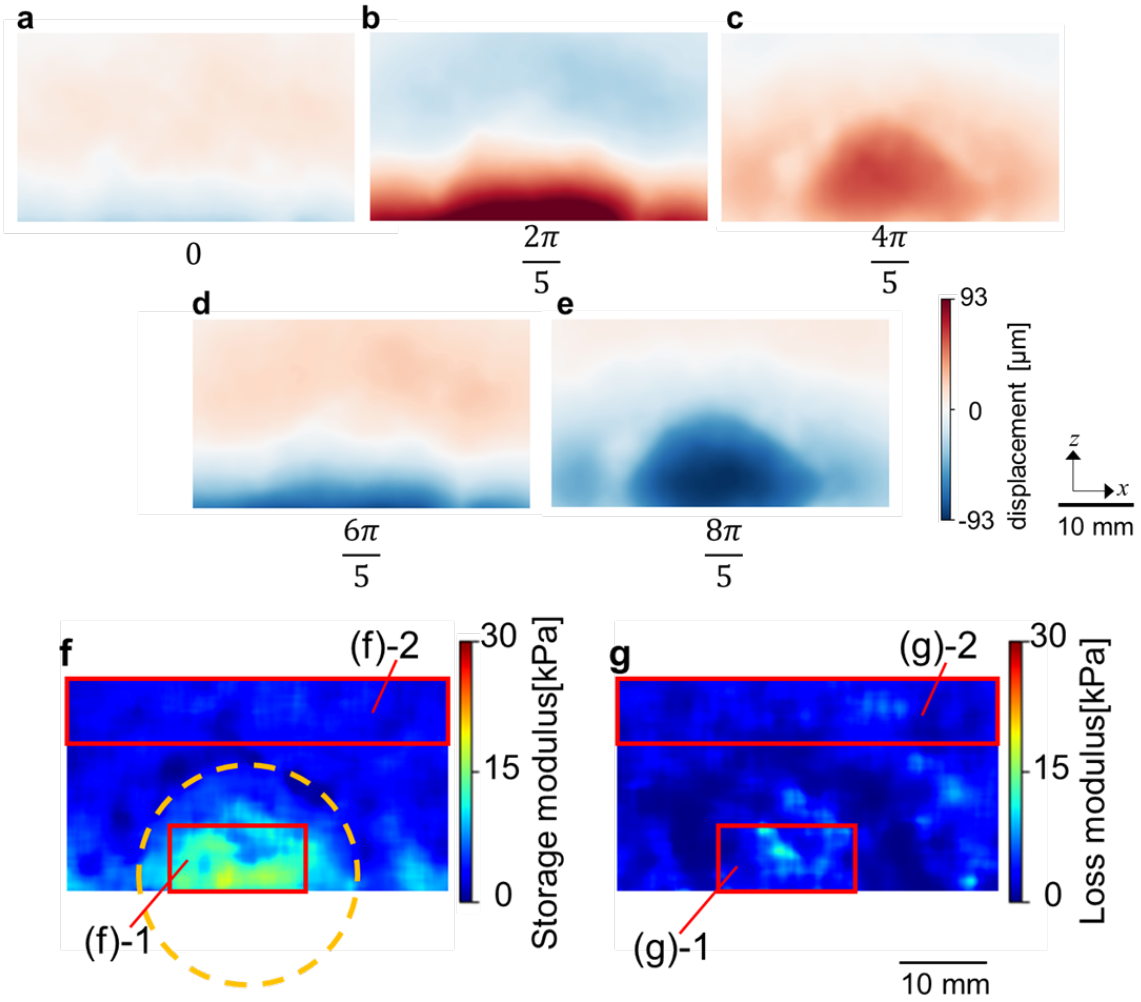

Figure 3-8: (a), (b), (c), (d), and (e) show the displacement maps with 0, 2/5 π, 4/5 π, 6/5 π, and 8/5 π radians of phases, respectively. (f) and (g): Maps of storage and loss moduli, respectively

$$CNR = \sqrt{\frac{2(\overline{S} - \overline{B})^2}{{\sigma_s}^2 + {\sigma_b}^2}} \tag{3.11}$$

Here, $\overline{S}$ and $\overline{B}$ are the mean of the signal and background,σ_s and σ_b are the standard deviation of the signal and background. The CNR in the storage modulus from (f)-1 to (f)-2 was 4.5. On the other hand, the CNR in the transmission image from the same ROI of (f)-1 to (f)-2 was 1.1. As such, the elastography outperforms naïve x-ray transmission imaging in its ability to discriminate a hard inclusion from surrounding material.

Discussion:

We demonstrated two-dimensional dynamic x-ray elastography by applying pneumatic vibration to a Hitohada gel phantom. Maps of storage and loss moduli were computed from the wave equation of the shear waves as they propagated through the phantom. The deformations imparted by the shear wave were imaged with a net exposure time of 4.5 s and an effective pixel size of 62 μm. The storage modulus map, obtained from dynamic elastography, was able to distinguish a hard inclusion inside a matrix with a CNR of 4.5. This is substantially better than the 1.1 CNR between these regions in the pure x-ray absorption images. The overall setup, using a pulsed x-ray source, was markedly more compact as compared to our previous setup that used a continuous x-ray with a chopper wheel.

The present paper focused on 2D elasticity maps. Because we used projection x-ray images of the breast phantom, any depth information along the direction of the x-ray projection is lost. Therefore, the elasticity maps are an aggregate, representing the whole thickness of the phantom. For many applications in medical diagnostics, including breast imaging, it is important to retain the depth information. In breast imaging, this is accomplished using tomosynthesis, an imaging technique in which a volumetric image is obtained from a series of projection images acquired along an angular span. Digital tomosynthesis has rapidly expanded in clinical practice and is the preferred method for evaluation of the breast. The experimental setup and the image processing methods presented in this paper have the potential to realize x-ray elastography and tomosynthesis in a volumetric fashion.

Tomosynthesis with the source module used in this study is feasible by virtue of the fact that the x-ray source has 7 x-ray elements spanning 24 degrees. Therefore, using 3 such sources side-by-side, one can create a 21-element arc of sources spanning approximately 72 degrees. These sources can be electronically steered, and such an assembly can be used for x-ray tomosynthesis without any moving parts. With the help of a vibration stage, it is possible to obtain the projection images over 4 or 5 different phases of shear wave propagation through the tissue. These projection images can then be converted into multiphase tomosynthesis slices, which can then

be used to produce slice-by-slice elasticity maps. All imaging for yielding slice-by-slice elasticity maps can be acquired without any moving parts in the setup and without rotating or displacing the sample.

The mean glandular dose (MGD) of full-field Digital Mammography (FFDM) and Digital Breast Tomosynthesis (DBT) for are approximately 1.4 mGy and 1.9 mGy, respectively, for the craniocaudal views as well as the mediolateral oblique views [26]. For x-ray elastography, one can divide this dose budget into lower dose projections that are timed and synchronized with the acoustic vibration according to the schedule described in this paper. As a result, the acquisition of the additional stiffness properties of the breast can essentially be dose neutral both in the FFDM and DBT setups.

Another possible application of this technique is compact x-ray elastography of small animals for basic medical science. This small and cost-effective x-ray elastography method would yield higher spatial resolution, deeper tissue penetration, and lower costs.

Acknowledgments: The authors thank Tomokazu Numano at Tokyo Metropolitan University and Yoshihiko Kawabata at Takashima Seisakusyo Co., Ltd for providing the software for vibration control. The authors also thank to Mitsuji Kamezawa for giving us the opportunity to use the vibration speaker.

3.3 Statistical Photon Arrival X-ray Imaging (SPARX): A Proposed Method for Low-Dose X-ray imaging

In this section I describe a proposed method for extending time-of-arrival optical imaging techniques into the x-ray domain. This could allow for exceptionally low-dose x-ray imaging, which would have patient safety benefits.

Developed jointly with Dr. Achuta Kadambi

Introducing SPARX

The SPARX imager is a novel type of X-ray imaging device that uses a probabilistic model of photon arrival times to obtain measurements of an object's attenuation. SPARX stands for **S**tatistics of **P**hoton **AR**rival **X**-ray. The potential benefit of SPARX is the ability to make images at dim illumination levels. In the context of X-rays, this would reduce the radiation dose to the patient.

Today, X-ray imaging follows the traditional model of Beer's law, expressed as

$$I = I_0 \exp(-\mu L), \tag{3.12}$$

where I is the irradiance on an image sensor, I_0 is the irradiance on the attenuating object, μ is the linear attenuation coefficient of the object, and L is the propagation distance through the object. Since I, I_0 and L are known or can be estimated, it is possible to solve Beer's equation for μ. In practice, a detector element collects charge generated by photons.[1]

In contrast, SPARX relies on fundamentally different data. Rather than measuring only the total number of photons (as in conventional X-ray), the SPARX method uses both timestamp and intensity data, requiring a specialized measurement system.

SPARX imaging hardware The imaging setup is shown in Figure 3-9. In the noiseless case, a temporal pulse $p(t)$ is transmitted into the sample and a photon receiver samples $\alpha p\left(t-\tau\right)$, a delayed and shifted version.

Related work This report repurposes classical statistical frameworks in information theory for the new goal of low-dose X-ray imaging. In particular, the point processes are taken from "Communication under the Poisson Regime" by Bar-David in 1969 [5], which is used to design maximum likelihood receivers. Much of this work is inspired by exciting, recent work in LIDAR imaging. Very specifically, this draft benefits from the dataset and statistical techniques from [127], clustering ideas introduced in [113] and temporal scatter analysis from [60].

[1]The number of photons incident on an X-ray sensor is not a standardized as it varies with factors that include the pixel pitch, exposure area, tube voltage, effective dose and tissue type. Assuming a chest radiograph with effective dose of 20 uSv, pixel pitch of 140 um, exposure area of 1500 cm^2, tube voltage of 90 kVp, the number of photons incident per pixel ranges from 10^3 to 10^4.

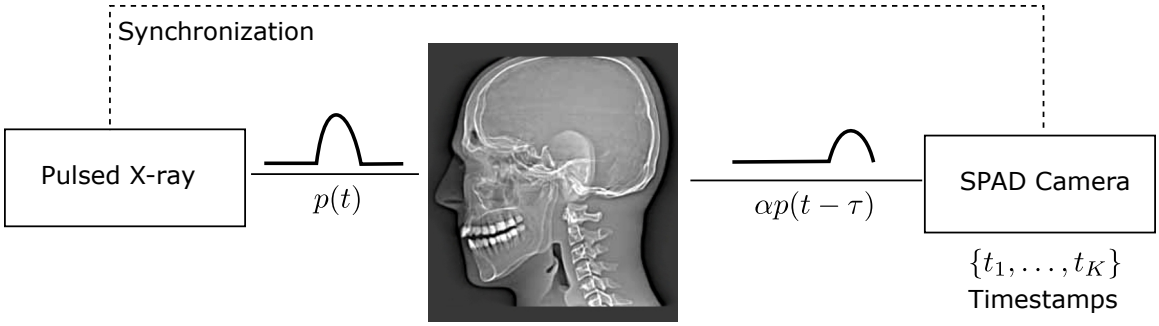

Figure 3-9: An experimental schematic of the setup. A pulsed X-ray source and SPAD camera are critical. To image the entire FoV of the object, the apparatus would need to be translated (not shown)

Statistical Framework

At a single scene point (x, y), in the absence of scattering, the rate at which photons arrive at the sensor can be expressed as a time-varying process:

$$\lambda_{x,y}(t) = \alpha_{x,y} p(t - \tau_{x,y}) + d,$$

where $\alpha_{x,y}$ is the attenuation of the pulse stream and d is the signal-independent dark rate. The goal is to estimate $\alpha_{x,y}$ at each scene point. To account for scattering, the rate function is modulated by a spatio-temporal blur, such that:

$$\begin{aligned}\lambda(t) = {} & \alpha_{x,y} p(t - \tau_{x,y}) + \\ & \iiint_{x',y',t'} \alpha_{x+x',y+y'} p(t + t' - \tau_{x+x',y+y'}) \, b_{x+x',y+y'}(t) \, (1 - \delta(x', y')) + d\end{aligned} \tag{3.13}$$

To simplify notation, let us write the above equation as:

$$\lambda_{x,y}(t) = \alpha_{x,y} p(t - \tau_{x,y}) + s_{x,y}(t) + d,$$

which uses the substitution $s_{x,y}(t)$ for the scattering integral. For now, it is assumed that $s_{x,y}(t)$ is independent of $\alpha_{x,y}$ (due to the Dirac within the integral). The framework of radiative transfer could be used to model the scattering process [20].

Using Poisson point process statistics, we can write the probability of detecting k

photons within a time window ranging from time $t = a$ to $t = b$ as

$$P[k, (a, b)] = \exp\left(-\int_a^b \lambda(t)\right)\left[\int_a^b \lambda(t)\right]^k /k!,$$

In principle, the imaging data at each pixel is a sequence of timestamps from the SPAD camera $\{t_1, \ldots, t_K\}_{x,y}$. The probability of detecting these timestamps is related to the rate function by

$$p\left[\{t_1, \ldots, t_K\}_{x,y}\right] = \exp\left(-\int_t \lambda_{x,y}(t)\right)\prod_1^K \lambda_{x,y}(t_k).$$

This can be written as a maximum likelihood problem:

$$\ell\left[\{t_1, \ldots, t_K\}_{x,y}; \alpha_{x,y}, \tau_{x,y}\right] = -\int_t \lambda_{x,y}(t) + \sum_1^K \log\left(\lambda_{x,y}(t_k)\right).$$

The derivative is written as

$$\frac{\partial \ell}{\partial \alpha_{x,y}} = -\int_t p(t - \tau_{x,y}) + \sum_1^K \frac{p(t - \tau_{x,y})}{\alpha_{x,y} p(t - \tau_{x,y}) + s_{x,y}(t) + b}.$$

The maximum likelihood estimate for α is then:

$$\widehat{\alpha} = \arg\min_\alpha -\int_t p(t - \tau_{x,y}) + \sum_1^K \frac{p(t - \tau_{x,y})}{\alpha_{x,y} p(t - \tau_{x,y}) + s_{x,y}(t) + b}.$$

As noted in previous work [127, 113], calculation of the maximum likelihood estimate for α is facilitated if the model omits noise (e.g., from dark counts or scattering). Hence, if $s_{x,y}(t) = b = 0$, the equation above can be rearranged as

$$\widehat{\alpha} = \frac{K}{\int_t p(t - \tau_{x,y})}.$$

This expression is intuitive, as the estimate for α is a ratio between the total number of photon events that the detector senses, and the energy of the incident radiation. This estimate produces good results in LIDAR, as first shown in [127]. Unfortu-

nately, omitting dark counts and scattering is practical for reflective LIDAR, but not for X-ray propagation through biological tissue. **Mixture Model** Conceptually, a maximum likelihood model suggests that the attenuation coefficient is proportionate to the signal counts that the detector senses. We will use parametric statistics to estimate which distribution each photon came from before performing the maximum likelihood estimate. This is closely related to prior work from [113], except that we are not trying to separate homogeneous and inhomogeneous Poisson processes. To simplify derivation, let us assume that the X-ray pulse is a Gaussian, such that the distribution of counts from the illumination source can be written as

$$f_{x,y}^{p}\left(t\right) \propto \left(\frac{K}{\int_{t} p\left(t-\tau_{x,y}\right)}\right) \exp\left(-\frac{\left(t-\tau_{x,y}\right)^{2}}{2\sigma_{p}^{2}}\right),$$

where σ_p corresponds to the temporal duration of the illumination. Proportionality is used to account for normalization. Here, the maximum likelihood estimate for the pulse attenuation scales our distribution. For simplicity - *later, we must precisely characterize the scattering distribution in X-ray, at the wavelengths, and tissue type we operate on* - let us assume the scattering distribution can also be expressed as a Gaussian:

$$f_{x,y}^{s}\left(t\right) \propto \exp\left(-\frac{\left(t-\tau_{x,y}-t_{s}\right)^{2}}{2\sigma_{s}^{2}}\right).$$

For a given count at $t = t_k$, we classify which distribution it most likely came from (e.g. scattering or signal). Then, we add up the photons that come from the signal distribution.

Regularization Separating signal counts from scattered or dark counts will help improve the contrast and resolution of the attenuation image, but the image will still by noisy. Specifically, Poisson noise will still limit the quality of reconstructions. This is a fundamental property of the quantum nature of light, so any approaches to mitigate shot noise will rely on aggregating signal. Since it is not feasible to increase the radiation exposure, an image processing approach like total variation or non-local means will be used for denoising.

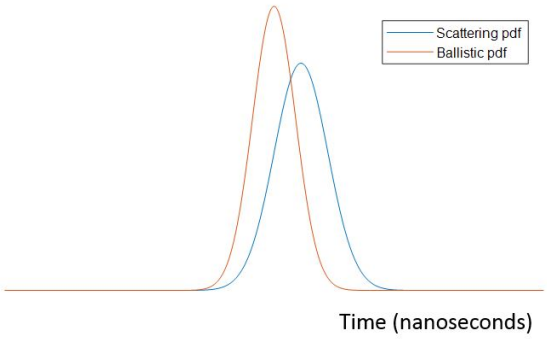

Figure 3-10: A photon is probabilistically identified as a scattered or ballistic photon based on a mixture model of distributions. The distribution will depend on the hardware configuration, X-ray energy level, and the type of tissue being imaged.

Maximum Likelihood Receiver On real data, it may be advantageous to characterize whether a small cluster of detections arises from signal or noise. We can split the rate equation into the sum of two inhomogeneous processes and a homogeneous process, such that:

$$\lambda(t) = \lambda_{x,y}^{\text{pulse}}(t) + \lambda_{x,y}^{\text{scatter}}(t) + \lambda^{\text{dark}}, \tag{3.14}$$

where each individual process is

$$\begin{aligned} \lambda_{x,y}^{\text{pulse}}(t) &= \alpha_{x,y} p(t - \tau_{x,y}) \\ \lambda_{x,y}^{\text{scatter}}(t) &= s_{x,y}(t) \\ \lambda^{\text{dark}} &= d \end{aligned} \tag{3.15}$$

Prior work has addressed the separation of $\lambda_{x,y}^{\text{pulse}}$ and λ^{dark} by exploiting the fact that the former is inhomogeneous and the other is not. Here, we will consider the distinction of the two inhomogeneous processes using a point process likelihood ratio:

$$\begin{aligned} \ell &= \exp\left(\int \lambda_{x,y}^{\text{scatter}}(t) - \int \lambda_{x,y}^{\text{scatter}}(t)\right) \prod_{1}^{K} \frac{\lambda_{x,y}^{\text{scatter}}(t)}{\lambda_{x,y}^{\text{pulse}}(t)} \\ &= \exp\left(-\int_{t} s_{x,y}(t) - \alpha_{x,y} p(t - \tau_{x,y})\right) \prod_{1}^{K} \frac{s_{x,y}(t)}{\alpha_{x,y} p(t - \tau_{x,y})} \end{aligned} \tag{3.16}$$

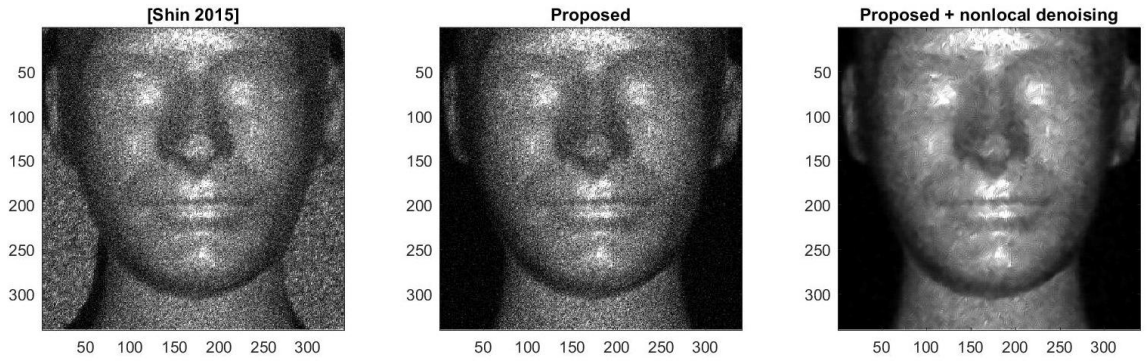

Figure 3-11: In the noiseless case, the proposed results are similar to the state-of-the-art [127].

Here, if the scatter kernel is known, and estimates of depth and transmission (e.g. using maximum likelihood) are known, then a cluster of K photon detections can be identified as belonging to the scatter or pulse process.

Simulated Comparisons

Experimental data: The experimental data was obtained from the authors of [127]. The dataset does not appear to include ground truth reflectivity measurements. Over the full-field, this dataset collects $K = 8.26$ timestamps per pixel with negligible dark counts (hence, 8 photons are collected per pixel). To date, this is the state-of-the-art paper for low-flux imaging measurements using LIDAR.

Noiseless case: In the absence of noise, the proposed technique demonstrates similar results to the state of the art (because there is no background noise). This is good - because the state-of-the-art by [127] is considered the lowest flux method in the LIDAR community.

Scattering: Three scattering levels were tested, at 10 dB, 20dB, and 30 dB of scattering. Because the dataset does not have ground truth it is difficult to get an error metric; however, it is clear that the proposed method has slightly more contrast.

Comparing SPARX with a Conventional Chest X-ray

We continue by describing how the experimental measurements on a LIDAR

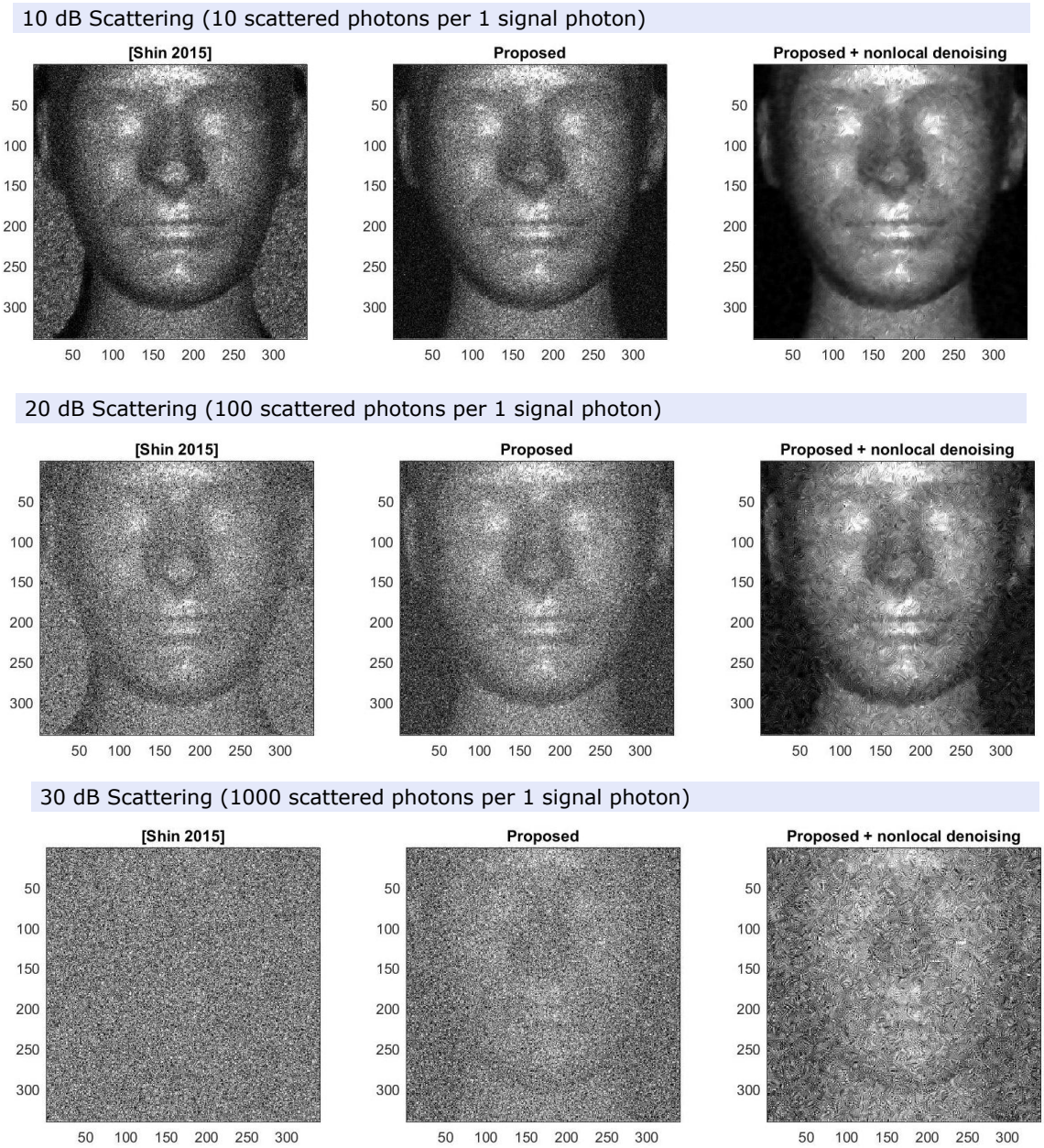

Figure 3-12: Performance at 10 dB, 20 dB, and 30 dB of scattering.

dataset offer support for radiation dose savings in a clinical X-ray context. The previous section used, on average, 8 photons per-pixel to obtain the results in Figure 3-12. Figure 3-14 shows a clinical scan of a projection chest X-ray, using on average thousands of photons-per-pixel in a 20 μSv chest exposure. At first glance, it is not immediately obvious how much dose is saved since forming images at 8 photons-per-pixel data on LIDAR data is a very different procedure from a 20 μSv chest X-ray. A few differences include:

1. Optical capture—the LIDAR data uses completely different hardware to acquire timestamp data in visible light and in reflection mode. In comparison, the projection X-ray was acquired in transmission mode. The sensing schemes are radically different.

2. Quality—on an image-to-image comparison, the reconstructed LIDAR image has a different noise level than the medical scan.

3. Dynamic Range and Contrast—on an image-to-image comparison, the reconstructed LIDAR image has a different amount of contrast.

In order to reasonably compare the two schemes, we aim for an accurate image-to-image comparison. Hence, distinctions in optical capture are not considered. Therefore, the comparison relies on: (1) choosing a metric for image "quality"; (2) finding "equivalent" regions in the two images; and (3) extrapolating dose assuming a Poisson noise model. Figure 3-13 summarizes the approach.

Quality Metric

In the medical imaging community, the metric of contrast-to-noise ratio is used, defined as

$$\mathrm{CNR} = \frac{(S_{\mathcal{A}} - S_{\mathcal{B}})}{\sigma}, \tag{3.17}$$

where $S_{\mathcal{A}}$ and $S_{\mathcal{B}}$ represent the quantized image values in two regions-of-interest, denoted as $\mathcal{A}$ and $\mathcal{B}$. In principle, $\mathcal{A}$ is considered the signal region of interest and $\mathcal{B}$ the background. The denominator of Equation 3.17, σ, represents the standard

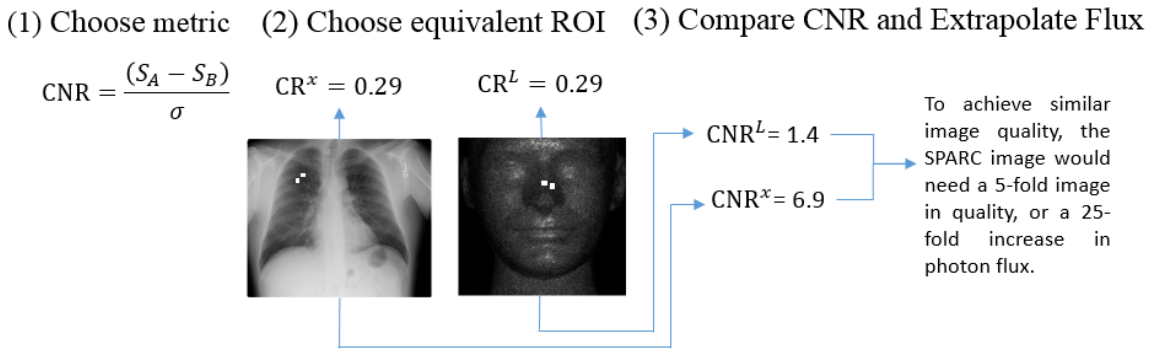

Figure 3-13: Methods used to extrapolate LIDAR flux to X-ray flux. First, the quality metric of contrast-to-noise (CNR) ratio is chosen. Second, pairs of comparable regions are identified in each of the X-ray and LIDAR images, selected for their contrast ratio being equal. These regions are shown in the white squares overlaid on the images. In computing CNR on these regions, it is observed that the quality of the LIDAR data has one-fifth the CNR of a medical-grade scan. Under a Poisson noise model, a 25-fold increase in the LIDAR exposure would achieve equivalent CNR between the two images.

deviation of image noise, once defined [52] over an ROI basis as

$$\sigma = \frac{1}{2\sqrt{\sigma_{\mathcal{A}}^2 + \sigma_{\mathcal{B}}^2}}. \tag{3.18}$$

In such manner, the image noise can be quantified over both regions-of-interest. In the radiology community, it is well-known that even within a single medical image, choosing different ROIs to define $\mathcal{A}$ and $\mathcal{B}$ will lead to a different contrast-to-noise ratio, which we consider in the next subsection.

Finding Equivalent ROIs

In order to find equivalent regions in the LIDAR data and the X-ray data, we impose the constraint that the CNR is computed over ROIs of comparable contrast. More precisely, one can quantify contrast as a ratio, expressed as

$$CR = \frac{(S_{\mathcal{A}} - S_{\mathcal{B}})}{S_{\mathcal{B}}}, \tag{3.19}$$

where CR denotes contrast-ratio. Let us now consider two pairs of ROIs. One pair exists in the space of LIDAR data, defined as $\mathcal{A}^L$ and $\mathcal{B}^L$. Another pair exists in the

space of X-ray data, written as $\mathcal{A}^X$ and $\mathcal{B}^X$. Now, contrast ratios can be calculated separately as

$$\begin{aligned} CR^L &= \frac{(S_{\mathcal{A}^L} - S_{\mathcal{B}^L})}{S_{\mathcal{B}^L}} \\ CR^X &= \frac{(S_{\mathcal{A}^X} - S_{\mathcal{B}^X})}{S_{\mathcal{B}^X}}. \end{aligned} \tag{3.20}$$

The regions of interest commonly used to define contrast in chest x-rays are the upper lung and adjacent rib shadow, shown in Figure 3-14. With such a definition, examination of six de-identified digital chest radiographs yielded a contrast ratio of $CR^X \approx 0.30 \pm 0.02$. Now, in the lidar image data, a search was performed over different regions of interest until a pair, $\mathcal{A}^L$ and $\mathcal{B}^L$, was found that yielded a $CR^L \approx CR^X$. Critically, the pair $\mathcal{A}^L$ and $\mathcal{B}^L$ must also correspond to a meaningful variation in the image (e.g. the bridge of the nose versus the shadow cast by the nose, shown in Figure 3-15). Equipped with a pair of corresponding regions, it becomes possible to compare image quality.

Flux Extrapolation

To estimate dose, the quality of the equivalent regions in the LIDAR and X-ray datasets are compared using CNR, where

$$\begin{aligned} CNR^L &= \frac{(S_{\mathcal{A}^L} - S_{\mathcal{B}^L})}{\sigma^L} \\ CNR^X &= \frac{(S_{\mathcal{A}^X} - S_{\mathcal{B}^X})}{\sigma^X}. \end{aligned} \tag{3.21}$$

After obtaining the ROI pair (as described in the previous subsection), it was found that $CNR^X \approx 6.97 \pm 1.43$ and $CNR^L \approx 1.4$. No standard deviation is provided for the LIDAR dataset, since only one such dataset was used in this paper. Not surprisingly, with an average of only 8 photons detected per pixel, the LIDAR dataset is of poorer quality than the X-ray data. However, the image noise would decrease with increasing flux levels or averaged exposures. If a Poisson model of image noise is assumed to occur in the LIDAR data, then increasing the number of detections by a factor of N would increase CNR^L by a factor of $\sqrt{N}$. Define N^* as the scaling factor at which

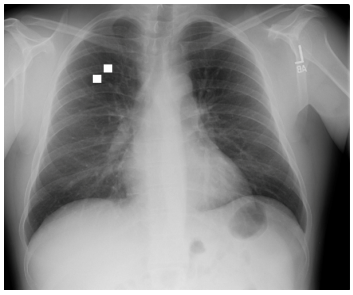

Figure 3-14: Clinical lung x-ray with ROI between upper lung and adjacent rib shadow. A dataset of six such, deidentified images were obtained from the Massachusetts General Hospital.

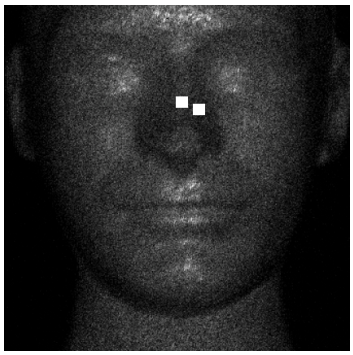

Figure 3-15: LIDAR image with ROI marked. The contrast between teh two squares in this image correspond to the contrast between the two squares in Figure 3-14. The LIDAR data is provided by Shin et al [127].

$CNR^L = CNR^X$. Then,

$$N^* = \left(\frac{CNR^X}{CNR^L}\right)^2. \tag{3.22}$$

For the datasets shown in Figure 3-13, the value of $N* \approx 25$. Therefore, the LIDAR data needs about 25 times the amount of light in order to achieve a similar quality as the chest radiograph. A LIDAR dataset would have to have about 200 photons/pixel to meet this quality requirement. We define this as the *effective photon fluence*.

Estimating SPARX Dose

We estimate here the dose from SPARX imaging. This is done by converting the effective photon fluence (from the previous section) to effective dose, in Sieverts.

Photon Fluence, Exposure, and Effective Dose

From the CNR analysis, we have an estimate for the number of photons per pixel in SPARX imaging; we now need to determine the corresponding effective dose delivered

to the patient. Photon fluence is defined as

$$\Phi = \frac{dN}{da} \tag{3.23}$$

Radiation exposure, the amount of ionization induced in air by x-rays, is commonly measured in Roentgen, a non-SI unit equivalent to $2.58 * 10^{-4}$ C/kg. We can convert from photon fluence to exposure using the formula:

$$\frac{\Phi}{X} = \frac{0.00873}{h\nu(\frac{\mu_{ab}}{\rho})} \frac{\text{J}}{\text{kg R}} \tag{3.24}$$

At 30 keV, a common photon energy level for chest radiography, the conversion factor is (Sprawls, 1995)

$$\Phi = 1.55 * 10^{10} \frac{\text{photons}}{\text{cm}^2 \text{ R}} \tag{3.25}$$

To go from exposure to absorbed dose in tissue, we use the conversion factor of 0.0096 Gray per roentgen. A further factor, the radiation weighting factor, would be used to account for the varying biological effects of different types of ionizing radiation; however, for x-ray photons, the radiation weighting factor w_R is 1.

We can calculate the dose-area product by multiplying absorbed dose by the irradiated area.

Finally, we need to convert from dose-area product to effective dose. Under the paradigm from [53], the conversion coefficient a chest radiography acquisition in an adult with a 20 cm chest, at 90 kVp, filtered with a 2 mm aluminum filter. will be 0.24mSv/Gy cm^2.

At at a tube voltage of 90 kVp, the average photon energy will be approximately 30 keV. At this energy and chest depth, the x-ray transmission through the chest will be about 10% [73]. Thus, for each photon that reaches the detector, an average of 10 photons will have been absorbed by the patient.

Dose calculation in SPARX imaging

With a SPARX imaging acquisition using 200 photons per pixel, and assuming a pixel pitch of 140 μm, and a 14"x17" detector size, we can calculate the effective dose

Table 3.1: SPARX is estimated to reduce the radiation dose by an order of magnitude.

Procedure	Effective Dose (μSv)
Simultaneous PET/CT	25,000
Chest CT	7000
Conventional Chest X-ray	**20**
Average Daily Background	10
SPARX Chest X-ray	**2.2**
Eating a 150 g banana	0.1

E as:

$$E = \frac{200 \text{ photons}}{\text{pixel}} \frac{1 \text{ pixel}}{140^2 \mu\text{m}^2} \frac{\text{cm}^2 \text{ R}}{1.55 * 10^{10} \text{ photons}} \frac{0.0096\text{Gy}}{\text{R}} \frac{0.24\text{mSv}}{\text{Gy cm}^2} 1535\text{cm}^2 \frac{1}{.1} \quad (3.26)$$

$$E = 2.23\mu\text{Sv} \quad (3.27)$$

By contrast, a typical dose for a conventional chest x-ray is 20 μSv.

Radiation risk in context

Under the assumptions detailed above, it is estimated that the SPARX chest X-ray would reduce the dose of a conventional chest X-ray by about an order of magnitude. A comparison of effective dose from various radiation sources, including SPARX, can be found in Table 3.1.

Medical imaging needs to take into account patient safety. In one of the most widely-adopted models for cancer risk from radiation, the linear-no-threshold model, a linear relationship is assumed between increased cancer risk and organ dose. The LNT model is supported by epidemiological data from survivors of the atomic bombings of Hiroshima and Nagasaki, as well as by subsequent epidemiological studies of cancer risk and medical imaging. Evidence for linearity in cancer risk has been shown down to 20mSv [74, 75]. Under this model, it is estimated that 0.5-2 percent of all US cancers are caused by radiation from computed tomography alone [15], although that figure has been debated.

Conclusion and Future Work

There are several immediate avenues for progress, both experimental and theoretical, that could advance SPARX as imaging technique. One step would be to develop a parametric model of scattering and pulse attenuation that takes into account the X-ray transmission and scattering. The applicability of SPARX imaging to CT could also be modeled, in order to quantify the dose reduction in tomographic imaging.

Experimentally, SPARX imaging could be conducted using a Single-Photon Avalanche Diode (SPAD) camera or Time Correlated Single Photon Counter (TSCPC) in conjunction with a fast scintillator or direct-detection film to measure timestamped photon arrivals. In the simulation, the LIDAR pulse was 270 picoseconds long, so an x-ray source capable of picosecond pulsewidths - perhaps driven by an optical clock - would also be important. A phantom consisting of a contrast pattern with 16 x-ray absorption "gray" levels would also be necessary to demonstrate the bit depth of SPARX imaging.

An extremely low-flux radiography system would allow for long-term or repeated imaging without fear of harming patients. While a ten-fold reduction in dose from a conventional projection x-ray is certainly appealing, a similar dose reduction in computed tomography would be revolutionary. Utilizing photon-arrival statistics, such as in the framework described here, could provide a way to achieve that dose reduction.

Chapter 4

Tomographic Image Reconstruction Techniques

4.1 Signal Sensing and Reconstruction Paradigms for a Novel Multi-source Static Computed Tomography System

We have demonstrated a new framework for tomographic imaging. We have completed a portable tomosynthesis module capable of extremity and specimen imaging. Our future work will focus on customizing what we have for specific medical applications.

An important aspect of the CT imaging chain (especially with x-ray sources that can vary their output) is the illumination pattern.

For a CT system comprised of discrete sources, there are two broad approaches to achieving sufficiently high x-ray dose rate at each projection- overlapping the exposure from multiple sources, or creating more powerful sources that may require more space, reducing the the number of projections.

In the first part of this chapter, we explore simulations for the first paradigm: increasing the effective dose by illuminating a given detector with multiple sources simultaneously. The results were not encouraging, as the increase in noise (even

without scatter considerations) outweighed the benefit in signal-to-noise ratio from the higher effective dose.

Adapted from: **Signal Sensing and Reconstruction Paradigms for a Novel Multi-source Static Computed Tomography System**, Kowtal, Cramer, et al. IEEE-IASSSP

Introduction

X-ray computed tomography (CT) can provide life-saving diagnostic information such as the detection of strokes, internal bleeds, and cancers in minutes. Traditional CT scanners employ a single powerful X-ray source and an arc of detectors mounted on a rotating gantry. The gantry rotates around a patient to acquire projection images that are transferred over a slip ring to a computer. Specialized reconstruction algorithms running on this computer invert the projection data to compute tomographic slices through an object or a patient. This architecture requires a powerful X-ray source, consuming as much as 250 kW of peak power, in order to obtain projections with high signal to noise ratio.

CT systems must be built with exceptional precision and rigidity to operate stably at the extreme rotation rates (up to 300 rpm) required for imaging. Particularly for full-body CT, such operational requirements invariably lead to heavy, difficult to service, non-portable machines which need to be operated in a controlled hospital-style environment. Careful balancing and calibration are required periodically as these systems remain susceptible to variability in environmental conditions and vibrations. Therefore, current CT systems are generally unsuitable for operation outside of well-controlled hospital environments.

One way to overcome these limitations is to replace the powerful, heavy, rotating source with multiple, weaker, static sources in a circle as shown in Fig. 4-1. Instead of mechanically rotating the sources, one can electronically pulse individual sources to acquire projections from multiple angles. We have designed such an architecture and demonstrated its feasibility [25, 111, 46]. We used an array of novel, miniaturized photocathode-based x-ray sources and an energy-integrating flat panel detector. Other attempts at building static computed tomography machines include electron-

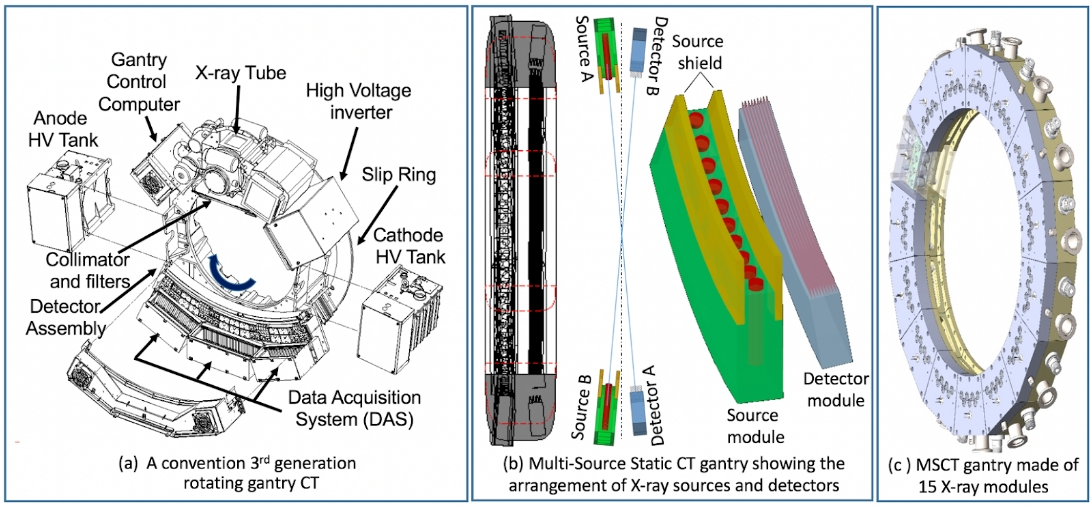

Figure 4-1: A typical CT system versus the proposed system

beam tomography, in which beam of accelerated electrons is steered along a circular tungsten anode around the patient [86]; and arrays of field emission sources[27], such as carbon nanotubes [151, 102].

Any tomographic imaging system with multiple X-ray sources offers the possibility for new acquisition schemes, since a single detector can be illuminated by X-rays emitted from more than one source simultaneously.

Measurement model

In traditional CT, the measurement a sensor j captures due to the source with power P is:

$$y_j = \mathcal{P}[Pe^{-\alpha_{S\to j}}] \tag{4.1}$$

where $\mathcal{P}[\beta]$ represents a Poisson random variable with parameter β. The 'attenuation coefficients', α_j, through the factor $e^{-\alpha_j}$, measure the fraction of light left after traversing the straight-line path from the source to detector j. At every point in the imaged object, the local attenuation coefficient is a function of the local electron density and atomic number. Inferring these attenuation coefficients, therefore, gives us information about the composition of the object. The total attenuation along the straight-line path from the source to detector j, $\alpha_{S\to j}$, is an integral of the attenuation

coefficients along it: $\alpha_j = \int_{p \in \mathcal{S} \to j} \alpha(p)$. The Poisson statistics of the measurement arise from the randomness in the source emitting photons and the detector counting them.

In this new sensing strategy, since we can turn multiple sources on at the same time, we have more flexibility in choosing which sources to turn on at each measurement step. In this case, in its full generality, the measurement model can be written as:

$$y_j^{(k)} = \mathcal{P}\left[\sum_{i=1}^{n} w_i^{(k)} P e^{-\alpha_{i \to j}}\right] \tag{4.2}$$

The measurement steps, indexed by k, are akin to one rotation in traditional CT. At measurement step k, the source i is turned on at a fraction $w_i^{(k)}$ of its full power. This model degenerates to traditional CT if only one of the sources is on at every measurement step.

The absorption coefficients $\alpha_{i \to j}$ represent, as before, the fraction of light left after light traverses the straight-line path from source i to detector j: $\alpha_{i \to j} = \int_{i \to j} \alpha$. This measurement model can be restricted to on/off sources by setting $w_j \in \{0, 1\}$.

The traditional CT problem can be solved by converting measurements into the 'projection space':

$$\log \frac{y_j}{P} = -\alpha_j \tag{4.3}$$

The path integral α_j is estimated by dividing the imaged object in voxels. In that case, α_j is a sum of attenuation coefficients over the imaged object, and the equations above represent a linear system in the attenuation coefficients of the object. This can be solved using techniques such as SART or filtered backprojection [3]. The new CT problem requires an additional step to disambiguate the contributions of different sources to each measurement.

$$\log \frac{y_j}{P} = -\sum_i w_i \sigma_{i \to j} \tag{4.4}$$

where $\sigma_{i\to j} = e^{-\alpha_{i\to j}}$. This linear system in $\sigma_{i\to j}$ can be solved to yield the values of $\alpha_{i\to j}$, which can be used to infer the object in the same way as traditional CT. This solution can be refined by solving the following regularized (here, total variation denoising) Poisson log-likelihood problem:

$$\min_{\alpha} \sum_{k,j} -\log \mathcal{P}_{\sum_{i=1}^{n} w_i^{(k)} P e^{-\alpha_{i\to j}}} \left(y_j^{(k)} \right) + TV(\alpha) \tag{4.5}$$

where $\mathcal{P}_\beta(.)$ is the Poisson probability mass function with parameter β. Signal-independent sensor noise can be tackled using the Gaussian approximation to a Poisson distribution:

$$\begin{aligned} \min_{\alpha} \sum_{k,j} -\log \mathcal{G} \Bigg(& y_j^{(k)}; \sum_{i=1}^{n} w_i^{(k)} P e^{-\alpha_{i\to j}}, \\ & \sum_{i=1}^{n} w_i^{(k)} P e^{-\alpha_{i\to j}} + \sigma^2 \Bigg) + TV(\alpha) \end{aligned} \tag{4.6}$$

where σ^2 is the variance of the sensor noise and $\mathcal{G}(.; \mu, \sigma^2)$ is the Gaussian probability density function with mean μ and variance σ^2. Our implementation solves Eq. 4.6 with the sensor noise set to 0.

Apart from the ability to apply a coded pattern of illumination, the static CT geometry may also enable other advantages. As an example, a distributed array CT geometry also allows for more precise beam current modulation than a conventional CT architecture, since the photon flux along any given ray is determined and modulated by electronics, not the angular momentum of a heavy rotating gantry. This could allow for a reduction in radiation exposure to portions of the anatomy where we already have enough photons to estimate the linear attenuation coefficients.

Multiplexed Measurement

The multi-source, static CT architecture splits a single, powerful source into multiple weak sources. The image acquisition consists of turning on only a fraction of the weak sources. Therefore, each detector gets only a fraction of the flux it would have received from the single powerful source. If we were to distribute the powerful

source into K weak sources, the photon flux intercepted by each detector is K times lower. The value of K, to be able to approximate a traditional CT system, needs to be high enough to cover all the angles for which projections are needed. Therefore, light paths that pass through the center of the object, and are attenuated the most, are severely photon-deprived. These are also the projections that contain the most information about the object's composition.

Fig. 4-2 shows the extent of photon deprivation in a typical brain CT scan. The simulated system here has a diameter of 70 cm, 5000 detector pixels, and 500 weak sources, each emitting a monochromatic 60 keV X-ray beam (approximating a 120 kV tube voltage) with a flux of 1 kW in total integrated over 360 degree angle. Detector size is fixed at 100 μm. The minimum flux intercepted is an average of 2.5 photons per pixel per exposure. A traditional CT scanner taking 500 exposures in the same exposure time, on the other hand, would see around 1000 photons per pixel per exposure.

One of the degrees of freedom the static CT system offers us is the possibility of turning on multiple sources at the same time. This is a unique feature that a rotating gantry cannot achieve. The case for multiplexing the measurements can be motivated by considering the CT reconstruction problem from linear measurements that have signal-independent noise with in them. The problem can be stated as $y = Ax + \eta$, where we need to recover a vector x from noisy measurements y in the presence of signal-independent noise η. Such a formulation is known to yield better (inverse-based) reconstruction with certain multiplexed measurements than non-multiplexed ones [120]. However, if the measurements are Poisson, $y = \mathcal{P}[Ax]$, and reconstruction is performed using the matrix (pseudo) inverse $y = A^{\dagger}x$, the best A to use in terms of reconstruction error is one that measures x element-wise [120, 135]. There also exist empirical results [126] that show that if this reconstruction is performed by solving a Poisson likelihood problem, in the low-flux regime and with positivity constraints, multiplexed matrices can yield better reconstructions.

Therefore, it is unclear if a solution multiplexing Poisson acquisition and maximizing Poisson likelihood would yield better reconstruction than measuring with one

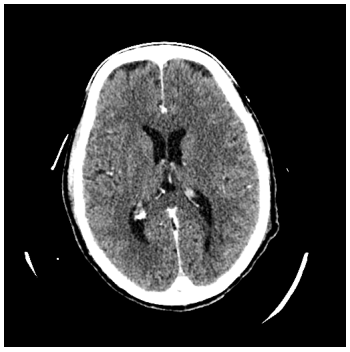

(a)

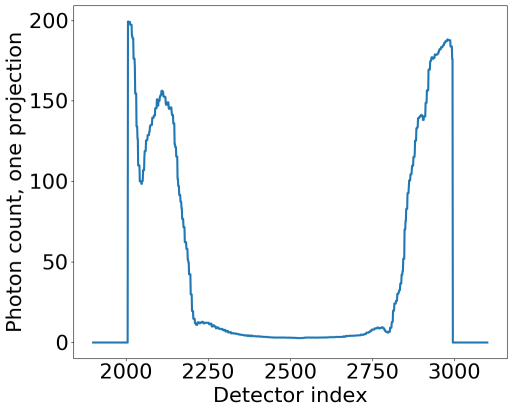

(b)

Figure 4-2: Photon deprivation with one source ON at a given time. (a) Imaged axial slice through a human brain, and a typical projection image with the X-ray source on top. (b) Photon rate seen in a noiseless measurement by a subset of detectors. The rate is smallest at a point opposite to the source because light traverses the most amount of tissue. Here, the minimum rate is ~ 2.5 photons per exposure.

source on at a time. However, our preliminary results seem to indicate that we cannot do better than the one-at-a-time exposure. In other words, multiplexing is not useful in terms of reconstruction image quality for fixed, non-adaptive imaging. The only solution that is better than one at a time is taking advantage of the limited fan angle of sources with a multi-leaf collimator. In such as setup, one can turn multiple sources on at the same time even thought only one source contributes to any single detector.

Results and Discussion

In this section we present preliminary results by simulating a traditional CT scanner and turning sources them on one at a time. In our simulations, we use a smaller version of the proposed design with only 100 sources and 1000 detectors. Each source

is set to emit at monochromatic 60 keV beam at 5 kW of power. The system has a diameter of 70 cm. The fan angle for each source is set to 36, which means 10 sources can be turned on at the same time without overlapping. Reconstruction is performed at a resolution of 128 $\times$ 128 pixels per slice. Fig. 4-3 shows the results of CT slice acquired at the level of foramen of Monro, a level that is dominated by brain parenchyma. Fig. 4-4 shows results for a slice at the skull base that is dominated by bony anatomy. Results from by a geometrically equivalent 200 kW CT scanner as also shown. Even though the image quality from the simulated traditional CT is less than ideal because of fewer number of projections, it is better than the low-power static CT image.

While static CT gives adequate image quality for high-contrast structures such as bone, it is inadequate for soft-tissue discrimination, required, for example, for distinguishing between gray and white matter of the brain.

Conclusion

In this paper we presented a new CT system architecture that lends itself to adaptive acquisition schemes. When the projection images are acquired one at at time, the image quality of the low power acquisitions from our proposed system does not match that of a traditional high-power CT scanner. Overlapping the image acquisition, e.g., by turning on multiple sources at the same time, also does not improve the image quality because of the additive nature of Poisson noise. Therefore research in adaptive schemes where each detector is illuminated by only one source at any given time is important. By engineering the system to allows an adaptive fan-angle for each X-ray source, and by installing a multi-leaf collimator, one can change sensing geometry that enables such acquisitions. Photon-counting detectors [145] in the reconstruction, as they provide an additional dimension of data, may also prove useful in improving reconstruction quality.

Improvements are also needed in the reconstruction algorithm to incorporate additional constraints and prior knowledge. Better data-driven priors could be constructed to regularize the inverse problem by countering the effect of relative increase in measurement noise. Incorporating the effect of x-ray photon scattering [39, 41] is also

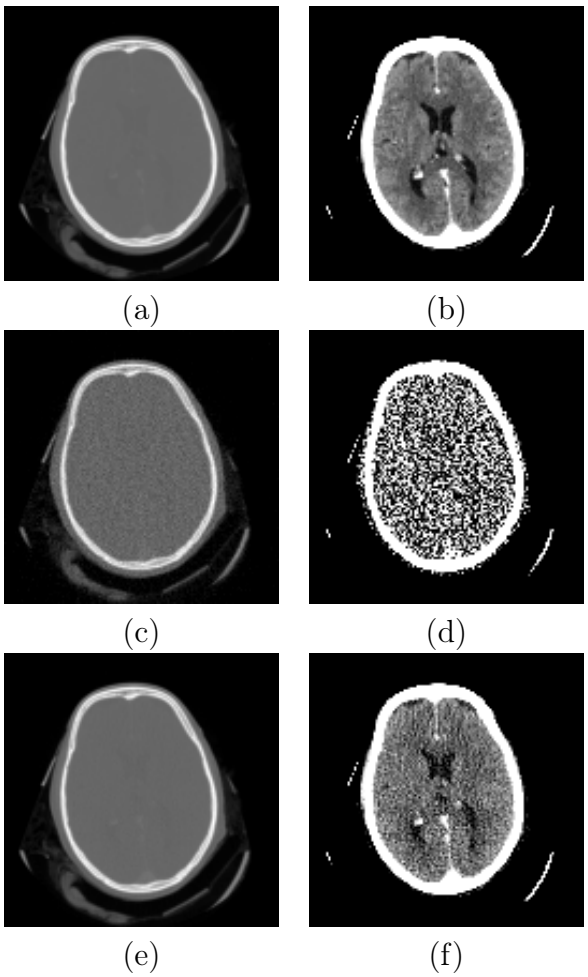

Figure 4-3: The ground truth CT slice (top row), a slice reconstructed from the simulated low-power static CT (middle row), and a slice reconstructed from a simulated, 200kW traditional CT scanner (bottom row). Both the bone (left) and brain (right) window levels are shown. For the simulated static CT system with parameters in Section **??**, the image quality metrics were RMSE = 6.36%, SSIM = 0.98 as compared with RMSE = 1.13% and SSIM = 0.999 for the high-power traditional CT.

very important for because geometries with multiple sources illuminating individual detectors preclude the use of an anti-scatter grid.

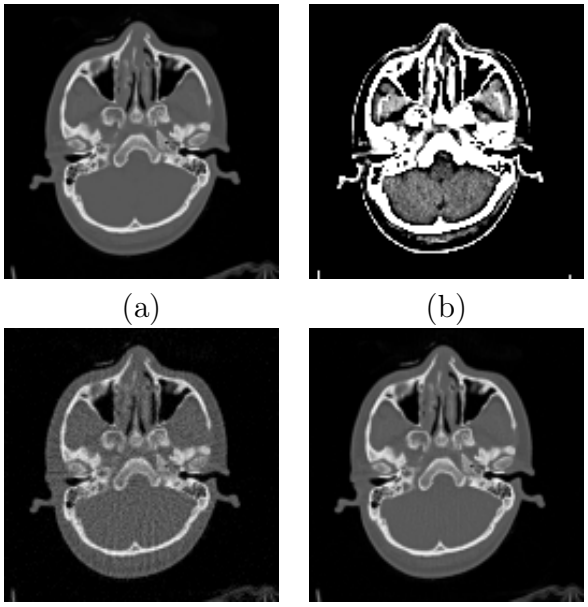

(a) (b)

(c) (d)

Figure 4-4: Ground truth slice in bone (a) and brain (b) window-level setting, slice reconstructed using the low-power static CT (c) results in RSME= 8.74% and SSIM = 0.976, and slice from a simulated high-power traditional CT (d) resultin in RSME = 1.83% and SSIM = 0.999.

4.2 AUTOMAP for CT: Reducing the Number of Projections in CT Imaging Using Domain-Transform Manifold Learning

In the second part of this chapter, we demonstrate a technique for noisy tomographic image reconstruction which, in conjunction with a discrete x-ray sources such as the ones described in Chapter 2, could advance the capabilities of non-rotating CT imaging. This technique relies on modern machine learning techniques and GPU hardware.

Adapted from: **AUTOMAP for CT: Reducing the Number of Projections in CT Imaging Using Domain-Transform Manifold Learning** Cramer et al, AAPM 2020.

Introduction Many non-rotating x-ray computed tomography (CT) frameworks are being developed, with discrete sources, including a system previously reported

by our group [24, 23, 155]. For these discrete-source systems, the number of x-ray sources is directly linked to the number of projection angles.

If a CT image could be reconstructed with fewer projections, it could mean not only less dose to the patient, but also ease the engineering constraints or a non-rotating CT system as each individual source can occupy a larger arc angle.

The heart of CT reconstruction is the solution to the inverse radon problem-phrased another way, determining the 2D image given a sinogram. From the Central Slice theorem, this inverse problem can be broken down into three distinct steps:

(1) a series of 1D discrete Fourier transforms (1DFT) of each row of the sinogram.

(2) a radial arrangement of the 1DFTs based on the angular separation of the individual projection images

(3) a 2D discrete Fourier transform into image space.

The CT image reconstruction problem shares many similarities with the 2D inverse discrete Fourier transform that is the basis of MRI image reconstruction. Machine learning techniques have improved the quality of reconstructed MRI images and in particular, and shown to have utility in undersampled reconstruction MR- the analogous problem to reconstructing a CT image from a limited number of projection angles.

One such algorithm, AUTOMAP, has had particular success in reconstructing undersampled and noisy MR images. However, AUTOMAP has two fully connected layers which severely constrain the GPU memory requirements. A possible solution to this issue was present in [122] by decomposing the fully connected layers, which reported not just lower memory useage but also better performance in certain MRI domains.

In general, various machine learning methods have been proposed and demonstrated for the solution to this inverse radon problem, as well as for the direct Fourier transform method necessary in MRI image reconstruction. These reconstruction algorithms can be grouped under a few broad categories:

Image-space to image-space transforms this category of algorithms first perform the deterministic algorithm (FBP or FFT for CT and MRI, respectively), and

then improve the resultant image space output by training on ground truth.

Projection-space to projection-space transforms in this category of algorithms, the raw sinograms/FFT data are improved, trained on a perfect forward model of the ground truth image. FBP/FFT is then applied to produce the image-space result.

End-to-end transforms including AUTOMAP and dAUTOMAP, end-to-end transformations take in projection space data and return image space data.

Methods

We adapted AUTOMAP (distributed AUTOmated transform by Manifold APproximation) for CT image reconstruction [155]. AUTOMAP is an end-to-end generalized reconstruction framework, implemented with a deep neural network architecture composed of two fully connected layers followed by a sparse convolutional autoencoder.

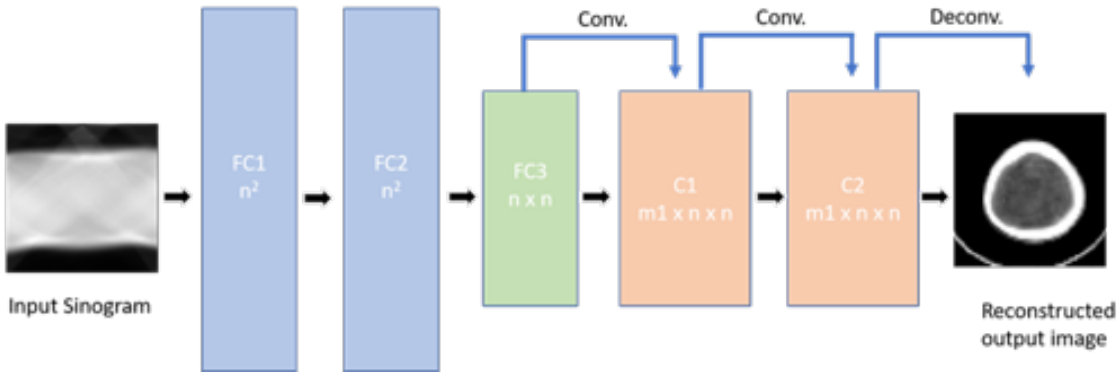

Figure 4-5: Layers of AUTOMAP, as used for CT

Because of the two fully-connected layers in AUTOMAP, the memory requirements of the algorithm increase dramatically as a function of image size. Furthermore, this memory requirement exists for each layer, so using multiple cores will not alone solve this problem- the size of each individual core is the limiting factor.

We explored three different hardware architectures that could solve this problem, detailed below:

-Using a 512 GB CPU, and accepting a roughly 5x computation time penalty

Breaking up individual matrix multiplications (block matrix decomposition), and

performing each sub-matrix multiplication on a separate GPU

Breaking up individual matrix multiplications (block matrix decomposition), and performing each sub-matrix multiplication on a single Large Model Support (LMS) 16 GB GPU optimized for fast loading and unloading

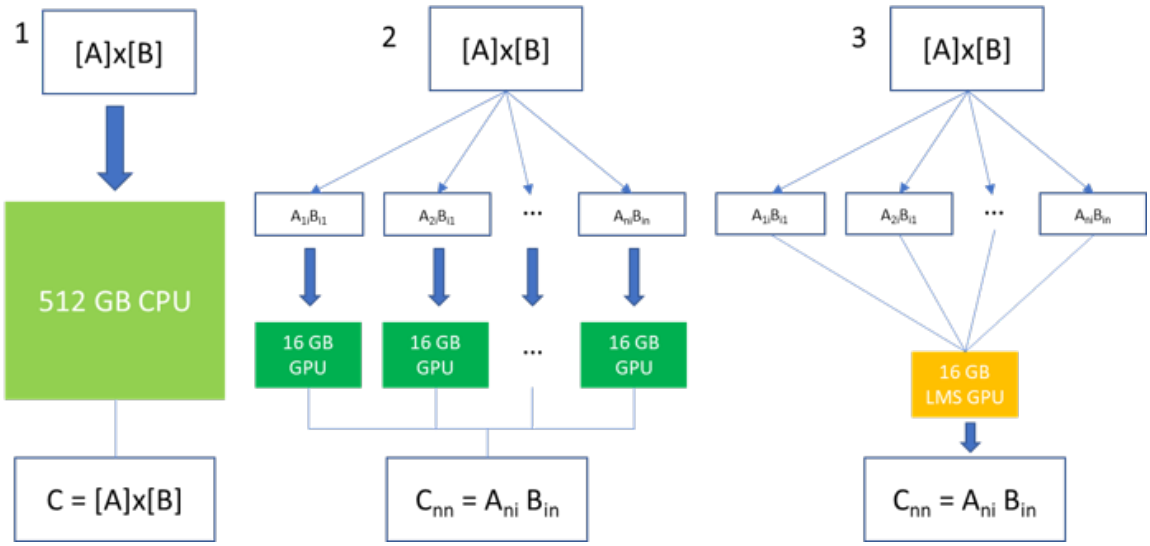

Figure 4-6: Hardware approaches for scaling AUTOMAP

However, all three of these hardware implementations have significant drawbacks, and for a full size 512x512 CT image, would take up to several weeks to train. With a pytorch implemenation on a DGX cluster comprised of eight 16 GB GPUS, AUTOMAP was limited a maximum image size (singorams) of just under 200x200 pixels.

Ultimately, the best solution would be a decomposition of the fully connected layers themselves. One such method, first proposed by [UCL FOLKS et al], is called decomposed AUTOMAP (dAUTOMAP) which allows for equivalent or better performance for FFT reconstructions relative to AUTOMAP for a fraction of the GPU memory requirement. Using dAUTOMAP, training a 512x512 CT image requires 4 GB GPU RAM, as opposed to nearly 200 GB for naive AUTOMAP. This could expand use of AUTOMAP for clinical CT (and other radon-type reconstruction problems) to more common GPU clusters, such as the NVIDIA dgx used in this study.

We train dAUTOMAP on several different training sets under different parameters. We started with the standard MNIST dataset of 70,000 28x28 pixel handwritten

numbers.

Subsequent training sets were created from the 150,000 images from the RSNA intracranial hemorrhage CT data. These images, which come from a variety of scanners and comprise both pathologic and normal images. The images were pre-processed as follows:

- Convert to Hounsfeld Units (HU) using the DICOM header data
- Windowed to head CT viewing range
- Rescaled to 8 bits
- Min-max scaled from 0 to 1
- Rescaled to desired dimensions
- Sinogram created by radon transform (parallel emission).

We test 28x28 MNIST images, and 32x32, 32x64, 64x64, 256x256, 512x512, and 100x512 CT images (sinogram size, projections x dimension).

For the 64x64 images, we tested several different levels of noise. Noise was simulated by adding Poisson noise at various levels directly to the sinograms.

Results

The performance of dAUTOMAP relative to conventional to solve the inverse radon problem was highly dependent on several image parameters. In general, dAUTOMAP's performance relative to FBP declined as the image (and projection number) increased. dAUTOMAP greatly outperformed FBP for the 28x28 MNIST images, and produced comparable images of 32x32, 32x64 and 64x64 CT reconstructions. Both AUTOMAP and dAUTOMAP produced noticeable blurrier reconstructions at 256 and 512 (half- and full) sized images, regardless of the number of projections.

However, dAUTOMAP did perform better relative to FBP in the reconstruction of noisy images. As per a structural similarity index measurement (SSIM), dAUTOMAP on average begins to outperform FBP when Poisson noise greater than 20% of the original pixel intensities is added to to the sinogram.

Discussion

Discrete source CT system face a difficult engineering tradeoff between the number of sources, and the size of each source. More sources mean that each source has to

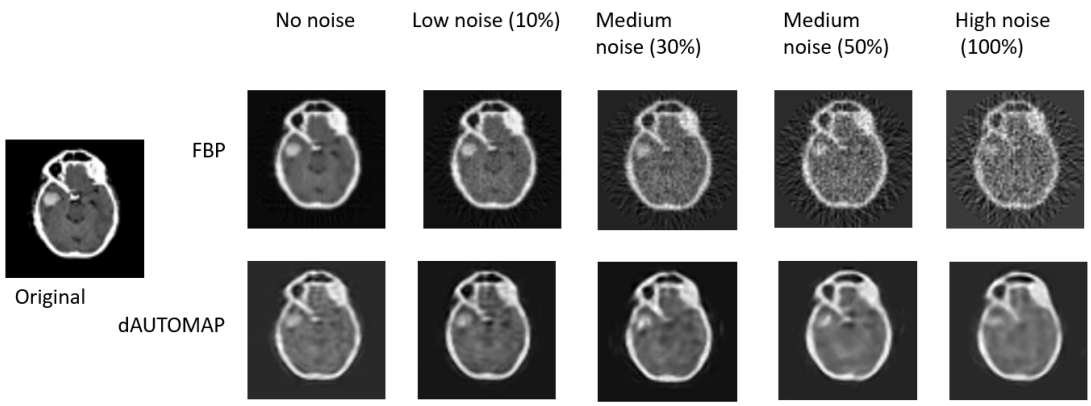

Figure 4-7: Comparison of dAUTOMAP and FBP SSIM loss, average on a 10,000 image testing set.

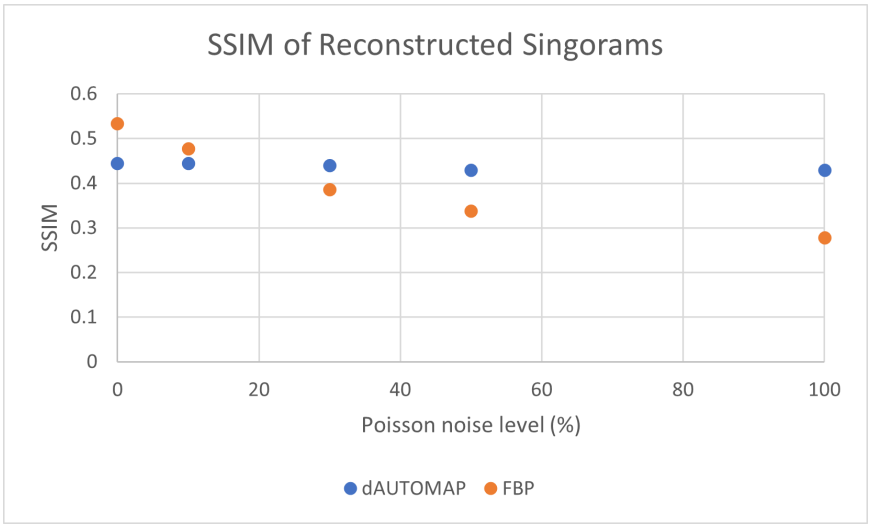

Figure 4-8: Comparison of dAUTOMAP and FBP SSIM loss, average on a 10,000 image testing set.

be smaller (occupying a smaller radial angle), possibly reducing the maximum x-ray flux. A higher source flux means better SNR on each projection; a higher number of sources means a more densely sampled sinogram. Exploiting modern ML techniques to solve one or both of the these problems will likely be helpful in bringing discrete source CT architectures to clinical practice.

The filter of Filtered Back Projection not does not change with input. By contrast, machine learning approaches can learning the specific noise pattern of the device.

Our results on noisy data here provide evidence that a ML algorithm trained on data produced by the specific device could be a way of compensating for the reduced SNR from low flux sources.

Conclusions

Our findings suggest that machine learning can be a valuable tool in reconstruction problems. In particular, we find that dAUTOMAP outperforms the conventional method of sinogram reconstruction when the signal-to-noise ratio was high.

Chapter 5

Conclusions and Future Work

5.1 Conclusions

In this thesis, I present advances in three different domains of x-ray imaging: source design, planar image acquisition, and tomographic image reconstruction. In addition to the immediate findings of each of these advances, these findings together provide evidence that

1) Tomographic x-ray imaging can be realistically accomplished by a distributed array small, pulseable cold-cathode sources.

2) Pulseable x-ray sources can allow for novel, time-dependent imaging modalities. These modalities can be used to extract mechanical (in addition to radioabsorption) data, and possibly to reduce radiation dose in x-ray imaging.

3) Modern signal processing algorithms, tailored specifically to the system being developed, can be used to improve image quality. However, it is unlikely that overlapping projections from different sources on to the same detector can be used to compensate for low source flux.

Nonetheless, the work presented has many possibilities for future research. Here, I highlight a few avenues for research that are particularly pressing.

5.2 Future work

Smaller spot size

Both the photocathode x-ray source and the silicon chip field emitter lacked a focusing apparatus for the electron beam.

A focusing apparatus could reduce the spot size further, and potentially enable applications that require a micro-focus spot. Most notably, this includes mammography, but a small spot sizes are important for any imaging geometry in which there is magnification of the object. Adding a focusing apparatus, such an an Einzel lens, would be a relatively simple (from a technical standpoint) way to improve the spot size of a cold-cathode source.

However, all of these sources we developed made use of a non-rotating anode. An x-ray device with a small spot size and a fixed anode may have significant heat dissipation concerns- after all, 99% of the energy in a Bremsstrahlung process is converted to heat, and could possible vaporize the anode (this is the mechanism by which e-beam sputtering is accomplished).

For an x-ray imaging system with distributed sources and (distributed) stationary anodes, care must be given to balance the duty cycle of electron beam at each anode with the current and voltage of the electron beam, or else the anode material will begin to coat inside of the x-ray tube.

Multi-modal imaging

Portable, discrete x-ray sources such as the ones described in chapter 2 could be used in conjunction with other medical imaging modalities.

In particular, PET/CT and CT/MRI have strong clinical motivations, and would benefit from the small footprint electron sources described in this thesis. Pairing cold-cathode x-ray sources with a portable, low-field MR (such as the Hyperfine system) in particular is a compelling application of such x-ray sources

Expanding machine learning techniques

As with any machine learning technique, substantial verification that the algorithm is not inventing things. This is particularly important in diagnostic image

reconstruction, as even minor additions or deletions could affect life-or-death decision making. Verification and ethics of AI in medicine is beyond the scope of this thesis, but readers hoping to continue developing AUTOMAP, dAUTOMAP and similar ML reconstruction algorithms are encouraged to pursue those topics rigorously.

Chapter 6

Epilogue: medical engineering in the pandemic

I wanted to include a historical marker for the future reader, as a reference for what it was like to finish a doctorate during the most turbulent era in living memory. While my experience may sound painfully familiar for you if you lived in the Northeast between March and October 2020, I imagine - and hope - that this document will be read by some of you who lived elsewhere, may not have been born yet, or have merely forgotten this era.

The summer of 2020 was a period of profound grief and suffering in many ways, but effects of the global coronavirus pandemic far outstripped those of the other natural and social disasters. At the time of writing there have some 200,000 confirmed deaths to COVID-19 in the US alone. My defense, like all of the PhD defenses for the foreseeable future, was conducted virtually.

The stay-at-home advisory (it was never technically an order in Massachusetts) brought with it some unexpected joys. I moved back home with my parents for the longest period of time since high school, and brought with me my girlfriend- after we had been dating for only a few weeks, since we would not have been able to see each other living in different households. With my usual hobbies of climbing and backcountry skiing denied (and access to my parents' woodshop restored), we embarked on a couple of ambitious woodworking projects, including a pair of Telemark

skis and a 17-foot strip-planked kayak.

I drove in to town run tests and errands a few days a week at MIT, HMS, and DFCI (access to my usual lab at MGH would not be restored until June). The campuses were ghost towns, and ominous 'auxiliary' treatment bays clogging the entrances of the hospitals.

In the initial days of the case surge in Boston, fears for the health and safety of healthcare providers was an overriding concern. These fears were underscored by dramatic shortages in personal protective equipment (PPE), which dominated not just the my conscience, but national news. As of mid-October, some 1,300 American healthcare providers have died from COVID-19.

Our first project was to re-purpose a then-idle cobalt irradiator for the re-use N95 respirators, as the effects of gamma radiation of respirator function would have had relevance for the many radiation oncology gamma sources that were also idle in hospitals across the country, as all but the most urgent of cancer treatments had been postponed.

6.1 Assessment of the Qualitative Fit Test and Quantitative Single-Pass Filtration Efficiency of Disposable N95 Masks Following Gamma Irradiation

Adapted from: Assessment of the Qualitative Fit Test and Quantitative Single-Pass Filtration Efficiency of Disposable N95 Masks Following Gamma Irradiation May 26, 2020. doi:10.1001/jamanetworkopen.2020.9961

Introduction

The coronavirus disease 2019 pandemic has led to a dramatic shortage of masks and other personal protective equipment in hospitals around the globe. One component of personal protective equipment, the disposable N95 face mask, is in particular

demand [33, 8] To alleviate a shortage of N95 masks, many methods to resterilize them have been proposed and studied [143]. Any method for resterilizing masks must not degrade the filtration efficiency of the mask.

This quality improvement study examines cobalt-60 gamma irradiation as a method of N95 mask sterilization. Viral inactivation of severe acute respiratory syndrome coronavirus has been reported at radiation doses of 10 kGy at most, with other studies supporting a radiation dose of 5 kGy for many types of viruses [32, 137]

Gamma irradiation has certain logistical advantages over other sterilization methods but there is a concern that radiation may damage the mask by cross-linking polymers within it and make them brittle. Ionizing radiation can disrupt the electrostatic charge distribution in the electret material of the mask and reduce its filtration efficiency against submicron particles [48].

Methods

This study was performed as part of hospital operations and infection control and, as per Massachusetts General Hospital policy, did not require institutional review board approval. This study follows the Standards for Quality Improvement Reporting Excellence (SQUIRE) reporting guideline.

A set of 3M 8210, 1805, and 9105 masks were irradiated using a cobalt-60 irradiator (GammaCell 220 E; Atomic Energy of Canada) at the Massachusetts Institute of Technology. Three masks of each type received 0 kGy (control), 1 kGy, 10 kGy, and 50 kGy of approximately 1.3 MeV gamma radiation from the source, at a dose rate of 2.2 kGy per hour.

The control (0 kGy) and 3 sets of irradiated masks (1, 10, and 50 kGy) were subjected to the Occupational Safety and Health Administration Gerson Qualitative Fit Test 50 (saccharin apparatus) by 1 of the authors (M.S.) and a Partners Healthcare physician in a blinded fashion. Another set of control and irradiated masks were tested for their particulate single-pass filtration efficiency. These masks were inserted into a specialized air duct, and ambient particulate matter was driven through the duct and the mask. The pressure differentials and flow velocities are shown in the Table. Three different particle sizes—0.3, 0.5, and 1 μm—were tested, and the single-pass filtration

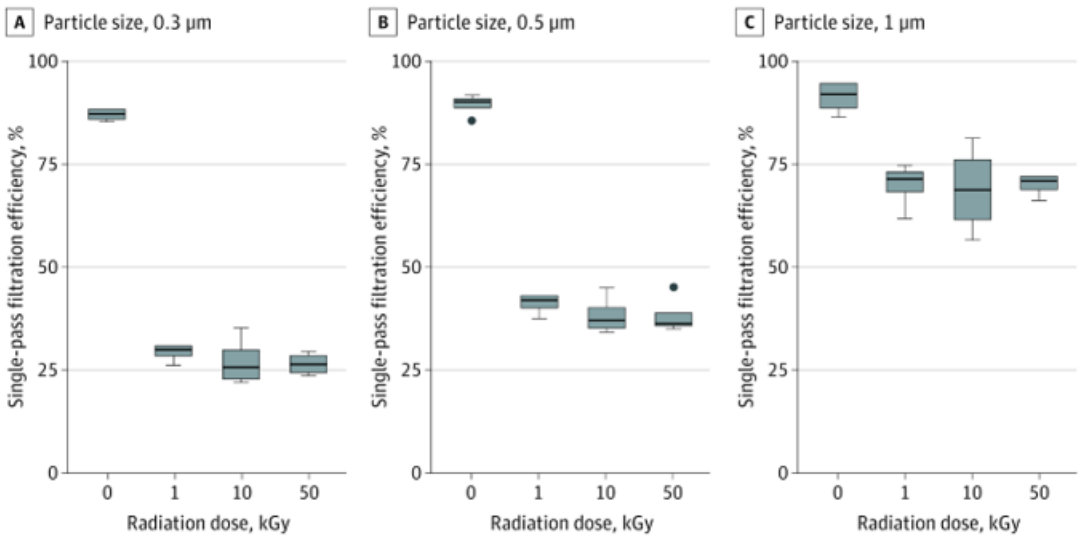

Figure 6-1: Box plots show data from a given particulate size for N95 masks that received 0, 1, 10, and 50 kGy gamma radiation doses from a cobalt-60 source. Tops and bottoms of boxes denote 75th and 25th percentiles, respectively. Lines within boxes denote medians. Circles denote outliers. Error bars were calculated by 6 observations of the upstream and downstream particle concentration.

efficiency was measured using an optical particle counter (Aerotrak 9306; TSI Inc). The measurement system, which was not calibrated for N95 mask certification, was only used to assess the relative changes in the filtration efficiency.

Statistical analyses were performed using R statistical software version 3.6.3 (R Project for Statistical Computing) with the level of significance set at $P < .05$. All tests were 2-sided. A linear mixed effects model was performed to assess the effects of dose (untreated, 1 kGy, 10 kGy, and 50 kGy) on the filtration efficiency of particles of 3 different sizes (0.3 μm, 0.5 μm, and 1 μm) using 2 masks per condition with 2 mask types (9105 and 8210). A Tukey honestly significant difference test was performed for the post-hoc analysis. Because of a lack of availability at the time of testing, we had to substitute the 1805 for the 9105 masks at 1 kGy. Data analysis was performed in April 2020.

Results

Nine of 9 of the tested control and irradiated masks, when donned properly, passed the qualitative fit test. Single-pass filtration data are shown in the Table and in the Figure. There was statistically significant degradation of filtration efficiency for all

Table. Single-Pass Filtration Efficiencies for Ambient Particles of Irradiated N95 Masks

Mask model and dose[a]	Single-pass filtration efficiency, mean (SD), %			Air pressure differential, Pa	Air flow velocity m/s	Temperature, °C	RH, %
	0.3 µm	0.5 µm	1 µm				
9105, 0 kGy							
Mask 1	85.9 (3.9)	89.5 (4.5)	94.3 (4.1)	175.5	0.4	23.7	11.5
Mask 2	88.3 (3.5)	90.2 (3.6)	94.7 (3.6)	185.8	0.4	23.9	19.5
1805, 1 kGy							
Mask 1	29.2 (1.4)	41.1 (1.4)	70.3 (8.2)	186.1	0.1	23.9	20.4
Mask 2	31.1 (1.8)	43.0 (4.4)	72.1 (10.6)	186.6	0.1	23.8	20.6
9105, 10 kGy							
Mask 1	28.3 (1.1)	38.6 (2.5)	74.3 (8.1)	176.8	0.4	23.2	12.1
Mask 2	22.2 (1.1)	35.5 (3.2)	63.1 (11.1)	186.0	0.4	23.9	20.4
9105, 50 kGy							
Mask 1	24.8 (1.0)	36.7 (2.7)	69.5 (11.4)	176.8	0.4	23.1	12.4
Mask 2	23.8 (0.8)	35.1 (1.9)	72.0 (12.2)	184.2	0.4	23.9	20.2
8210, 0 kGy							
Mask 1	88.1 (1.9)	91.4 (1.8)	89.2 (2.7)	173.9	0.4	22.9	11.3
Mask 2	85.0 (2.2)	85.4 (1.7)	86.2 (3.5)	191.7	0.4	23.6	21.1
8210, 1 kGy							
Mask 1	30.8 (0.8)	43.1 (3.7)	75.0 (9.5)	185.0	0.4	23.7	21.2
Mask 2	26.2 (1.4)	37.4 (2.0)	61.6 (10.7)	187.1	0.4	23.7	21.4
8210, 10 kGy							
Mask 1	35.2 (0.9)	45.0 (2.8)	81.0 (5.7)	179.2	0.4	23.1	11.7
Mask 2	23.3 (1.6)	34.3 (2.5)	56.3 (13.0)	185.5	0.4	23.7	21.4
8210, 50 kGy							
Mask 1	28.2 (1.1)	36.0 (2.3)	66.0 (9.9)	186.1	0.4	23.6	21.4
Mask 2	29.6 (1.0)	45.2 (2.1)	71.9 (9.2)	186.4	0.4	23.7	21.2

Abbreviation: RH, relative humidity.

[a] All masks were manufactured by 3M.

Figure 6-2: Single-Pass Filtration Efficiencies for Ambient Particles of Irradiated N95 Masks

treated masks. For example, for 1 of the 9105 masks, mean (SD) filtration efficiency for 0.3 μm particles decreased from 85.9% (3.9%) at 0 kGy to 28.3% (1.1%) at 10 kGy, and for 1 of the 8210 masks, mean (SD) filtration efficiency for 0.3-μm particles decreased from 88.1% (1.9%) to 30.8% (0.8%) at 1 kGy (for particle size, F=59.0002; for radiation dose, F=75.6986; P<.001 for both). However, there was no difference in filtration efficiency between the masks irradiated at 1 kGy (mean [SE] estimate, 42.275 [3.542]), 10 kGy (mean [SE] estimate, 44.258 [23.542]), or 50 kGy (mean [SE] estimate, 44.117 [3.542]). For example, for 1 of the 8210 masks, the mean (SD) filtration efficiency for 0.3-m particles was 26.2% (1.4%) at 1 kGy, 23.3% (1.6%) at 10 kGy, and 29.6% (1.0%) at 50 kGy. The filtration efficiency for 1 μm particles was greater than that for 0.5 μm particles (mean [SE] estimate, 23.125 [3.068]; z=7.538; P<.001) which, in turn, was greater than that for 0.3 μm particles (mean [SE] estimate, 9.219 [3.068]; z=3.005; P=.007).

Discussion

This study has limitations. The test we used to assess filtration efficiency is not approved by the National Institute for Occupational Safety and Health, and particulate matter smaller than 0.3 μm was not examined. The number and type of masks studied was limited by the current supply shortage. However, these findings suggest that a qualitative fit test alone is unable to fully assess mask integrity and that at the doses required for sterilization, gamma radiation degrades the filtration efficiency of N95 masks.

6.2 Analysis of SteraMist ionized hydrogen peroxide technology as a method for sterilizing N95 respirators and other personal protective equipment

With gamma radiation (and ionizing radiation in general) shown to be unlikely to work as a means of N95 sterilization, we turned to looking at ionized hydrogen peroxide (iHP). This system was already installed at the Dana-Farber Cancer Institute, so it was advantageous as it was within the hospital center itself.

Adapted from **Analysis of SteraMist ionized hydrogen peroxide technology as a method for sterilizing N95 respirators and other personal protective equipment** (Cramer et al, *Scientific Reports* [under review])

Abstract

Objectives: The COVID-19 pandemic has led to widespread shortages of personal protective equipment (PPE) for healthcare workers, including filtering facepiece respirators (FFRs) such as N95 masks. These masks are normally intended for single use, but their sterilization and subsequent reuse could substantially mitigate a world-wide shortage.

Methods: In this study, we investigate PPE sterilization using ionized hydrogen peroxide (iHP), generated by SteraMist equipment (TOMI; Frederick, MD), in a sealed environment chamber installed in the animal facility of an academic medical center. PPE, including five N95 mask models from three manufacturers, were eval-

uated for efficacy of sterilization following iHP treatment (measured with bacterial spores in standard biological indicator assemblies). Additionally, N95 masks were assessed for their ability to form an airtight seal using a quantitative fit test. Finally, filtration efficiency down to 0.3 μm particles was measured using ambient particulate matter at a university lab and an aerosolized NaCl challenge at a National Institute for Occupational Safety and Health (NIOSH) pre-certification laboratory.

Results: The data demonstrate that N95 masks sterilized using SteraMist iHP technology retain function up to ten cycles, the maximum number tested to date. Some but not all PPE could also be sterilized using an iHP environmental chamber, but pre-treatment with a handheld iHP generator was required for semienclosed surfaces such as respirator hoses.

Conclusions: A typical iHP environment chamber with a volume of 80 m^3 can treat up to 7000 masks per day, as well as other items of PPE, making this an effective approach for a busy medical center.

Introduction

The COVID-19 pandemic has led to widespread shortages in personal protective equipment (PPE) for clinicians and first responders. Shortages in filtering facepiece respirators (FFRs) such as N95 "masks", which are certified to filter 95% of airborne particles down to 0.3 μm, are particularly problematic because these normally single-use items are a mainstay of infection control. It has been widely reported that the US Department of Health and Human Services (HHS) anticipates a need for as many as 3.5 x 10^9 N95 masks in 2020 for US use alone, but estimates of total available supply are far short of that number [17]. The consequent need for N95 mask sterilization and subsequent reuse is therefore likely to continue for the foreseeable future. The possibility that disposable N95 masks could be sterilized and reused was raised 15 years ago as a strategy to address shortages arising from medical emergencies, but with the exception of a single FDA-funded study by the Battelle Memorial Institute, little subsequent research was performed on the topic [112, 18, 7]. Recently, in response to acute N95 mask shortages, multiple strategies for mask sterilization have been proposed and studied, including exposure to ultraviolet (UV) germicidal irradiation,

Company	Products	Technology	Technology of delivery	Existing Use for N95 Sterilization
Bioquell	Bioquell Clarus C; Bioquell Z-2; Bioquell ProteQ	**HPV** *Hydrogen Peroxide Vapor*	30-35% liquid H_2O_2 vaporized and delivered into a chamber; saturated H_2O_2 condenses on surfaces[6,14,15,18]	EUA granted (3/28/2020) to Batelle to use Bioquell as part of its Critical Care Decontamination System for up to 20 cycles of N95 mask reuse[30]
Steris Corporation	STERIS V-PRO 1 Plus, maX and maX2 Low Temperature Sterilization Systems	**VHP™** *Vaporized Hydrogen Peroxide*	30-35% liquid H_2O_2 is vaporized and delivered into a dehumidified chamber; concentration is held below condensation point[16]	EUA granted (4/10/2020) to Steris Corporation for STERIS V-PRO 1 Plus, maX and maX2 Low Temperature Sterilization Systems for up to 10 cycles of single-user reuse[31]
Advanced Sterilization Products (ASP)	STERRAD 100S H2O2 Gas Plasma Sterilizer; STERRAD NX H2O2 Gas Plasma Sterilizer; STERRAD 100NX H2O2 Gas Plasma Sterilizer	**HPGP** *Hydrogen Peroxide Gas Plasma*	58-60% liquid H_2O_2 is vaporized into a chamber; radiation frequency energy is targeted into the chamber, exciting the H_2O_2 to a low-temperature plasma state[12,20]	EUA granted (4/12/2020) to ASP for STERRAD 100S Cycle, STERRAD NX Standard Cycle, or STERRAD 100NX Express Cycle for up to two cycles in Tyvek pouching for single-user reuse[29]
TOMI	SteraMist Binary Ionization Technology (BIT)	**iHP™** *ionized Hydrogen Peroxide*	7.8% aqueous H_2O_2 aerosolized. 0.05-3 µm droplets are pushed past a cold plasma field generated by two electrodes and ionized into hydroxyl radicals[32]	The topic of this study. Currently being investigated for sterilization of PPE for re-use in academic medical centers

Figure 6-3: Commercial vaporization and ionization-based hydrogen peroxide sterilization technologies,

vaporized hydrogen peroxide, moist heat, ethylene oxide, and gamma irradiation [26, 70, 144, 143]. In this study, we evaluate a recently developed technology, ionized hydrogen peroxide (iHP), as a method for sterilizing N95 masks and other PPE.

Hydrogen peroxide (H_2O_2) is a powerful sterilizing agent that can be used on porous and other surfaces following vaporization or ionization to create a mist containing hydroxyl radicals. Such vaporized or ionized hydrogen peroxide methods (VHP/iHP) are widely used for environmental sterilization across multiple industries including food preparation, healthcare, and life sciences [64, 47, 61, 114, 123, 34]. VHP/iHP methods can be used on a wider range of sensitive materials than high temperature methods (e.g. autoclaving) and are safer than ethylene oxide methods. Four distinct VHP/iHP-based H_2O_2 sterilization technologies that have been commercialized to date are shown in Table 1, each of which involves a different approach to generating and delivering the sterilant. In all cases microbial killing is achieved through the reaction of hydroxyl radicals with proteins, nucleic acids and other biomolecules in pathogens. Three VHP-based systems have received emergency use authorization (EUA) from the Food and Drug Administration (FDA) for N95 mask decontamination, even though relatively limited peer-reviewed data is avail-

able, particularly from non-commercial third parties.

As a consequence, it is difficult for infection control teams in hospitals and other healthcare providers to evaluate these systems. The absence of data on the post-sterilization performance of different makes and models of N95 masks is also limiting. The Brigham and Women's Hospital (BWH; Boston MA) Incident Command, which is involved in this study, currently has on hand over 30 models of N95 masks from three manufacturers.

This study focuses on the use of iHP as a N95 mask sterilization method, specifically the SteraMist Binary Ionization Technology (BIT) from TOMI (Beverly Hills, CA). iHP was registered with the Environmental Protection Agency (EPA) in 2015 for use in health care, life sciences, food safety, and other settings (appearing on EPA lists G, H, K, L, and M). Most recently it was added to EPA List N: Disinfectants for Use Against SARS-CoV-2, for use on hard, nonporous surfaces [141]. The active ingredient in iHP is 7.8% aqueous H_2O_2 (an H_2O_2 concentration 5 times lower than used in commercial VHP systems), which is flowed past a plasma arc and dispersed into a treatment chamber as a mist of micron-sized liquid droplets. As it passes through the plasma, the hydrogen peroxide is ionized into reactive hydroxyl radicals, the active sterilant. iHP is commercially available in two implementations: a handheld sprayer device ("Surface Unit") and an environmental unit ("Environment System").

The environment system used in this study was installed at the Dana-Farber Cancer Institute (DFCI; Boston, MA) animal research facility for use in sterilizing incoming equipment and materials. Following cycles of sterilization, masks were tested for three critical features: (1) sterility, as measured by the inactivation of bacterial spores contained in biological indicators; (2) filtration efficiency, measured both by aerosolized 75 nm NaCl particles and by 0.3-1 μm ambient particulate matter; and (3) fit, using a PortaCount quantitative fit test apparatus. Multiple sterilization cycles were completed to assess mask durability. Sterilization of other PPE items such as face shields and hoods and hoses for Powered-Air Purifying Respirators (PAPRs) was also explored. Testing was performed at the DFCI, MIT and ICS Laboratories (a commercial laboratory accredited to perform testing to NIOSH/ISO/IEC standards).

Methods

Selection of N95 respirators and other PPE samples

A total of 83 N95 masks representing five models from three manufacturers (3M 1860, Kimberly-Clark [KC]/Halyard 46767 "duckbill," Gerson 2130, 3M 8210, and 3M 9210/37021) were selected for testing as a representative sample of the N95 masks used in three local hospitals: Dana-Farber Cancer Institute, Brigham and Women's Hospital, and Boston Children's Hospital. N95 masks of the same model available in different sizes (for example, the 3M 1860 and the 3M 1860S, representing regular and small sizes) were considered to be interchangeable for testing purposes. The total sample size was necessarily limited by existing mask shortages and the importance of prioritizing the needs of healthcare workers; given the uniformity of the results reported below, the sample size was judged to be adequate.

Additionally, an assortment of other PPE and hospital equipment was selected for sterilization. This included the following PAPR components: Sentinel XL CBRN hood with hose, Sentinel head cover hoods, Sentinel PAPR breathing tubes for use with Sentinel XL HP PAPR (ILC Dover, Frederica, DE), and Bullard RT Series PAPR hood (Bullard, Lexington, KY). Other equipment included two models of face shields, one locally fabricated and the other a Fisherbrand Disposable Face Shield (Fisher Scientific, Waltham MA), a DuPont Tyvek 400 coverall (Wilmington, DE), an iPad (Apple, Cupertino CA), and an iPad case. The iPad was included for testing since BWH is making them available to COVID-19 patients as a means of communicating with family members.

A first set of 30 N95 masks representing five different models was processed using the SteraMist system for zero to five cycles, and then analyzed for single-pass filtration efficiency using ambient particulate matter at MIT. A second set of 44 N95 masks was processed using the SteraMist system and sent to ICS Laboratories (Brunswick, OH) for testing to an abbreviated (instantaneous only) or full loading NIOSH N95 filtration efficiency protocol. Nine masks underwent a quantitative fit test at DFCI following sterilization.

Sterilization in a SteraMist environment chamber

Sterilization of N95 masks and other PPE was accomplished using a SteraMist-equipped room (dimensions 5.64 m x 4.57 m x 3.05 m) at the DFCI animal research facility. Three SteraMist environmental units (room version TPO-302-PLC-V1.4) are mounted on the ceiling of the room and can be controlled via a single panel, accessible from the outside. iHP mist was delivered through three nozzles at a total of 90 mL/min for 15 min, yielding a delivered concentration of 17.7 mL/m^3.

N95 masks were placed with their interior surfaces facing up on standard stainless-steel shelves (open grid, InterMetro style). Most of the other PPE was also laid out on these shelves with the exception of two PAPR hoods, one PAPR hose, and the Tyvek coverall, which were hung in various configurations. PPE was spaced 6 cm to 20 cm apart on each shelf; this was designed to test sterilization performance at multiple points in the chamber. Tighter but non-overlapping spacing would likely be necessary for processing equipment in higher volumes.

Two PAPR hoods, one PAPR hose, and one face shield were pre-treated with a SteraMist handheld spraying device in advance of processing in the SteraMist-equipped chamber. Pre-treatment was intended to ensure delivery of sterilant to items with semi-enclosed surfaces (such as the inside of a PAPR hose). Treating these items with the handheld device consisted of spraying the equipment from a distance of approximately 0.5-1m for a few seconds per surface. Per manufacturer protocol, the 100-minute sterilization cycle in the environmental chamber included: an initial 15-minute fill phase during which the mist was released; a 20-minute dwell phase to allow the mist to penetrate the room; and a 65-minute scrub phase during which the exhaust was re-opened to aerate the space at a rate of 43 air changes per hour. The room is tested and calibrated quarterly to ensure homogeneous sterilization throughout the space.

Evaluating sterility using biological indicators

The efficacy of sterilization was evaluated using Apex Biological Indicators (BIs: Mesa Labs; Boseman, MT); bacterial spores in these indicators are more resistant to killing than most viruses and therefore provide a conservative and simple estimate of sterilization efficacy. In particular, the Geobacillus stearothermophilus spores used in

this study are known to be difficult to kill using hydrogen peroxide6. Each Apex biological indicator ribbon carries a minimum of 1.0 x 106 G. stearothermophilus spores. The BIs were positioned in the environmental chamber prior to the first sterilization cycle. For N95 masks, BIs were placed under or adjacent to the masks. For the PAPR components and other equipment, BIs were placed on surfaces that were judged to be least accessible to the sterilant (for example, inside the PAPR tubing). The BIs were extracted using sterile forceps, placed in Releasat growth medium (Mesa Labs), incubated at 55-60 , and monitored for bacterial growth over a period of 10 days using a colorimetric assay. Previous work with G. stearothermophilus spores suggests that a conservative benchmark for complete sterilization represents a 6-log10 kill; that is, a ratio in the number of surviving to initial viable spores in a BI of 10-6. This corresponds to no observable bacterial growth and thus no color change after 5 days in Releasat medium.

Evaluating filtration efficiency

Single-pass filtration efficiency testing was performed at MIT on five control N95 masks and 25 masks sterilized in the SteraMist-equipped chamber. An 8cm x 8cm sample of each N95 mask was inserted into a specialized air duct, and ambient particulate matter was driven through the duct, and thus through the mask fabric, using a pressure differential of roughly 175 pascals at 0.4 m/s face velocity. The concentration of 0.3, 0.5, and 1 μm diameter particles prior to and after passage through the mask fabric was determined using an Aerotrak 9306 optical particle counter (TSI Inc.; Shoreview, MN) (Table 2). Filtration efficiency testing was performed a second time on a subset of decontaminated masks stored for 10 days after treatment to test for time-dependent degradation in N95 mask performance following sterilization. Although readily available and potentially effective, testing performed at MIT is not equivalent to NIOSH-approved testing for N95 masks and thus, these results should be interpreted as a relative, not absolute, measurements of filtration efficiency.

A second sample of sterilized N95 masks was tested at ICS labs to NIOSH standards with 34 masks undergoing an instantaneous filter efficiency test and 10 masks undergoing a full loading filter efficiency test. Per NIOSH testing Procedure No.

TEB-APR-STP-0059 (rev. 3.2), all masks were challenged with a sodium chloride aerosol neutralized to a Boltzmann equilibrium state at 25 ± 5 and a relative humidity of 30 ± 10%. Particle size and distribution was verified to correspond to a median diameter of 0.075 ± 0.020 μm, with a geometric standard deviation ≤ 1.86. N95 masks were conditioned at 85 ± 5% relative humidity and 38 ± 2 for 25 hours prior to filter efficiency testing. For instantaneous filter efficiency testing, each mask was then assembled into a fixture and subjected to instantaneous aerosol loading. The loading was performed by depositing sodium chloride aerosol at an airflow rate of 85 liters per minute (LPM) for one minute. For full loading filter efficiency, each mask was assembled into a fixture and subjected to full aerosol loading. The loading was performed by depositing 200 mg of sodium chloride aerosol at an airflow rate of 85 LPM for 75 minutes. Flow rate was monitored every 5-10 minutes on average and adjusted to maintain a flow rate of 85 ± 2 LPM.

Quantitative fit testing

Nine masks from three models underwent a quantitative fit test following 2, 5, and 10 sterilization cycles to confirm that sterilization did not interfere with the ability of masks to form an effective seal with the human face. Testing was performed using a PortaCount Pro+ 8038 fit tester (TSI Inc.; Shoreview, MN) set to the 100-200 fit factor range, per manufacturer recommendation.

Results

Evaluating sterilization using biological indicators

All BIs placed under or adjacent to N95 masks that had been exposed to a single sterilization cycle in the SteraMist-equipped chamber exhibited at least a 9-log10 kill (representing no color change following seven days of incubation in Releasat medium). BIs placed within PAPR hoods also achieved 9-log10 kill as did a BI placed in a PAPR hose that was pre-treated using a SteraMist handheld spraying device. BIs placed on the iPad, iPad case, and PanFab face shield designs all passed the sterilization threshold, and the iPad was observed to be fully functional after one cycle of iHP treatment. In contrast, two BIs placed inside either end of a PAPR hose that was not subjected to pre-treatment were not sterilized, as determined by rapid bacterial

growth following transfer to Releasat medium. This was also true of a BI embedded in the thick foam at the top of a Fisherbrand Disposable Face Shield. We tested the effect of pretreating the same face shield with a hand-held SteraMist device (after inserting a new BI) and observed a 4-log10 kill, which also fails the 6-log10 threshold conventionally used to score successful sterilization.

From these data we conclude that a single iHP cycle is efficacious at sterilizing N95 masks and other equipment placed throughout a SteraMist-equipped decontamination chamber and that the process is not obviously damaging to delicate equipment such as an iPad (n = 1). Penetration into semi-enclosed spaces such as PAPR hoses appeared to be less efficient, but such equipment could be sterilized by pre-treatment with a handheld iHP-delivery device followed by a cycle of iHP treatment in a chamber. Even with pre-treatment sterility was not achieved with thick face shield foam, suggesting that such normally disposable PPE should not be reused. In contrast, a custom-fabricated face shield[87] introduced under an FDA EUA and consisting of 3D printed parts appeared to be sterilized effectively.

Evaluating filtration efficiency

Performance data was collected at MIT on five models of N95 masks from three manufacturers (a total of 30 units) using an ambient particulate matter filtration efficiency test. Relative to control N95 masks, we observed no reduction in filtration efficiency for 0.3, 0.5, and 1 μm particles by N95 masks subjected to up to ten sterilization cycles (Table 2).

In addition, five models of N95 masks from three manufacturers (44 units total) were evaluated using testing protocols derived from NIOSH published standard testing procedures (STPs) maintained by ICS Laboratories. These data showed that 34 iHP-sterilized N95 masks retained instantaneous filtration efficiencies of $\geq$95%, including masks subjected to five sterilization cycles, the maximum number of cycles tested (Figure 1, Table 3, and Table 4). Gerson 2130 N95 masks were the least effective at filtering 75nm NaCl particles, but even these units passed the instantaneous test threshold out to five sterilization cycles. In no case did we detect an appreciable increase in resistance to airflow, a change which would likely be perceived by users as

increased inhalation resistance.

Fully loaded filtration efficiency was also evaluated by ICS Laboratories to NIOSH standards. The purpose of this test is to mimic the effect of an accumulation of charged particles in a mask, a phenomenon related to time of use. Mask loading is known to reduce filtration efficiency, potentially by weakening electrostatic charge in the filtering layer [81]. Again, we observed that the 10 sterilized masks passed the NIOSH threshold for N95 pre-certification.

To test for time-dependent degradation of performance, 30 N95 masks were tested at MIT 10 days after initial filtration testing and 10-15 days after sterilization with iHP. We observed no difference in filtration performance between measurements taken immediately after sterilization, and those taken 10 days after, as determined by a repeated measures ANOVA ($p = 0.45$). From these data we conclude that the filtration efficiency of multiple models of domestically manufactured N95 masks is not substantially affected by one to ten cycles of iHP sterilization in terms of filtration efficiency or inhalation resistance, and that all masks tested meet existing NIOSH pre-certification standards.

PortaCount quantitative fit data

All nine masks that were tested for fit (KC/Halyard 46767, 3M 1860, 3M 8210) using the PortaCount equipment passed a reading of >200 fit factor following 2, 5, and 10 sterilization cycles. This corresponds to a filtration efficiency of 99% or higher (data not shown) according to manufacturer guidelines. Thus, iHP sterilization does not appear to impair the ability of N95 masks to form an effective seal against a user's face.

Discussion

Hydrogen peroxide has a long history of successful use in the field of medical device sterilization, and our results support the use of iHP as a PPE sterilant when delivered using a SteraMist-equipped environment chamber, in some cases complemented by pre-treatment with a handheld iHP delivery device. Thus, iHP sterilization can likely be used to extend the usability of PPE such as N95 masks that are usually disposed of after a single use. The DFCI SteraMist environment chamber used in this study has a

Model	Cycles	Filtration Efficiency (SD)		
		0.3µm	0.5µm	1.0µm
3M 1860	0	97.66% (0.18)	99.05% (0.13)	99.68% (0.03)
	0	97.53% (0.18)	99.11% (0.23)	100.00% (0.00)
	1	99.20% (0.08)	99.70% (0.08)	99.90% (0.20)
	2	98.98% (0.10)	99.80% (0.06)	100.00% (0.00)
	2	99.42% (0.05)	99.89% (0.09)	99.91% (0.18)
	3	99.36% (0.12)	99.92% (0.06)	100.00% (0.00)
	4	98.55% (0.07)	99.59% (0.13)	99.88% (0.24)
	5	98.76% (0.03)	99.52% (0.16)	100.00% (0.00)
	10	98.45% (0.15)	99.39% (0.09)	100.00% (0.00)
KC/Halyard 46767 (duckbill)	0	99.91% (0.02)	99.95% (0.05)	100.00% (0.00)
	1	99.83% (0.07)	99.86% (0.17)	100.00% (0.00)
	2	99.91% (0.02)	99.98% (0.02)	100.00% (0.00)
	3	99.90% (0.04)	99.98% (0.04)	100.00% (0.00)
	4	99.69% (0.06)	99.80% (0.12)	99.89% (0.24)
	5	99.89% (0.03)	99.95% (0.07)	100.00% (0.00)
	10	99.86% (0.07)	99.97% (0.06)	100.00% (0.00)
Gerson 2130	1	96.06% (0.20)	98.90% (0.10)	99.68% (0.43)
	2	96.46% (0.19)	99.08% (0.11)	99.84% (0.19)
	3	95.17% (0.37)	98.80% (0.26)	99.65% (0.30)
3M 8210	0	98.09% (0.22)	99.42% (0.24)	99.82% (0.21)
	1	99.86% (0.04)	99.99% (0.02)	100.00% (0.00)
	2	99.52% (0.03)	99.93% (0.04)	100.00% (0.00)
	3	99.28% (0.06)	99.88% (0.04)	100.00% (0.00)
	4	98.90% (0.11)	99.40% (0.10)	100.00% (0.00)
	10	99.16% (0.15)	99.77% (0.13)	100.00% (0.00)
3M 9210/37021	0	99.75% (0.11)	99.92% (0.11)	100.00% (0.00)
	1	99.77% (0.16)	99.83% (0.19)	99.71% (0.37)
	2	99.70% (0.07)	99.92% (0.07)	100.00% (0.00)
	3	99.39% (0.18)	99.86% (0.04)	100.00% (0.00)
	4	98.68% (0.98)	99.01% (0.92)	99.05% (1.19)

Figure 6-4: Results obtained at a university laboratory on single-pass filtration efficiency for ambient particle matter. Each row represents a single N95 mask. Filtration efficiency values are an average of four upstream and downstream measurements.

Model	Cycles	Number of Masks	Flow Rate (LPM)	Resistance (mm of H2O)	Penetration (%)	Filter Efficiency (%)	Passed?
3M 1860	1	4	86	10.35	0.67	99.33	Yes
	2	5	86	9.78	0.53	99.47	Yes
	5	3	86	9.10	0.64	99.36	Yes
	10	3	86	9.17	0.60	99.40	Yes
KC/Halyard 46767 (duckbill)	1	1	86	15.20	0.11	99.89	Yes
	2	1	86	14.10	0.22	99.78	Yes
	5	3	86	14.33	0.11	99.89	Yes
Gerson 2130	1	1	86	9.30	1.31	98.69	Yes
	2	1	86	7.90	2.57	97.43	Yes
	5	1	85	9.80	1.35	98.65	Yes
3M 8210	1	2	86	8.85	0.24	99.76	Yes
	2	2	86	8.95	0.18	99.82	Yes
	5	3	85	9.40	0.28	99.72	Yes
	10	3	86	7.77	0.37	99.63	Yes
3M 9210	5	1	85	10.40	0.07	99.93	Yes

Figure 6-5: Results from ICS Laboratories on instantaneous filtration efficiency according to NIOSH standard Procedure No. TEB-APR-STP-0059. Each row represents data from 1-5 N95 masks and data are reported as the average for all tests that were performed.

Model	Cycles	Flow Rate (LPM)	Resistance (mm of H2O)	Initial Penetration (%)	Maximum Penetration (%)	Filter Efficiency (%)	Passed?
3M 1860	5	85	9.6	1.22	4.40	95.60	Yes
	5	85	9.8	0.94	4.11	95.89	Yes
	10	86	8.3	0.67	4.44	95.56	Yes
	10	86	8.9	0.62	3.79	96.21	Yes
KC/Halyard 46767 (duckbill)	5	85	15.5	1.40	1.40	98.60	Yes
	5	85	14.8	0.13	0.13	99.87	Yes
3M 8210	5	85	9.8	0.29	1.77	98.23	Yes
	5	85	9.9	0.49	1.84	98.16	Yes
	10	85	8.5	0.21	2.43	97.57	Yes
	10	85	10	0.23	2.17	97.83	Yes

Figure 6-6: Results from ICS Laboratories on full loading filtration efficiency according to NIOSH standard Procedure No. TEB-APR-STP-0059. Each row represents data from an N95 mask.

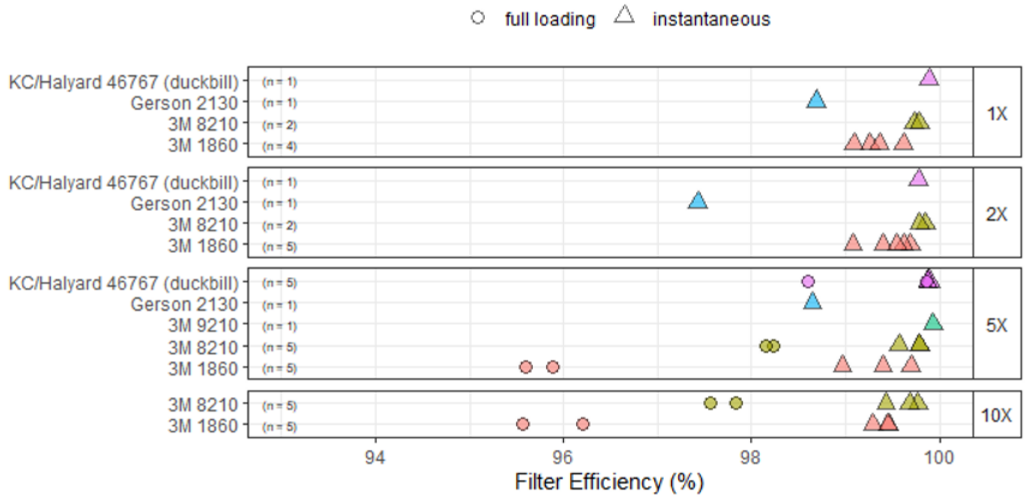

Figure 6-7: Instantaneous and fully-loaded ambient particulate matter filtration data for N95 masks over one, two, and five SteraMist sterilization cycles. Results were obtained from ICS Laboratories according to NIOSH standard Procedure No. TEB-APR-STP-0059. All masks passed ICS standards, including filtration efficiency of 95%.

volume of approximately 80 m^3 and could comfortably fit about 2400 N95 masks per cycle without the masks touching each other, or a lesser number of PAPR hoods and other PPE. At this rate, assuming idealized staffing and logistics, roughly 4,800-7,200 masks could be sterilized for use per day given a typical 100 minute sterilization cycle. These numbers could be increased with the addition of an overnight workforce.

In keeping with standard practice, sterility was judged in this study using biological indicators containing bacterial spores and was not based on killing of pathogens such as SARS-CoV-2 encountered in a clinical setting. However, the G. stearothermophilus spores in the BIs we used are known to be resistant to killing by hydrogen peroxide, and spores are substantially more resistant to sterilization than enveloped viruses such as SARS-CoV-227. Recent work has also demonstrated that VHP can kill SARS-CoV-2 [34]. Thus, we do not believe our use of BIs rather than direct measurement of viral viability represents a significant limitation in the interpretation of the data.

Two independent lines of evidence, one generated at a university laboratory and one at a commercial laboratory accredited to perform N95 mask certification to

NIOSH/ISO/IEC standards, show that N95 masks decontaminated with iHP using SteraMist technology retain their performance with respect to filtration and inhalation resistance for at least ten cycles, the maximum number tested. No deterioration was detected in masks tested 10 days post treatment. Quantitative fit testing of N95 masks sterilized up to ten cycles confirms that they still form an airtight seal as required. Thus, sterilized N95 masks remain fully functional.

Limitations of this study

The tests described in this study were conducted using unused N95 masks. We do not yet have data on N95 masks used in an actual health care facility responding to a pandemic. Among questions to be addressed by real-world testing are inhalation resistance for an N95 mask that has been loaded with internal and external contaminants, the comfort level of health care workers in using an N95 mask that is sterilized but previously used by another individual, and the rate of wastage arising from breakage of elastic bands, contamination with makeup or topical face products, and unacceptable degradation in fit. Remarkably, these types of real-world use data are not available for any iHP/VHP-based sterilization method, even for technologies that have been heavily promoted commercially. Nonetheless, the data reported in this study were judged by our clinical teams to be sufficient to implement N95 mask sterilization and reuse at DFCI.

Future work should address the question of whether decontaminated N95 masks must be returned to the original users (as specified in the Sterrad and Sterris EUAs for N95 mask decontamination) or can be returned to a common pool (as specified in the Batelle EUA); the latter is substantially easier to implement from a logistical perspective. Finally, while there is good support for the use of spore-based BIs in measuring the efficacy of sterilization, direct tests on SARS-CoV-2 itself may be warranted, particularly in the case of items such as hoses and other PPE that have a complex shape (this would require BL3-level studies).

Conclusions

Our data support the use of the SteraMist iHP technology as a sterilization method for reuse of N95 masks, including many of the most commonly used models, as well

as other types of PPE – in some cases following pre-treatment with an iHP hand-held delivery device. In interpreting these data, it is important to note that not all iHP/VHP methods are the same. While Bioquell is approved under an FDA EUA for 20 cycles, N95 masks sterilized using an alternative HPGP method commercialized by Sterrad fail at five cycles (the Sterrad EUA was approved for 2 sterilization cycles and requires that a mask be returned to a single user). Moreover, our data show that semi-enclosed items of PPE, such as PAPR hoses, cannot be sterilized without pre-treatment, and that face shields with thick foam may not be sterile even after iHP pre-treatment followed by iHP treatment in an environmental chamber. Thus, it is imperative that institutions seeking to deploy iHP/VHP technology review available primary data prior to local deployment. We also suggest that BIs routinely be deployed when attempting to sterilize hoses and other semi-enclosed PE components.

The issues described above about reuse of N95 masks have been recognized for over two decades based on multiple instances of human transmission of novel respiratory diseases. As the global response to COVID-19 evolves, we hope that the study of sterilization technologies such as iHP/VHP will continue and involve peer-review of independently acquired data so that we are in a better position for the coming waves of this crisis and for those in the future.

Bibliography

[1] Elastographic Tomosynthesis From X-Ray Strain Imaging of Breast Cancer. *IEEE Journal of Translational Engineering in Health and Medicine*, 7, August 2019.

[2] Hemant Kumar Aggarwal and Angshul Majumdar. Hyperspectral image denoising using spatio-spectral total variation. *IEEE Geoscience and Remote Sensing Letters*, 13(3):442–446, 2016.

[3] A.H. Andersen and A.C. Kak. Simultaneous algebraic reconstruction technique (sart): A superior implementation of the art algorithm. *Ultrasonic Imaging*, 6(1):81–93, 1984.

[4] Mark R. Bagg, Dana C. Covey, and Elisha T. Powell. Levels of medical care in the global war on terrorism. *The Journal of the American Academy of Orthopaedic Surgeons*, 14(10 Spec No.):S7–9, 2006.

[5] Israel Bar-David. Communication under the poisson regime. *IEEE Transactions on Information Theory*, 15(1):31–37, 1969.

[6] R. J. Batt and C. H. B. Mee. Effect of Film Structure on Photoelectric Emission from Thin Films of Aluminium. *Journal of Vacuum Science and Technology*, 6(4):737–740, July 1969.

[7] Battelle. Final Report for the Bioquell Hydrogen Peroxide Vapor (HPV) Decontamination for Reuse of N95 Respirators. Technical Report Study No 325, Food and Drug Administration, 2016.

[8] Howard Bauchner, Phil B. Fontanarosa, and Edward H. Livingston. Conserving Supply of Personal Protective Equipment—A Call for Ideas. *JAMA*, March 2020.

[9] Miriam H. Beauchamp, Michael Ditchfield, Franz E. Babl, Michael Kean, Cathy Catroppa, Keith O. Yeates, and Vicki Anderson. Detecting Traumatic Brain Lesions in Children: CT versus MRI versus Susceptibility Weighted Imaging (SWI). *Journal of Neurotrauma*, 28(6):915–927, April 2011.

[10] H. Bethe and W. Heitler. On the stopping of fast particles and on the creation of positive electrons. *Proc. R. Soc. Lond. A*, 146(856):83–112, August 1934.

[11] Bryan Blesdoe. Mobile Stroke Units: A Device in Search of an Indication. *Journal of Emergency Medical Services*, January 2017.

[12] Jean-Marc Bonard, Christian Klinke, Kenneth A. Dean, and Bernard F. Coll. Degradation and failure of carbon nanotube field emitters. *Physical Review B*, 67(11):115406, March 2003.

[13] Marouan Bouali and Saïd Ladjal. Toward optimal destriping of modis data using a unidirectional variational model. *IEEE Transactions on Geoscience and Remote Sensing*, 49(8):2924–2935, 2011.

[14] Ritvij Bowry, Stephanie Parker, Suja S. Rajan, Jose-Miguel Yamal, Tzu-Ching Wu, Laura Richardson, Elizabeth Noser, David Persse, Kamilah Jackson, and James C. Grotta. Benefits of Stroke Treatment Using a Mobile Stroke Unit Compared With Standard Management: The BEST-MSU Study Run-In Phase. *Stroke*, 46(12):3370–3374, December 2015.

[15] David J. Brenner and Eric J. Hall. Computed Tomography — An Increasing Source of Radiation Exposure. *New England Journal of Medicine*, 357(22):2277–2284, November 2007.

[16] Richard Bukata. Are Mobile CT Stroke Units Worth the Price Tag? *Emergency Physicians Monthly*, January 2017.

[17] Cristina Carias, Gabriel Rainisch, Manjunath Shankar, Bishwa B. Adhikari, David L. Swerdlow, William A. Bower, Satish K. Pillai, Martin I. Meltzer, and Lisa M. Koonin. Potential demand for respirators and surgical masks during a hypothetical influenza pandemic in the United States. *Clinical Infectious Diseases: An Official Publication of the Infectious Diseases Society of America*, 60 Suppl 1:S42–51, May 2015.

[18] CDC. Coronavirus Disease 2019 (COVID-19), February 2020.

[19] Stanley H Chan, Ramsin Khoshabeh, Kristofor B Gibson, Philip E Gill, and Truong Q Nguyen. An augmented lagrangian method for total variation video restoration. *IEEE Transactions on Image Processing*, 20(11):3097–3111, 2011.

[20] Subrahmanyan Chandrasekhar. *Radiative transfer*. Courier Corporation, 2013.

[21] Neurologica Corporation. Ceretom portable ct, 2018.

[22] Neurologica Corporation. Ceretom portable ct, 2018.

[23] Avilash Cramer, Jaime Caines, Tim Moulton, Kai Yang, Wolfgang Krull, and Rajiv Gupta. A Compact High Voltage System for Experimental X-Ray Sources. Wiley, July 2019.

[24] Avilash Cramer, Jake Hecla, Dufan Wu, Xiaochun Lai, Tim Boers, Kai Yang, Tim Moulton, Steven Kenyon, Zaven Arzoumanian, Wolfgang Krull, Keith Gendreau, and Rajiv Gupta. Stationary Computed Tomography for Space and other Resource-constrained Environments. *Scientific Reports*, 8(1):1–10, September 2018.

[25] Avilash Cramer, Jake Hecla, Dufan Wu, Xiaochun Lai, Tim Boers, Kai Yang, Tim Moulton, Steven Kenyon, Zaven Arzoumanian, Wolfgang Krull, Keith Gendreau, and Rajiv Gupta. Stationary computed tomography for space and other resource-constrained environments. *Scientific Reports*, 8(1):14195, 2018.

[26] Avilash Cramer, Enze Tian, Sherryl H. Yu, Mitchell Galanek, Edward Lamere, Ju Li, Rajiv Gupta, and Michael P. Short. Disposable N95 Masks Pass Qualitative Fit-Test But Have Decreased Filtration Efficiency after Cobalt-60 Gamma Irradiation. *medRxiv*, page 2020.03.28.20043471, March 2020. Publisher: Cold Spring Harbor Laboratory Press.

[27] B. De Man, J. Uribe, J Baek, D. Harrison, Z Yin, R. Longtin, J. Roy, B. Waters, C. Wilson, J. Short, L. Inzinna, J. Reynolds, V.B. Neculaes, K. Frutschy, B. Senzig, and N. Pelc. Multisource inverse-geometry CT. Part I. system concept and development. *Medical Physics*, 43(6):4607–4616, 2016.

[28] Steven Duclos. Scintillator Phosphors for Medical Imaging. *The Electrochemical Society Interface*, 1998.

[29] Martin Ebinger, Benjamin Winter, Matthias Wendt, Joachim E. Weber, Carolin Waldschmidt, Michal Rozanski, Alexander Kunz, Peter Koch, Philipp A. Kellner, Daniel Gierhake, Kersten Villringer, Jochen B. Fiebach, Ulrike Grittner, Andreas Hartmann, Bruno-Marcel Mackert, Matthias Endres, Heinrich J. Audebert, and STEMO Consortium. Effect of the use of ambulance-based thrombolysis on time to thrombolysis in acute ischemic stroke: a randomized clinical trial. *JAMA*, 311(16):1622–1631, April 2014.

[30] Albert Einstein. On a Heuristic Point of View Concerning the Production and Transformation of Light. *Annalen der Physik*, 17:132–148, 1905.

[31] Helen Fan, Heather L Durko, Stephen K Moore, Jared Moore, Brian W Miller, Lars R Furenlid, Sunil Pradhan, and Harrison H Barrett. Dr with a dslr: digital radiography with a digital single-lens reflex camera. In *Proceedings of SPIE–the International Society for Optical Engineering*, volume 7622, page 76225E. NIH Public Access, 2010.

[32] Friederike Feldmann, W. Lesley Shupert, Elaine Haddock, Barri Twardoski, and Heinz Feldmann. Gamma Irradiation as an Effective Method for Inactivation of Emerging Viral Pathogens. *The American Journal of Tropical Medicine and Hygiene*, 100(5):1275–1277, May 2019.

[33] Shuo Feng, Chen Shen, Nan Xia, Wei Song, Mengzhen Fan, and Benjamin J Cowling. Rational use of face masks in the COVID-19 pandemic. *The Lancet Respiratory Medicine*, page S221326002030134X, March 2020.

[34] Robert Fischer, Dylan H. Morris, Neeltje van Doremalen, Shanda Sarchette, Jeremiah Matson, Trenton Bushmaker, Claude Kwe Yinda, Stephanie Seifert, Amandine Gamble, Brandi Williamson, Seth Judson, Emmie de Wit, Jamie Lloyd-Smith, and Vincent Munster. Assessment of N95 respirator decontamination and re-use for SARS-CoV-2. *medRxiv*, page 2020.04.11.20062018, April 2020. Publisher: Cold Spring Harbor Laboratory Press.

[35] C. Michael Foale, Alexander Y. Kaleri, Ashot E. Sargsyan, Douglas R. Hamilton, Shannon Melton, David Martin, and Scott A. Dulchavsky. Diagnostic Instrumentation Aboard ISS: Just-In-Time Training for Non-Physician Crewmembers. *Aviation, Space, and Environmental Medicine*, 76(6):594–598, June 2005.

[36] Les Folio. *Combat Radiology: Diagnostic Imaging of Blast and Ballistic Injuries*. Springer, New York, NY, June 2010.

[37] Sairam Geethanath and John Thomas Vaughan. Accessible magnetic resonance imaging: A review. *Journal of magnetic resonance imaging: JMRI*, 49(7):e65–e77, June 2019.

[38] Keith C. Gendreau, Zaven Aroumanian, Steven J. Kenyon, and Nick Salvatore Spartana. Miniaturized high-speed modulated x-ray source, February 2014. U.S. Classification 378/123, 378/136; International Classification H01J35/06; Cooperative Classification H01J35/06, H05G1/70, H01J35/065.

[39] Adam Geva, Yoav Y. Schechner, Yonatan Chernyak, and Rajiv Gupta. X-ray computed tomography through scatter. In Vittorio Ferrari, Martial Hebert, Cristian Sminchisescu, and Yair Weiss, editors, *Computer Vision – ECCV 2018*, pages 37–54, Cham, 2018. Springer International Publishing.

[40] E L Gingold, X Wu, and G T Barnes. Contrast and dose with Mo-Mo, Mo-Rh, and Rh-Rh target-filter combinations in mammography. *Radiology*, 195(3):639–644, June 1995.

[41] Ioannis Gkioulekas, Anat Levin, and Todd Zickler. An evaluation of computational imaging techniques for heterogeneous inverse scattering. In Bastian Leibe, Jiri Matas, Nicu Sebe, and Max Welling, editors, *Computer Vision – ECCV 2016*, pages 685–701, Cham, 2016. Springer International Publishing.

[42] Tom Goldstein and Stanley Osher. The split bregman method for l1-regularized problems. *SIAM journal on imaging sciences*, 2(2):323–343, 2009.

[43] Ramon Gilberto Gonzalez, William A. Copen, Pamela W. Schaefer, Michael H. Lev, Stuart R. Pomerantz, Otto Rapalino, John W. Chen, George J. Hunter,

Javier M. Romero, Bradley R. Buchbinder, Mykol Larvie, Joshua Adam Hirsch, and Rajiv Gupta. The Massachusetts General Hospital acute stroke imaging algorithm: an experience and evidence based approach. *Journal of NeuroInterventional Surgery*, 5(suppl 1):i7–i12, May 2013.

[44] Robbie Gonzalez. NASA Can Use Pulsars to Navigate Deep Space. Where to Now? *WIRED*, January 2018.

[45] Rajiv Gupta and Richard I Hartley. Linear pushbroom cameras. *IEEE Transactions on pattern analysis and machine intelligence*, 19(9):963–975, 1997.

[46] Rajiv Gupta and Yongjin Sung. System and method for motion-free computed tomography, 2015. US Patent No. 20170196522A1.

[47] Leslie Hall, Jonathan A. Otter, John Chewins, and Nancy L. Wengenack. Use of hydrogen peroxide vapor for deactivation of Mycobacterium tuberculosis in a biological safety cabinet and a room. *Journal of Clinical Microbiology*, 45(3):810–815, March 2007.

[48] C. Randall Harrell, Valentin Djonov, Crissy Fellabaum, and Vladislav Volarevic. Risks of Using Sterilization by Gamma Radiation: The Other Side of the Coin. *International Journal of Medical Sciences*, 15(3):274–279, 2018.

[49] R. Hart and M. R. Campbell. Digital radiography in space. *Aviation, space, and environmental medicine*, 73(6):601–606, June 2002.

[50] Daichi Hayashi, Li Xu, Frank W. Roemer, David J. Hunter, Ling Li, Avinash M. Katur, and Ali Guermazi. Detection of Osteophytes and Subchondral Cysts in the Knee with Use of Tomosynthesis. *Radiology*, 263(1):206–215, April 2012.

[51] Shahram Hejazi and David P Trauernicht. System considerations in ccd-based x-ray imaging for digital chest radiography and digital mammography. *Medical physics*, 24(2):287–297, 1997.

[52] R. Edward Hendrick. *Breast MRI - Fundamentals and Technical Aspects*. Springer, 2 edition, 2008.

[53] J. C. Le Heron. Estimation of effective dose to the patient during medical X-ray examinations from measurements of the dose-area product. *Physics in Medicine & Biology*, 37(11):2117, 1992.

[54] Bingsheng Huang, Martin Wai-Ming Law, and Pek-Lan Khong. Whole-body PET/CT scanning: estimation of radiation dose and cancer risk. *Radiology*, 251(1):166–174, April 2009.

[55] National Cancer Instititue. TMIST (Tomosynthesis Mammographic Imaging Screening Trial). https://www.cancer.gov/about-cancer/treatment/clinical-trials/nci-supported/tmist.

[56] Ako Itoh, Ei Ueno, Eriko Tohno, Hiroshi Kamma, Hideto Takahashi, Tsuyoshi Shiina, Makoto Yamakawa, and Takeshi Matsumura. Breast Disease: Clinical Application of US Elastography for Diagnosis. *Radiology*, 239(2):341–350, May 2006. Publisher: Radiological Society of North America.

[57] Seby John, Sarah Stock, Thomas Masaryk, Andrew Bauer, Russell Cerejo, Ken Uchino, Stacey Winners, Peter Rasmussen, and Muhammad S. Hussain. Performance of CT Angiography on a Mobile Stroke Treatment Unit: Implications for Triage. *Journal of Neuroimaging: Official Journal of the American Society of Neuroimaging*, 26(4):391–394, July 2016.

[58] Thorsten R. C. Johnson. Dual-Energy CT: General Principles. *American Journal of Roentgenology*, 199(5_supplement):S3–S8, November 2012.

[59] Achuta Kadambi and Petros T Boufounos. Coded aperture compressive 3-d lidar. In *Acoustics, Speech and Signal Processing (ICASSP), 2015 IEEE International Conference on*, pages 1166–1170. IEEE, 2015.

[60] Achuta Kadambi, Refael Whyte, Ayush Bhandari, Lee Streeter, Christopher Barsi, Adrian Dorrington, and Ramesh Raskar. Coded time of flight cameras: sparse deconvolution to address multipath interference and recover time profiles. *ACM Transactions on Graphics (ToG)*, 32(6):167, 2013.

[61] A. Kahnert, P. Seiler, M. Stein, B. Aze, G. McDonnell, and S. H. E. Kaufmann. Decontamination with vaporized hydrogen peroxide is effective against Mycobacterium tuberculosis. *Letters in Applied Microbiology*, 40(6):448–452, 2005.

[62] Willi A. Kalender. X-ray computed tomography. *Physics in Medicine & Biology*, 51(13):R29, 2006.

[63] Paul Kennedy, Mathilde Wagner, Laurent Castéra, Cheng William Hong, Curtis L. Johnson, Claude B. Sirlin, and Bachir Taouli. Quantitative Elastography Methods in Liver Disease: Current Evidence and Future Directions. *Radiology*, 286(3):738–763, February 2018. Publisher: Radiological Society of North America.

[64] Patrick Kenney, Benjamin K. Chan, Kaitlyn Kortright, Margaret Cintron, Nancy Havill, Mark Russi, Jaqueline Epright, Lorraine Lee, Thomas Balcezak, and Richard Martinello. Hydrogen Peroxide Vapor sterilization of N95 respirators for reuse. *medRxiv*, page 2020.03.24.20041087, March 2020. Publisher: Cold Spring Harbor Laboratory Press.

[65] Faiz Khan. *The Physics of Radiation Therapy, 3rd Ed.* Lippincott Williams and Wilkins, Philadelphia, 2003.

[66] Jae G. Kim, A. B. M. Aowlad Hossain, Jong H. Shin, and Soo Y. Lee. Calculation of strain images of a breast-mimicking phantom from 3D CT image data. *Medical Physics*, 39(9):5469–5478, September 2012.

[67] Jae G. Kim, So E. Park, and Soo Y. Lee. X-ray strain tensor imaging: FEM simulation and experiments with a micro-CT. *Journal of X-Ray Science and Technology*, 22(1):63–75, 2014.

[68] Ahmed Kirmani, Dheera Venkatraman, Dongeek Shin, Andrea Colaço, Franco N. C. Wong, Jeffrey H. Shapiro, and Vivek K. Goyal. First-Photon Imaging. *Science*, 343(6166):58–61, January 2014.

[69] A. V. Korol, O. I. Obolensky, A. V. Solov'yov, and I. A. Solovjev. The full relativistic description of the bremsstrahlung process in a charged particle-atom collision. *Journal of Physics B: Atomic, Molecular and Optical Physics*, 34(9):1589, 2001.

[70] Mia Kumar, Steven Mazur, Britini L. Ork, Elena Postnikova, Lisa E. Hensley, Peter B. Jahrling, Reed Johnson, and Michael R. Holbrook. Inactivation and safety testing of Middle East Respiratory Syndrome Coronavirus. *Journal of Virological Methods*, 223:13–18, October 2015.

[71] Bruce Lee and Andrew Newberg. Neuroimaging in Traumatic Brain Imaging. *NeuroRx*, 2(2):372–383, April 2005.

[72] Robert M. Lerner, S. R. Huang, and Kevin J. Parker. "Sonoelasticity" images derived from ultrasound signals in mechanically vibrated tissues. *Ultrasound in Medicine & Biology*, 16(3):231–239, January 1990.

[73] Christopher L. Liptak, Deborah Tovey, William P. Segars, Frank D. Dong, and Xiang Li. Anatomy-based transmission factors for technique optimization in portable chest x-ray. volume 9412, pages 941247–941247–9, 2015.

[74] Mark P. Little, Richard Wakeford, and Gerald M. Kendall. Updated estimates of the proportion of childhood leukaemia incidence in Great Britain that may be caused by natural background ionising radiation. *Journal of Radiological Protection: Official Journal of the Society for Radiological Protection*, 29(4):467–482, December 2009.

[75] Mark P. Little, Richard Wakeford, E. Janet Tawn, Simon D. Bouffler, and Amy Berrington de Gonzalez. Risks Associated with Low Doses and Low Dose Rates of Ionizing Radiation: Why Linearity May Be (Almost) the Best We Can Do. *Radiology*, 251(1):6–12, April 2009.

[76] Zejian Liu, Guang Yang, Yueh Z. Lee, David Bordelon, Jianping Lu, and Otto Zhou. Carbon nanotube based microfocus field emission x-ray source for microcomputed tomography. *Applied Physics Letters*, 89(10):103111, September 2006.

[77] R.A Loch. Cesium-Telluride and Magnesium for high quality photocathodes, June 2005. Master's Thesis, University of Twente.

[78] K. O. Lovblad, H. J. Laubach, A. E. Baird, F. Curtin, G. Schlaug, R. R. Edelman, and S. Warach. Clinical experience with diffusion-weighted MR in patients with acute stroke. *American Journal of Neuroradiology*, 19(6):1061–1066, June 1998.

[79] O. J. Ma, J. R. Mateer, M. Ogata, M. P. Kefer, D. Wittmann, and C. Aprahamian. Prospective analysis of a rapid trauma ultrasound examination performed by emergency physicians. *The Journal of trauma*, 38(6):879–885, June 1995.

[80] O. John Ma, Jeffrey G. Norvell, and Srikala Subramanian. Ultrasound applications in mass casualties and extreme environments. *Critical Care Medicine*, 35(5):S275, May 2007.

[81] Alireza Mahdavi, Fariborz Haghighat, Ali Bahloul, Clothilde Brochot, and Claude Ostiguy. Particle loading time and humidity effects on the efficiency of an N95 filtering facepiece respirator model under constant and inhalation cyclic flows. *The Annals of Occupational Hygiene*, 59(5):629–640, June 2015.

[82] A. Manduca, T. E. Oliphant, M. A. Dresner, J. L. Mahowald, S. A. Kruse, E. Amromin, J. P. Felmlee, J. F. Greenleaf, and R. L. Ehman. Magnetic resonance elastography: non-invasive mapping of tissue elasticity. *Medical Image Analysis*, 5(4):237–254, December 2001.

[83] Axel Martinez-Möller, Michael Souvatzoglou, Gaspar Delso, Ralph A. Bundschuh, Christophe Chefd'hotel, Sibylle I. Ziegler, Nassir Navab, Markus Schwaiger, and Stephan G. Nekolla. Tissue Classification as a Potential Approach for Attenuation Correction in Whole-Body PET/MRI: Evaluation with PET/CT Data. *Journal of Nuclear Medicine*, 50(4):520–526, April 2009.

[84] K. Martini, A. S. Becker, R. Guggenberger, G. Andreisek, and T. Frauenfelder. Value of tomosynthesis for lesion evaluation of small joints in osteoarthritic hands using the OARSI score. *Osteoarthritis and Cartilage*, 24(7):1167–1171, July 2016.

[85] P Michelato. Photocathodes for RF photoinjectors. *Nuclear Instruments and Methods in Physics Research Section A: Accelerators, Spectrometers, Detectors and Associated Equipment*, 393(1):455–459, July 1997.

[86] Tarun K. Mittal and Michael B. Rubens. *Computed Tomography Techniques and Principles. Part a. Electron Beam Computed Tomography*, pages 93–98. Springer London, London, 2006.

[87] Arash Mostaghimi, Marc-Joseph Antonini, Deborah Plana, Philip D. Anderson, Brandon Beller, Edward W. Boyer, Amber Fannin, Jacob Freake, Richard Oakley, Michael S. Sinha, Leanne Smith, Christopher Van, Helen Yang, Peter K. Sorger, Nicole R. LeBoeuf, and Sherry H. Yu. Regulatory and Safety Considerations in Deploying a Locally Fabricated, Reusable Face Shield in a Hospital

Responding to the COVID-19 Pandemic. *Med*, 0(0), June 2020. Publisher: Elsevier.

[88] Gerd Muehllehner and Joel S. Karp. Positron emission tomography. *Physics in Medicine & Biology*, 51(13):R117, 2006.

[89] Phillip E Muntz and Wende Westinghouse Logan. Focal Spot Size and Scatter Suppression in Magnification Mammography. *American Journal of Roentgenology*, 133:453–459, September 1979.

[90] R. Muthupillai, D. J. Lomas, P. J. Rossman, J. F. Greenleaf, A. Manduca, and R. L. Ehman. Magnetic resonance elastography by direct visualization of propagating acoustic strain waves. *Science (New York, N.Y.)*, 269(5232):1854–1857, September 1995.

[91] R. Muthupillai, P. J. Rossman, D. J. Lomas, J. F. Greenleaf, S. J. Riederer, and R. L. Ehman. Magnetic resonance imaging of transverse acoustic strain waves. *Magnetic Resonance in Medicine*, 36(2):266–274, August 1996.

[92] H Nie, M Schoenitz, and E. Dreizin. Oxidation of magnesium: Implication for aging and ignition. *The Journal of Physical Chemistry C*, 120:974–983, December 2015.

[93] Schoenitz M Dreizin E. Nie, H. Oxidation of Magnesium: Implication for Aging and Ignition. *The Journal of Physical Chemistry C*, 120:974–983, December 2015.

[94] Takeshi Nishioka, Tohru Shiga, Hiroki Shirato, Eriko Tsukamoto, Kazuhiko Tsuchiya M.d, Takashi Kato, Keiichi Ohmori, Akira Yamazaki, Hidefumi Aoyama, Seiko Hashimoto, Ta-Chen Chang, and Kazuo Miyasaka. Image fusion between 18fdg-PET and MRI/CT for radiotherapy planning of oropharyngeal and nasopharyngeal carcinomas. *International Journal of Radiation Oncology*, 53(4):1051–1057, July 2002.

[95] OECD. Computed Tomography (CT) exams (indicator), 2018. DOI: 10.1787/3c994537-en.

[96] J. M. Ollinger and J. A. Fessler. Positron-emission tomography. *IEEE Signal Processing Magazine*, 14(1):43–55, January 1997.

[97] J. Ophir, I. Cespedes, B. Garra, H. Ponnekanti, Y. Huang, and N. Maklad. Elastography: Ultrasonic imaging of tissue strain and elastic modulus in vivo. *European Journal of Ultrasound*, 3(1):49–70, January 1996.

[98] J. Ophir, I. Céspedes, H. Ponnekanti, Y. Yazdi, and X. Li. Elastography: A quantitative method for imaging the elasticity of biological tissues. *Ultrasonic Imaging*, 13(2):111–134, April 1991.

[99] D Palmer. A Review of Metallic Photocathode Research, 2005. SLAC-TN-05-080.

[100] Hae-Kwan Park, Won-Il Joo, Chung-Kee Chough, Chul-Beom Cho, Kyung-Jin Lee, and Hyoung-Kyun Rha. The clinical efficacy of repeat brain computed tomography in patients with traumatic intracranial haemorrhage within 24 hours after blunt head injury. *British Journal of Neurosurgery*, 23(6):617–621, December 2009.

[101] Richard Parmee, Clare Collins, William Milne, and Matthew Cole. X-ray generation using carbon nanotubes. *Nano Convergence*, 1(34), 2014.

[102] C. R. Peebles. Non-invasive coronary imaging: computed tomography or magnetic resonance imaging? *Heart (British Cardiac Society)*, 89(6):591–594, Jun 2003. 12748207[pmid].

[103] W. G. Penney. The photoelectric effect in thin metallic films. *Proc. R. Soc. Lond. A*, 133(822):407–417, October 1931.

[104] F. Le Pimpec, F. Ardana-Lamas, C. P. Hauri, and C. Milne. Quantum efficiency of technical metal photocathodes under laser irradiation of various wavelength. *Applied Physics A*, 112(3):647–661, September 2013. arXiv: 1202.0152.

[105] Etta D. Pisano, Constantine Gatsonis, Edward Hendrick, Martin Yaffe, Janet K. Baum, Suddhasatta Acharyya, Emily F. Conant, Laurie L. Fajardo, Lawrence Bassett, Carl D'Orsi, Roberta Jong, and Murray Rebner. Diagnostic Performance of Digital versus Film Mammography for Breast-Cancer Screening. *New England Journal of Medicine*, 353(17):1773–1783, October 2005.

[106] G. J. van der Plaats. *Medical X-Ray Techniques in Diagnostic Radiology: A textbook for radiographers and Radiological Technicians*. Springer Science & Business Media, December 2012. Google-Books-ID: dpfqCAAAQBAJ.

[107] Steven P. Poplack, Tor D. Tosteson, Christine A. Kogel, and Helene M. Nagy. Digital Breast Tomosynthesis: Initial Experience in 98 Women with Abnormal Digital Screening Mammography. *American Journal of Roentgenology*, 189(3):616–623, September 2007.

[108] R. A. Powell, W. E. Spicer, G. B. Fisher, and P. Gregory. Photoemission Studies of Cesium Telluride. *Physical Review B*, 8(8):3987–3995, October 1973.

[109] Connor Puett, Christina Inscoe, Allison Hartman, Jabari Calliste, Dora K. Franceschi, Jianping Lu, Otto Zhou, and Yueh Z. Lee. An update on carbon nanotube-enabled X-ray sources for biomedical imaging. *Wiley Interdisciplinary Reviews. Nanomedicine and Nanobiotechnology*, 10(1), January 2018.

[110] Xin Qian, Andrew Tucker, Emily Gidcumb, Jing Shan, Guang Yang, Xiomara Calderon-Colon, Shabana Sultana, Jianping Lu, Otto Zhou, Derrek Spronk,

Frank Sprenger, Yiheng Zhang, Don Kennedy, Tom Farbizio, and Zhenxue Jing. High resolution stationary digital breast tomosynthesis using distributed carbon nanotube x-ray source array. *Medical Physics*, 39(4):2090–2099, April 2012.

[111] Gupta R., Krull W., J. Hecla, Cramer A., Kenyon S., Gendreau K., and Arzoumanian Z. Design of a distributed, modulated x-ray source for use in tomographic imaging. patent application submitted by NASA as Docket No. GSC-18126-1 (4/25/2019).

[112] Lewis J. (Jr) Radonovich, Aliya Baig, Ronald E Shaffer, Raymond Roberge, Andrew Levinson, Donald F Doerr, and Victoria Davey. BETTER RESPIRATORY EQUIPMENT USING ADVANCED TECHNOLOGIES FOR HEALTHCARE EMPLOYEES (PROJECT B.R.E.A.T.H.E.). Technical report, e Office of Public Health and Environmental Hazards in the Veterans Health Administration at the U.S. Department of Veterans Affairs, 2009.

[113] Joshua Rapp and Vivek K Goyal. A few photons among many: Unmixing signal and noise for photon-efficient active imaging. *arXiv preprint arXiv:1609.07407*, 2016.

[114] Amy Ray, Federico Perez, Amanda M. Beltramini, Marta Jakubowycz, Patricia Dimick, Michael R. Jacobs, Kathy Roman, Robert A. Bonomo, and Robert A. Salata. Use of vaporized hydrogen peroxide decontamination during an outbreak of multidrug-resistant Acinetobacter baumannii infection at a long-term acute care hospital. *Infection Control and Hospital Epidemiology*, 31(12):1236–1241, December 2010.

[115] Bryan P. Ribaya, Joseph Leung, Philip Brown, Mahmud Rahman, and Cattien V. Nguyen. A study on the mechanical and electrical reliability of individual carbon nanotube field emission cathodes. *Nanotechnology*, 19(18):185201, May 2008.

[116] W.C. Roentgen. On a new kind of rays. *Radiography*, 36(428):185–8, August 1970. Translated by Arthur Stanton from the Sitzungsberichte der Würzburger Physic-medic. Gesellschaft, 1895. Nature, January 23, 1896.

[117] Leonid I Rudin, Stanley Osher, and Emad Fatemi. Nonlinear total variation based noise removal algorithms. *Physica D: Nonlinear Phenomena*, 60(1-4):259–268, 1992.

[118] Christin Sander. Neurovascular coupling to D2/D3 dopamine receptor occupancy using simultaneous PET/functional MRI | Proceedings of the National Academy of Sciences. *Proceedings of the National Academy of Sciences*, 110(27):11169–11174.

[119] Jeffrey L. Saver. Time Is Brain - Quantified. *Stroke*, 37(1):263–266, January 2006.

[120] Y. Y. Schechner, S. K. Nayar, and P. N. Belhumeur. Multiplexing for optimal lighting. *IEEE Transactions on Pattern Analysis and Machine Intelligence*, 29(8):1339–1354, Aug 2007.

[121] Peter D. Schellinger, Olav Jansen, Jochen B. Fiebach, Werner Hacke, and Klaus Sartor. A Standardized MRI Stroke Protocol: Comparison with CT in Hyperacute Intracerebral Hemorrhage. *Stroke*, 30(4):765–768, April 1999.

[122] Jo Schlemper, Ilkay Oksuz, James R. Clough, Jinming Duan, Andrew P. King, Julia A. Schnabel, Joseph V. Hajnal, and Daniel Rueckert. dAUTOMAP: decomposing AUTOMAP to achieve scalability and enhance performance. *arXiv:1909.10995 [cs, eess, stat]*, September 2019. arXiv: 1909.10995.

[123] Antony Schwartz, Matthew Stiegel, Nicole Greeson, Andrea Vogel, Wayne Thomann, Monte Brown, Gregory D. Sempowski, Thomas Scott Alderman, James Patrick Condreay, James Burch, Cameron Wolfe, Becky Smith, and Sarah Lewis. Decontamination and Reuse of N95 Respirators with Hydrogen Peroxide Vapor to Address Worldwide Personal Protective Equipment Shortages During the SARS-CoV-2 (COVID-19) Pandemic. *Applied Biosafety*, page 1535676020919932, April 2020. Publisher: SAGE Publications Inc.

[124] Jing Shan. *Development of a Stationary Chest Tomosynthesis System Using Carbon Nanotube X-ray Source Array.* PhD thesis, UNC Chapel Hill, 2015.

[125] Jing Shan, Andrew W. Tucker, Yueh Z. Lee, Michael D. Heath, Xiaohui Wang, David H. Foos, Jianping Lu, and Otto Zhou. Stationary chest tomosynthesis using a carbon nanotube x-ray source array: a feasibility study. *Physics in Medicine & Biology*, 60(1):81, 2015.

[126] D. Shin, A. Kirmani, and V. K. Goyal. Low-rate poisson intensity estimation using multiplexed imaging. In *2013 IEEE International Conference on Acoustics, Speech and Signal Processing*, pages 1364–1368, May 2013.

[127] Dongeek Shin, Ahmed Kirmani, Vivek K Goyal, and Jeffrey H Shapiro. Photon-efficient computational 3-d and reflectivity imaging with single-photon detectors. *IEEE Transactions on Computational Imaging*, 1(2):112–125, 2015.

[128] Rosa M. S. Sigrist, Joy Liau, Ahmed El Kaffas, Maria Cristina Chammas, and Juergen K. Willmann. Ultrasound Elastography: Review of Techniques and Clinical Applications. *Theranostics*, 7(5):1303–1329, 2017.

[129] Jason Silverstein. Most of the World Doesn't Have Access to X-Rays. *The Atlantic*, September 2016.

[130] Rebecca Smith-Bindman. Radiation Dose Associated With Common Computed Tomography Examinations and the Associated Lifetime Attributable Risk of Cancer. *Archives of Internal Medicine*, 169(22):2078, December 2009.

[131] Andrew M. Southerland, Karen C. Johnston, Carlos A. Molina, Magdy Selim, Noreen Kamal, and Mayank Goyal. Suspected Large Vessel Occlusion - Should EMS transport to the nearest PSC or bypass to a CSC with Endovascular Capabilities? *Stroke; a journal of cerebral circulation*, 47(7):1965–1967, July 2016.

[132] Perry Sprawls. *The Physical Principles of Medical Imaging, 2nd Ed.* Medical Physics Publishing, Madison, Wisconsin, 1995. Accessed online at http://www.sprawls.org/ppmi2.

[133] T. Srinivasan-Rao, J. Schill, I. Ben Zvi, and M. Woodle. Sputtered magnesium as a photocathode material for rf injectors. *Review of Scientific Instruments*, 69(6):2292–2296, June 1998.

[134] James R. Stevenson and Eugene B. Hensley. Thermionic and Photoelectric Emission from Magnesium Oxide. *Journal of Applied Physics*, 32(2):166–172, February 1961.

[135] L. Streeter, G. R. Burling-Claridge, M. J. Cree, and R. Künnemeyer. Optical full hadamard matrix multiplexing and noise effects. *Appl. Opt.*, 48(11):2078–2085, Apr 2009.

[136] H. Sugie, M. Tanemura, V. Filip, K. Iwata, K. Takahashi, and F. Okuyama. Carbon nanotubes as electron source in an x-ray tube. *Applied Physics Letters*, 78(17):2578–2580, April 2001.

[137] Robert Sullivan, Alexander C. Fassolitis, Edward P. Larkin, Ralston B. Read, and James T. Peeler. Inactivation of Thirty Viruses by Gamma Radiation 1. *Applied Microbiology*, 22(1):61–65, 1971.

[138] Anke Thomas, Sherko Kümmel, Florian Fritzsche, Mathias Warm, Bernd Ebert, Bernd Hamm, and Thomas Fischer. Real-time sonoelastography performed in addition to B-mode ultrasound and mammography: improved differentiation of breast lesions? *Academic Radiology*, 13(12):1496–1504, December 2006.

[139] Elihu Thompson. Roentgen-ray Tube, August 1896. US575772 A. The General Electric Company, Assignee.

[140] Maurice Tubiana. Computed Tomography and Radiation Exposure. *New England Journal of Medicine*, 358(8):850–853, February 2008.

[141] OCSPP US EPA. List N: Disinfectants for Use Against SARS-CoV-2, March 2020. Library Catalog: www.epa.gov.

[142] Sudhakar K. Venkatesh and Richard L. Ehman. Magnetic Resonance Elastography of Abdomen. *Abdominal imaging*, 40(4):745–759, April 2015.

[143] Dennis J Viscusi, Michael S Bergman, Benjamin C Eimer, and Ronald E Shaffer. Evaluation of Five Decontamination Methods for Filtering Facepiece Respirators. *Ann. Occ. Hyg.*, 53(8):815–827, October 2009.

[144] Dennis J Viscusi, William P King, and Ronald E Shaffer. Effect of Decontamination on the Filtration Efficiency of Two Filtering Facepiece Respirator Models. *Journal of the International Society for Respiratory Protection*, 24:93–107, 2007.

[145] David Walter, Uwe Zscherpel, and Uwe Ewert. *Photon Counting and Energy Discriminating X-Ray Detectors-Benefits and Applications*. Bundesanstalt für Materialforschung und-prüfung (BAM), 2016.

[146] Silke Walter, Panagiotis Kostopoulos, Anton Haass, Isabel Keller, Martin Lesmeister, Thomas Schlechtriemen, Christian Roth, Panagiotis Papanagiotou, Iris Grunwald, Helmut Schumacher, Stephan Helwig, Julio Viera, Heiko Körner, Maria Alexandrou, Umut Yilmaz, Karin Ziegler, Kathrin Schmidt, Rainer Dabew, Darius Kubulus, Yang Liu, Thomas Volk, Kai Kronfeld, Christian Ruckes, Thomas Bertsch, Wolfgang Reith, and Klaus Fassbender. Diagnosis and treatment of patients with stroke in a mobile stroke unit versus in hospital: a randomised controlled trial. *The Lancet. Neurology*, 11(5):397–404, May 2012.

[147] David R. Williams and Matthew Turnock. Human Space Exploration The Next Fifty Years. *McGill Journal of Medicine : MJM*, 13(2), June 2011.

[148] L. T. Williams, V. S. Kumsomboone, W. J. Ready, and M. L. R. Walker. Lifetime and Failure Mechanisms of an Arrayed Carbon Nanotube Field Emission Cathode. *IEEE Transactions on Electron Devices*, 57(11):3163–3168, November 2010.

[149] Y. Yamakoshi, J. Sato, and T. Sato. Ultrasonic imaging of internal vibration of soft tissue under forced vibration. *IEEE transactions on ultrasonics, ferroelectrics, and frequency control*, 37(2):45–53, 1990.

[150] Ming Yan. Restoration of images corrupted by impulse noise and mixed gaussian impulse noise using blind inpainting. *SIAM Journal on Imaging Sciences*, 6(3):1227–1245, 2013.

[151] G. Yang. *Carbon nanotube based stationary x-ray tomosynthesis scanner for detection of breast cancer*. PhD thesis, The University of North Carolina at Chapel Hill, 2008.

[152] D. M. Yealy and D. E. Hogan. Imaging after head trauma. Who needs what? *Emergency Medicine Clinics of North America*, 9(4):707–717, November 1991.

[153] Quan Yuan, Aaron W. Baum, R. Fabian W. Pease, and Piero Pianetta. Effect of oxygen adsorption on the efficiency of magnesium photocathodes. *Journal of Vacuum Science & Technology B: Microelectronics and Nanometer Structures Processing, Measurement, and Phenomena*, 21(6):2830–2833, November 2003.

[154] Hongyan Zhang, Wei He, Liangpei Zhang, Huanfeng Shen, and Qiangqiang Yuan. Hyperspectral image restoration using low-rank matrix recovery. *IEEE Transactions on Geoscience and Remote Sensing*, 52(8):4729–4743, 2014.

[155] Bo Zhu, Jeremiah Z. Liu, Stephen F. Cauley, Bruce R. Rosen, and Matthew S. Rosen. Image reconstruction by domain-transform manifold learning. *Nature*, 555(7697):487–492, 2018.